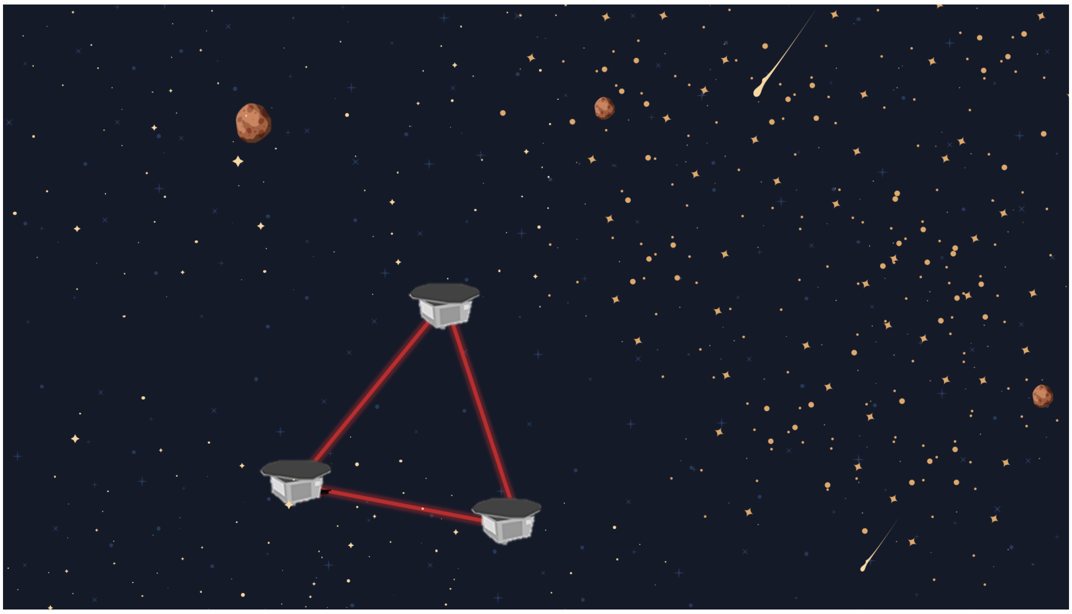

Assessing the Detection of Near Earth Asteroids with the Space-borne Gravitational Waves Detector LISA

Sara Carvalho Marques

Thesis to obtain the Master of Science Degree in

Aerospace Engineering

Supervisors: Dr. Oliver Jennrich
Prof. Paulo Jorge Soares Gil

Examination Committee

Chairperson: Prof. João Manuel Melo de Sousa
Supervisor: Dr. Oliver Jennrich
Member of the Committee: Prof. Patrícia Carla Serrano Gonçalves

July 2024

For my parents, Vitor and Sofia, and sister,
Raquel, who have always motivated me to follow
my dreams.
As Carl Sagan said: “Somewhere, something
incredible is waiting to be known.” and because of
all your support, someday I may discover it.

Declaração

Declaro que o presente documento é um trabalho original da minha autoria e que cumpre todos os requisitos do Código de Conduta e Boas Práticas da Universidade de Lisboa.

Declaration

I declare that this document is an original work of my own authorship and that it fulfills all the requirements of the Code of Conduct and Good Practices of the Universidade de Lisboa.

Acknowledgments

I would like to express my deepest gratitude to Dr. Oliver Jennrich to allow this research work to be possible. Your help, advices and guidance has been invaluable to me and to my future career as a scientist.

Additionally, I would like to thank Professor Paulo Gil for the hints and advices provided in the redaction of this work. Thanks to you, this work is proper and clear to a reader which wants to know how to detect asteroids with LISA.

Resumo

O estudo de ondas gravitacionais apresenta uma oportunidade sem precedentes para a exploração cósmica, com o lançamento futuro da missão Laser Interferometer Space Antenna (LISA) prestes a revolucionar a nossa compreensão do universo. A investigação realizada nesta dissertação examina o uso de um detector de ondas gravitacionais no contexto da ciência planetária, focando particularmente na utilização dos dados recolhidos pela missão LISA para a deteção de asteroídes nas proximidades da Terra (NEAs). Pretende-se compreender quais as variáveis que podem influenciar a deteção de um asteróide, qual a probabilidade de deteção dos mesmos e com que precisão podem-se extrair os seus elementos orbitais e propriedades físicas, como a massa. Utilizando metodologias como modelos teóricos, simulações numéricas e análises estatísticas, bem como técnicas suportadas pela Informação de Fisher, o trabalho revela resultados intrigantes. Obtém-se uma probabilidade não infinitesimal de deteção de NEAs pela missão LISA, particularmente para objetos maiores e aqueles em proximidade orbital mais próxima. A técnica da Informação de Fisher fornece estimativas robustas da incerteza nas propriedades dos NEAs derivadas de observações do LISA, sublinhando o potencial da astronomia de ondas gravitacionais na defesa planetária e na exploração. Os resultados obtidos abrem caminho para futuras investigações destinadas a refinar as probabilidades de deteção, eliminar algumas das hipóteses feitas e metodologias de extração de parâmetros.

Palavras-chave: LISA, NEAs, detecção, probabilidade, massa

Abstract

Gravitational wave astronomy presents an unparalleled opportunity for cosmic exploration, with the imminent launch of the Laser Interferometer Space Antenna (LISA) poised to revolutionize our understanding of the universe.

This work examines the use of gravitational wave astronomy in the planetary science context, particularly focusing on leveraging LISA data for the detection of Near-Earth Asteroids (NEAs). It addresses key questions such as which variables can influence the detection, what is the detection probability for a certain asteroid and which what precision can we be able to extract its orbital elements and physical properties such as the mass.

Employing a comprehensive methodology encompassing theoretical modeling, numerical simulations, and statistical analyses and Fisher Information techniques, the study uncovers significant insights. By examining factors influencing NEA detectability and employing statistical approaches to estimate detection probabilities under different scenarios, the research unveils insightful trends, indicating a likelihood of NEA detection by LISA, particularly for larger objects and those in closer orbital proximity. However, precise models of asteroid mass probability distributions are deemed necessary for more accurate predictions. Fisher Information techniques provide robust estimates of uncertainty in NEA properties derived from LISA observations, underscoring the potential of gravitational wave astronomy in planetary defense and exploration. The obtained insights provide the way for future research aimed at refining detection probabilities, eliminating some of the hypotheses made and parameter extraction methodologies.

Keywords: LISA, NEAs, detection, probability, mass

Contents

List of Tables

List of Figures

Nomenclature

Greek Letters

$\boldsymbol{\theta}_{\text{min}}$	Vector of parameters minimizing least squares problem
$\boldsymbol{\theta}$	Vector of parameters in study
ℓ	Log-likelihood
γ	Rotation angle around rotation axis defined by MOID
$\mathcal{L}$	Likelihood
$\mathcal{N}$	Normal distribution
μ	Mean
Ω	Longitude ascending node
ω	Argument of perihelion
ρ	Density
σ	Standard deviation
σ_Ω	Standard deviation of longitude of ascending node
σ_ω	Standard deviation of argument of perihelion
σ_a	Standard deviation of semi-major axis
σ_e	Standard deviation of eccentricity
σ_i	Standard deviation of inclination
σ_m	Standard deviation of mass
σ_m^*	Normalized standard deviation of mass
τ_{ij}	Arm link direction from S/C i to S/C j
θ	True anomaly

Roman Letters

$\boldsymbol{b}$	Vector for Sherman-Morrison-Woodbury formula
$\boldsymbol{C}$	Covariance matrix
$\boldsymbol{c}$	Vector for Sherman-Morrison-Woodbury formula
$\boldsymbol{D}$	Diagonal matrix of standard deviations
$\boldsymbol{F^d}$	Diagonalized Fisher matrix
$\boldsymbol{F}$	Fisher matrix
$\boldsymbol{M}$	Squared matrix for Sherman-Morrison-Woodbury formula
$\boldsymbol{R}$	Rotation matrix for diagonalization
$\boldsymbol{u}$	Rotated normalized column vectors of diagonalized Fisher Matrix
$\boldsymbol{v}$	Normalized column vectors of diagonalized Fisher Matrix
$\boldsymbol{X}$	Correlation matrix
Δv_{ij}	Change in velocity of test mass in S/C i along the direction $\vec{n}_j$
$\tilde{m}$	Fourier transform of model of signal
$\tilde{X}$	Fourier transform of time-series signal
$\vec{e_p}$	Unit vector from the focal point towards the perihelion
$\vec{e_q}$	Unit vector points from the focal point in the direction of the semi-latus rectum
$\vec{n}_i$	LISA's reference frame direction i
A	Quasi-orthogonal TDI variable
a	Semi-major axis
A_{det}	Area of detectability
C_N	Normalization Constant
d	Diameter
E	Eccentric anomaly
E	Quasi-orthogonal TDI variable
e	Eccentricity
F	Gravitational force
f	Frequency

f_{max}	Maximum frequency for integration
G	Gravitational constant
g	Time-series datastream
H	Absolute magnitude
i	Inclination
k	Constant of integration
L	Armlength
M	Mean anomaly
m	Mass
m	Time-series model of signal
m_0	Initial mass of asteroid
m_{tm}	Mass of test mass
N	Number of pairs (Ω, ω) in grid for Local Search Algorithm
n	Mean motion
n	Time-series noise
$P(\boldsymbol{\theta} \,\vert\, \boldsymbol{F_1},\, \boldsymbol{F_2})$	Probability of parameters given two Fisher matrix measurements
$P(g)$	Evidence probability of observing the datastream
$P(g \,\vert\, x)$	Likelihood probability of observing the signal given a datastream
$P(x)$	Prior probability of observing a signal
$P(x \,\vert\, g)$	Posterior probability of observing the datastream given a signal is present
P_{det}	Probability of detection for LISA's lifetime of 10 years
p_{det}	Probability of detection dependent on mass
$P_{\text{det}}^{\text{syn}}$	Probability of detection for the synodic period
p_{υ}	Geometric albedo
p_{ρ}	Probability density function for density
P_{Ci}	Probability Density Function in Category i
p_{Ci}	Probability Constant for Category i
p_H	Probability density function for absolute magnitude

p_m	Probability density function for mass
p_{p_v}	Probability density function for albedo
Q	Aphelion distance
q	Constant of normalization product of log-likelihood
q	Perihelion distance
r	Orbital radius
r	Radius
r_{SoI}	Radius of sphere of influence
S_{acc}	Noise due to external and residual accelerations
S_{IMS}	Noise due to laser interferometry measurement system
S_c	Noise due to galactic background
S_n	Total noise on simulations
T	Orbital period
T	Quasi-orthogonal TDI variable
T	Time interval for limit
t	Time
T_0	Time of passage at periapsis
T_{syn}	Synodic period between asteroid and LISA's spacecraft
V	Volume
v	Orbital velocity
v	Velocity due to gravitational acceleration
X	Michelson TDI variable
x	Time-series signal
Y	Michelson TDI variable
Z	Michelson TDI variable

List of Acronyms

2D Two-dimensions.

3D Three-dimensions.

BHBs Blackhole Binaries.

DRS Disturbance Reduction System.

EMRI Extreme Mass Ration Inspiral.

ESA European Space Agency.

FT Fourier Transform.

GW Gravitational Waves.

IMS Laser Interferometry Measurement System.

LCGT Large-scale Cryogenic Gravitational wave Telescope.

LIGO National Science Foundation's Laser Interferometer Gravitational-Wave Observatory.

LISA Laser Interferometer Space Antenna.

LSA Local Search Algorithm.

MBHBs Massive Blackhole Binaries.

MOID Minimum Orbital Intersection Distance.

NASA National Aeronautics and Space Administration.

NEAs Near Earth Asteroids.

NEOCC Near-Earth Object Coordination Centre.

OBs Optical Benches.

PDF Probability Density Function.

PHA Potentially Hazardous Asteroid.

PSD Power Spectral Density.

S/C Spacecraft.

SNR Signal to Noise Ratio.

SSA Space-Situational Awareness.

SoI Sphere of Influence.

TDI Time Delay Interferometry.

TNO Transneptunion Object.

Chapter 1

Introduction

1.1 Objectives

The objective of this work is to assess new techniques to measure the physical properties of Near Earth Asteroids and to support current methods used in their orbit determination. The assessment is focused on the feasibility to use the Laser Interferometer Space Antenna constellation for the detection of gravitational waves produced by Near Earth Asteroids when approaching the spacecraft, using the measured signal to extract some of the features of the asteroids, in particular its mass.

Near-Earth Asteroids are of scientific importance due to their participation in the solar system formation process. All the information that can be captured from them helps to be a step closer to understand the formation of the Solar System and answer fundamental questions.

1.2 Context

1.2.1 Gravitational Waves

In 1915, Albert Einstein published his theory of General Relativity [1] determining that massive objects are capable of warping the fabric of space-time, a distortion that manifests itself as gravity. He showed that if these massive objects are moving and accelerating, they are able to create ripples in the space time that would propagate in all directions away from the sources. [2, 3] These ripples are called Gravitational Waves (GW).

It was only in 2015 that the existence of GWs was confirmed by the National Science Foundation's Laser Interferometer Gravitational-Wave Observatory (LIGO). The observatory was able to sense the disruptions of the space-time caused by two merging black holes nearly 1.3 billion light years away. This event was very important in the scientific community as it opened the door to study a new world. Historically speaking, the way to study the universe always relied on electromagnetic radiation in its all kind of forms. Nevertheless, gravitational waves provide an independent and distinct way to get answers for the fundamental questions. They allow us to detect vibrations coming from the farthest reaches of the cosmos from sources like supernova, pulsars, merging black holes, binary systems and so on. Besides, opposite to electromagnetic radiation, gravitational waves interact very little with matter, meaning they will travel unimpeded throughout the Universe, carrying undisturbed information about their sources. [4]

1.2.2 LISA Mission

The Laser Interferometer Space Antenna (LISA) is a future constellation composed by three satellites and will be the first dedicated space-based gravitational wave observatory, a mission led by the European Space Agency (ESA) with contributions from the National Aeronautics and Space Administration (NASA). The launch date is expected to be in 2035 with a lifetime of four years and a possible six years extension. [5]

LISA will be the first space-borne mission probing the entire history of the Universe using gravitational waves. The LISA constellation will fly in a triangular formation in an heliocentric orbit similar to the Earth orbit and will perform precise laser interferometry over an armlength of 2.5 million km. Gravitational waves modulate the frequency of the light used to measure the distance. These variations can be measured and used to detect them. For such, the constellation will lie on a plane in a triangular formation, inclined $60°$ to the ecliptic and with the center of the triangle lying in an Earth similar orbit, forming an heliocentric angle of $19° - 23°$ with the Earth. The triangle rotates around its center and, each $120°$, the spacecrafts return to their initial configuration in the triangle [6]. An illustration of the LISA constellation orbit and respective motion can be seen in Figure 1.1.

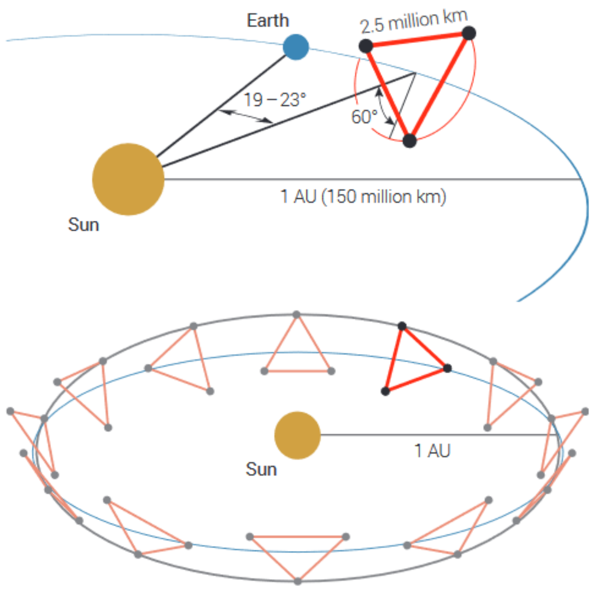

Figure 1.1: Illustration of geometry for LISA orbit [6]. The LISA constellation is composed by three spacecrafts (dark dots) performing precise laser interferometer with a armlength of 2.5 million km (red lines). It is located at $19° - 23°$ behind the Earth orbit around the Sun. The constellation's plane is inclined at $60°$ compared to the Earth's orbit plane.

Some of the Scientific Objectives of the mission include [5]:

- Study the formation and evolution of Compact Binary Stars in the Milky Way galaxy.
- Trace the history of Massive Black Holes throughout the Cosmic Ages.
- Explore the fundamental Nature of Gravity and Black Holes.
- Probe the Expansion Rate of the Universe.
- Search for gravitational wave bursts and unforeseen sources.

As gravitational waves cause ripples in the space-time, measuring the change in the distance of spatially separated objects is a common concept for measuring the effect of gravitational waves. Thus, in order to perform such measurements, each spacecraft is equipped with two test masses kept in free fall acting as reference points for interferometric measurements of the inter-spacecraft distance. This drag-free principle allows to get rid of external noise on the measurements such as perturbations generated from radiation pressure from the Sun. The test masses are put inside cavities in vacuum on each spacecraft, so that they are only subjected to gravity. [6]

The sensitivity of those interferometric measurements is measured through the Characteristic Strain: an average of a frequency dependent power produced by the signal of the gravitational waves. It is a quantity designed to allow to compare the signal of the GW sources described in the frequency domain to the sensitivity of the instruments i.e, their internal noises which can be seen as waves of a certain amplitude in the frequency domain too. By using the characteristic strain, this direct comparison between sources and noise used to assess the possibility of detection can be directly visualized in graphs such the one presented in Figure 1.2. Here, the characteristic strains for the expected noise and some of the supposedly detectable sources are shown. The sensitivity curve, meaning a minimum threshold for detection for the LISA constellation is displayed with and without galactic background noise in green and dotted black, respectively. Everything above these lines is detectable. Several sources, part of LISA detection objectives, are displayed. [7]

The LISA Mission was created to probe gravitational waves from massive black hole coalescence within a vast cosmic volume encompassing all ages, from cosmic dawn to the present, across the epochs of the earliest quasars and of the rise of galaxy structure. The events probed need to be massive since the gravitational force is a very weak force compared to others. Nevertheless, it allows to detect far away sources compared to the other forces since the amplitude decay of the waves is proportional to the inverse of distance and not square of distance. Yet, nothing is said about detecting sources such as near passing by asteroids. If asteroids pass close enough, they may be able to attract the test masses producing a gravitational effect, thus creating noise in the datastream of the interferometers of LISA. This effect is not like the gravitational waves coming from the massive sources, as it doesn't contain as nearly the same intensity nor the same profile. Signals of black holes merging, for instance, are usually chirps [8]. Asteroids generate a profile compared to a lump as we will see later on. Notwithstanding, this gravitational effect can be seen as a signal in the perspective of the detection of asteroids.

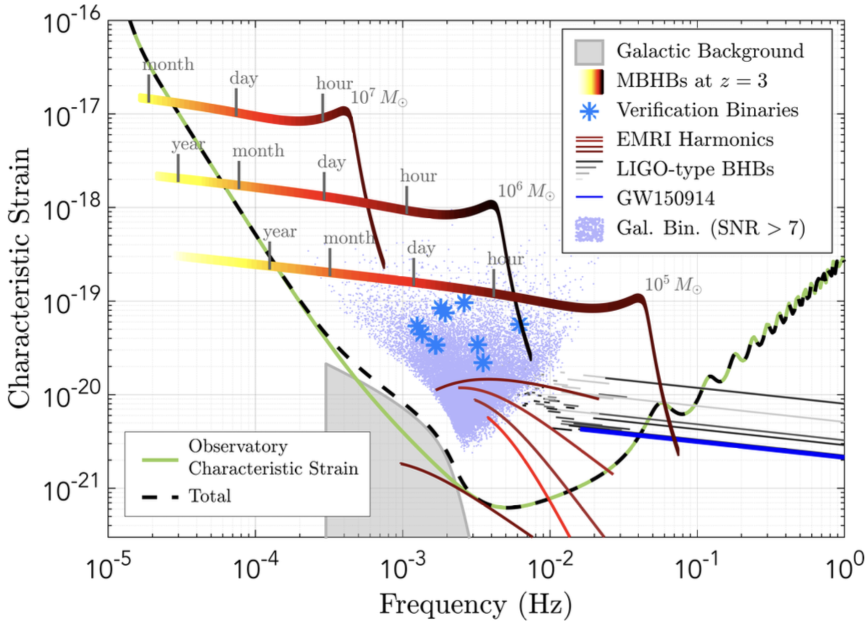

Figure 1.2: LISA sensitivity and some example of GW sources in its frequency range [6]. The green line represents the sensitivity of the LISA constellation due to internal noises while the dotted black line adds up the contribution of the galactic background or foreground which acts as external noise to the measurements done to the spacecraft. In this graph, everything above the black sensitivity line is detectable. Several sources are displayed such as Massive Blackholes Binaries (MBHBs), Blackhole Binaries (BHBs), Verification Binaries, Extreme Mass Ratio Inspiral (EMRI) Harmonics, Galactic Binaries and so on.

1.2.3 Near-Earth Asteroids

Near-Earth Asteroids (NEAs) are asteroids situated close to Earth due to the gravitational attraction of nearby planets that put them into their current orbits. They are seen as remnant debris from the Solar System's formation process, 4.6 billion[1] years ago. NEAs are divided into different groups (Atira, Aten, Apollo and Amor) according to their perihelion distance, q, aphelion distance, Q, and semi-major axes, a as shown in Figure 1.3.

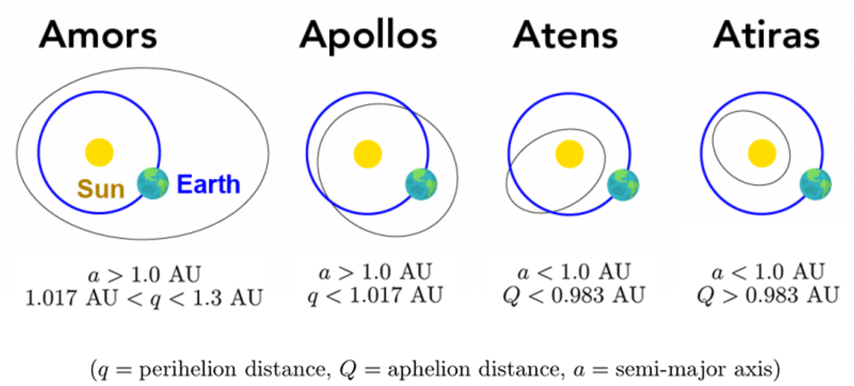

Figure 1.3: Types of near-Earth asteroids. Adapted from [9]

[1] It corresponds to 10^9 years.

The scientific interest on these objects is largely due to the fact that they remain nearly unchanged throughout the years. So, they can be seen as the leftovers of the initial birth of the solar system and be studied to understand more about our primordial universe. Moreover, NEAs can be dangerous if not detected. Due to their proximity to the Earth, they can endanger the humanity if they fall into our planet, so their detection and surveillance is crucial. The asteroids posing a major risk for close encounters with the Earth are called Potentially Hazardous Asteroids (PHA). Until now, more than 32000 NEAs have been found as displayed in Figure 1.4, from which 1596 are considered PHA. [10]

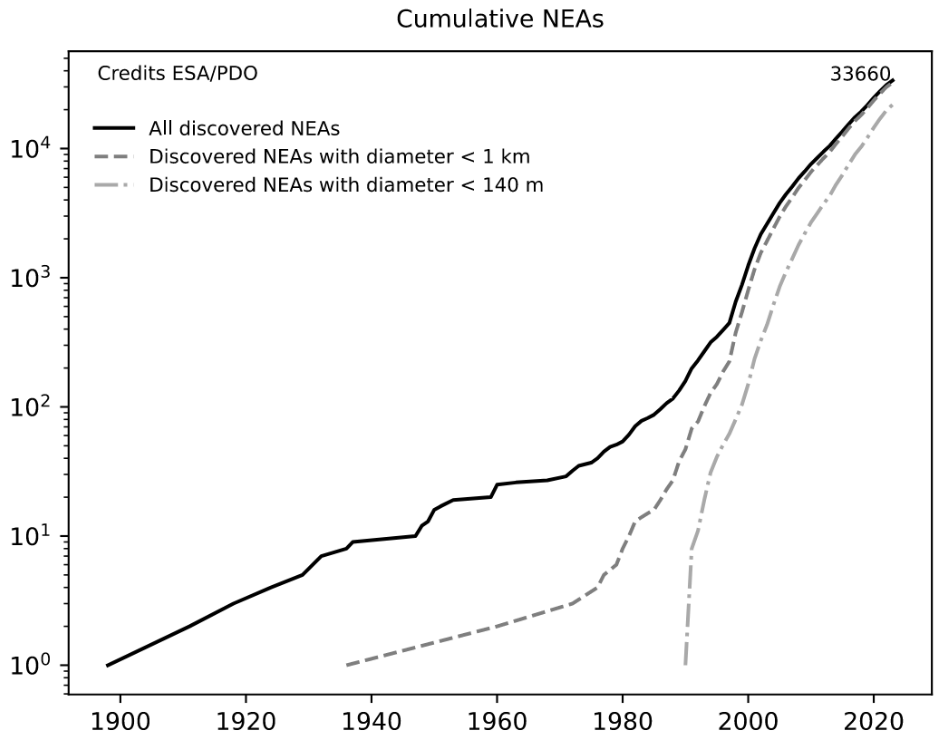

Figure 1.4: NEAs discoveries throughout the years [10]. This graph displays the total cumulative number of discovered NEAs starting on 1900 until today, with cumulative curves for different diameters ranges.

The early efforts to discover NEAs relied upon the comparison of observations of the same region of the sky taken several minutes apart. Stars and galaxies were used as fixed elements to calibrate the observations. Although the technology used evolved throughout the years, currently the same detection techniques depend on the same principle and can be quite inaccurate still. [9]

The discovery of all NEAs and improvement in the technologies of detection becomes, then, very important because if such an object collides with Earth the consequences will be catastrophic. Therefore, if it is possible to predict that there will be a collision, it may be possible to divert the asteroid so that it misses Earth. The earlier the prediction, the more likely that a diversion is possible and successful. As a consequence, with this work we intend to contribute to such methods of detection.

1.3 State of the Art

1.3.1 NEAs Detection

Traditionally, asteroids are detected with the help of observations done by ground-based telescopes or space-born observatories. The problem of determination of orbital elements from observations was firstly tackled by Carl Friedrich Gauss in 1809 [11] using a method with two steps: determination of a preliminary orbit and using the least squares method for its correction. The heliocentric motion of the asteroids is inverted from observations. These observations usually comprise a set of right ascensions and declinations but also sometimes other types of data, such as radar time delay and Doppler astrometry. Since then, the methods for orbit determination evolved including new statistical approaches to deal with the uncertainty and observation errors which impact the prediction of their motion. Even space-borne missions like Gaia from ESA were able to perform observations of small bodies in the Solar System, collecting more than a million of measurements of thousands of transiting bodies [12]. Computer-based iterative orbit-estimation methods also have made it possible to accelerate the exploration of the potential solution space for the inversion problem [13].

Nowadays, using observational data for orbit determination is extended to orbital propagation via the computation of ephemerides, i.e., positions and motion of celestial bodies at certain times. By calculating an asteroid ephemeris, we can prepare observation programs, cross-match or identify a known asteroid, predict stellar occulations and even try to perform rendez-vous with the asteroid. Current methods have evolved to have an accuracy up to a few tenths of arcseconds. [14]

Although the asteroid ephemerides are quite precise for the vast majority of asteroids due to large amount of observations collected, the same cannot be said for their physical properties. Physical properties are not measured easily. The mass of an asteroid is determined using typically four methods. These methods include orbit deflection during close encounters which results on a gravitational pull from which the mass can be deduced [15, 16]. There is also planetary ephemerides which takes into account several asteroids to describe and predict the position of planets [17, 18]. Spacecraft tracking uses the Doppler shifts of the deflected radio signals sent by the spacecraft when passing by an asteroid to be able to determine its properties [19, 20]. Finally, orbital imaging can allow to derive the mass using Kepler's third law [21, 22]. From these methods, we can have an accuracy ranging of a couple percent for the most precise technique (only applicable to a couple of asteroids) to up to values exceeding the 100% for the most inaccurate (applicable to the vast majority) [23]. Diameter measurements are assessed from also four techniques: estimation from the absolute magnitude [24], thermal modeling using mid-infrared radiometry [25, 26], direct observation from stellar occultation [27, 28] and using synthetic models [29]. As the mass measurements, these methods can have an accuracy ranging from a few percent up to uncertainties in the order of 50%. Finally, measurements on the composition are also not very accurate either, relying on models or direct measurements on the previous physical properties. In fact, the uncertainty on the composition can be far greater than 200%. [30]

1.3.2 Gravitational Waves Detection

Interferometry is the common approach chosen to detect gravitational waves. The technique is used in several observatories around the world including the Advanced Virgo in Italy, GEO600 in Germany, LIGO in the United States of America and Large-scale Cryogenic Gravitational wave Telescope (LCGT) in Japan [31]. The limits to the sensitivity of this technique depend on two factors: the ability to measure the phase difference of the returning light in a precise way and the dampening on the noise caused by external forces acting on the mirrors/test masses. The detection itself is bounded by the Poisson statistics of the laser light, which leads to uncertainty on the measurements. On the other hand, the external noises include the seismic noise produced by Earth's seismic activity, wind-induced ground motion and disturbances in the infrastructure, thermal noise from the components closer to the detector and newtonian background due to the gravitational pulls of the sources around the detector. [32]

In contrast to ground-based gravitational wave detectors that have a typical sensitivity in the range from $1\,\mathrm{Hz}$ to $1\,\mathrm{kHz}$ [33], the sensitivity for LISA stretches between 0.1 mHz and 0.1 Hz [6], accessing a frequency window that is inaccessible to ground-based detectors due to the external noises (present on the ground but non-existent in space). The LISA technology has been demonstrated by the LISA Pathfinder mission launched in 2015. Its performance goals included the pure gravitational free fall of the test masses to one order of magnitude of the LISA mission requirements, the demonstration of the laser interferometry with free-falling mirrors and assess the lifetime and reliability of the different apparatus in space [34]. The results obtained indicated that the performance of the interferometer of the LISA Pathfinder mission was better than intended and, when corrected for expected noises due to the sensing equipment and motion of the spacecraft, the performances would be better than the ones required by the LISA mission itself. [35]

While the LISA mission is designed to detect Gravitational Waves from massive sources, there is a first preliminary study to use interferometry to detect asteroids. The perturbation caused on the spacecrafts due to a close approach is assessed making some hypothesis: the asteroids are not massive enough to disturb the full constellation at the same time and the close encounters do not affect the geometry of the constellation. Additionally, it is assumed that the trajectory of the asteroid can be seen as a straight line in a reference frame where the spacecraft is at rest. The results obtained link some physical properties and characteristic motions to a potential detection. [36]

1.4 Thesis Overview

Gravitational waves have opened up unprecedented opportunities for exploring the cosmos. LISA poised to launch in the near future, promises to revolutionize our understanding of the universe. This research investigates the intersection of gravitational wave astronomy and planetary science, particularly focusing on the detection of NEAs using the LISA mission. We address several research questions:

- Can gravitational waves detected by LISA be utilized to identify and track NEAs passing through the inner solar system?
- What is the probability of detecting NEAs using gravitational wave signatures, considering various factors such as their size, distance, and orbital parameters?
- How can uncertainties in the orbital elements and mass of detected NEAs be quantified, given the inherent limitations of gravitational wave measurements?

To answer these questions, this work employs a combination of theoretical modeling for the motion of the LISA constellation and asteroids themselves, numerical simulations for the close approaches, signals and noises making them as realistic as possible, and statistical analyses to investigate the detectability and characterization of the uncertainties of the measurements of NEAs through gravitational wave observations. A fictitious population was used to eliminate the observation bias of the current observed NEA population.

We start by initially examine the factors influencing the detectability of the NEA. Then, statistical approaches are utilized to estimate the probability of NEA detection by LISA assuming any launch date in two scenarios: for any asteroid having a fixed shape and size, the minimum close approach possible, but freedom on the spatial orbital orientation; and for any asteroid having a completely fixed orbit but more freedom in the close approach. Additionally, Fisher information techniques are applied to assess uncertainties in the orbital elements and mass of detected NEAs. Finally, the obtained results emphasize the potential of gravitational wave astronomy, particularly through LISA, in augmenting traditional methods for NEA detection and characterization.

Chapter 2

Scientific Background

In this Chapter, the necessary knowledge to be able to construct a simulation is provided to the reader. The relevant orbital mechanics notions, physical properties of asteroids and the concepts of signal processing and analysis are presented. Lastly, everything is put together and an example is provided.

2.1 Orbital Mechanics

2.1.1 Coordinate System

In order to study the the motion of asteroids and the LISA spacecraft, a coordinate system is needed. The Heliocentric Ecliptic coordinate system is a celestial coordinate system commonly used for representing the apparent positions, orbits, and pole orientations of the Solar System objects. This reference frame is quite useful as it is an inertial reference frame, meaning, there is no rotation with respect to the stars or no accelerating origin [37] . Due to this, we select it as the coordinate system to be used for the simulations.

2.1.2 Classical Orbital Elements

In this work, the trajectories of the asteroids and LISA spacecraft are defined as Keplerian orbits. As such, we use the orbital elements $(a,\, e,\, i,\, \Omega,\, \omega,\, M)$ to define their geometry as well as movement of the bodies [38]. The classical orbital elements traditionally use the true anomaly θ, corresponding to the angular position compared to the perihelion. In this work, the mean anomaly, M, was chosen. The mean anomaly M is defined using the Kepler equation:

$$M = E - e \sin E \tag{2.1}$$

where E is the eccentric anomaly. The eccentric anomaly can be calculated from the true anomaly:

$$\tan\left(\frac{\theta}{2}\right) = \sqrt{\frac{1+e}{1-e}}\tan\left(\frac{E}{2}\right). \tag{2.2}$$

The mean anomaly M was chosen instead of the true anomaly θ because it varies uniformly with time which is more convenient for the orbital calculations performed in this work.

2.1.3 Motion in Orbit

As we will study the motion of the bodies, we calculate the position from the orbit equation

$$r = \frac{a(1-e^2)}{1+e\cos\theta}. \tag{2.3}$$

From this, the position $\vec{r}$ vector is given by

$$\vec{r} = r\cos\theta\,\vec{e}_p + r\sin\theta\,\vec{e}_q. \tag{2.4}$$

where $\vec{e}_p$ is the unit vector that points from the focal point towards the perihelion, and $\vec{e}_q$ the unit vector that points from the focal point in the direction of the semi-latus rectum. Then, with the appropriate rotation matrix, we just insert the orbital plane in space according to the heliocentric ecliptic coordinate system [37]. In Figure 2.1, an orbit defined in the heliocentric ecliptic coordinate system is presented. It includes the motion vectors $\vec{r}$ and velocity $\vec{v}$ as well as some of the orbital elements.

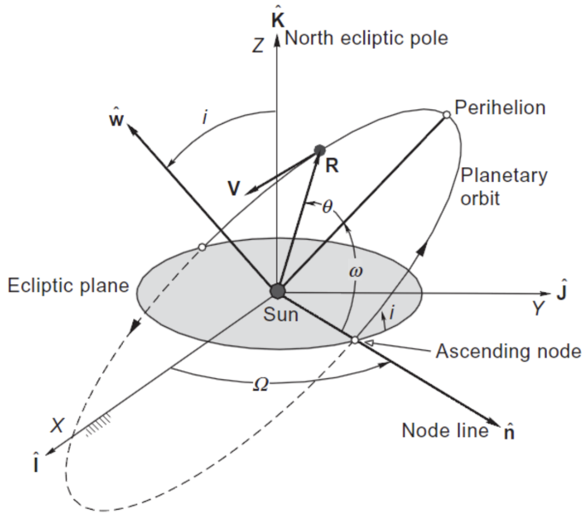

Figure 2.1: Orbit defined in heliocentric ecliptic coordinate system. Adapted from [37]. The orbit of the planet is represented using a dash line for the part below the ecliptic plane followed by a filled line above the ecliptic plane. The ecliptic plane is represented in grey. The inclination of the orbit is the angle between the normal of the orbital plane $\hat{w}$ and the normal of the ecliptic plane $\hat{K}$. The longitude of ascending node Ω is the angle between the ascending node (point where the orbit intersects the ecliptic plane in an upwards motion defined by the node line $\hat{n}$) and the direction of the First Point of Aries $\hat{I}$. The argument of perihelion ω is the angle in the orbital plane between the ascending node and the perihelion. V and R represent the velocity and the distance of the planet compared to the center of the orbit, respectively. The true anomaly θ is the angle in the orbital plane between the perihelion and direction of R.

2.1.4 Minimum Orbital Intersection Distance

To ensure a potential detection, it would be better to have the strongest signal possible. Since gravity depends on distance, if we find the smallest distance between the NEA and the spacecraft, we get the best gravitational effect possible. So the desired close approach should be happen at this distance. The Minimum Orbital Intersection Distance (MOID) is defined as the minimum possible distance between two confocal Keplerian orbits. It is the distance used in the simulations while performing a close approach. An illustration of this concept can be visualized in Figure 2.2.

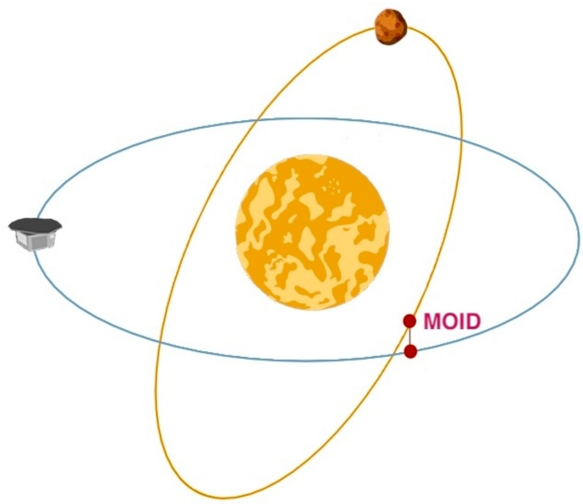

Figure 2.2: Schema of the MOID for one LISA spacecraft and a NEA orbit. The orbits of the asteroid and LISA spacecraft are shown in orange and blue, respectively. The red dots correspond to the position in each orbit, allowing the bodies to be at the minimum distance possible to each other, i.e, at their MOID.

The MOID allows us to study the best or almost best case scenario for detection. It allows for the close approach to be at the minimum distance, where the gravitational attraction is the strongest. If an asteroid is not detectable at the MOID, it won't be detectable anywhere else in the orbit since the gravitational attraction will always be smaller elsewhere. Thus, we can already exclude unsuitable candidates and focus on the potentially detectable candidates.

Nevertheless, It might not be the best scenario because the detection does not only depend on the distance but also the mass of the asteroid and the LISA geometry (configuration of the constellation at the moment of detection) as described in Section 3.2.

As the MOID is a geometrical concept between the orbits, it is not enough to simulate a close approach. As a consequence, it is also crucial to find the corresponding times in which the bodies are passing to the points in their respective orbit that allow them to be at the MOID. In this case, we calculate for each body in the close approach (one NEA and one LISA spacecraft) the corresponding mean anomalies M that allow both bodies to be at their minimum distance.

2.2 Physical Properties

The physical properties allow to define a mass which is essential for the characterization of the gravitational effect of the asteroids on the LISA constellation during a close approach.

2.2.1 Albedo

The albedo p_v is a dimensionless physical property that indicates the ratio of the incident sunlight and reflected sunlight on the surface of a body. If a body has a perfectly white surface meaning it reflects all light, it will have an albedo of 1. While, on the other hand, if a body is a perfect black body, meaning all light is absorbed, it will have an albedo of 0. The albedo is an interesting property for asteroids because it allows to estimate the size of an object from its brightness.

There are three categories for the albedo of NEAS [39]:

Category 1: $p_v \leq 0.1;$

Category 2: $0.1 < p_v \leq 0.3;$

Category 3: $0.3 < p_v \leq 1.$

The albedo for NEAs is often unknown thus, we can use the expected albedo, $p_v = 0.14$ proposed in [40]. This expected albedo is considered the standard when no measurement has been possible. We note that this value is assumed and can result in high uncertainties in the calculations of size, but we accept this principle and this value will be used in the calculation of the diameter of the NEAs in our simulations whenever the albedo is not available.

2.2.2 Absolute Magnitude

The apparent magnitude is defined as a measure of how bright an object appears from the location of the observer. As the apparent magnitude depends on the location of the observer, it is not the best concept to compare the intrinsic properties of objects at different distances. Thus the concept of absolute magnitude was created. [41]

The Absolute Magnitude H is a measure on how bright objects appear under a specific set of conditions. This concept has two definitions depending on the objects being studied. For objects outside the Solar System, the absolute magnitude is defined as the apparent magnitude an object would have when viewed from a standard distance of 10 pc. Within the Solar System, the Absolute Magnitude H is defined as the visual magnitude of an asteroid at mean brightness reduced to a distance of 1 au from the Sun and the Earth at zero solar phase angle[1]. An illustration of this definition is shown in Figure 2.3.

In daylight the human eye is most sensitive to radiation with a wavelength of about 550 nm, the

[1]Solar System bodies are illuminated by the Sun and vary brightness due to their motion as seen by the observer. The phase angle allows to describe this variation. It is the angle between the Sun and the observer measured from the body. A zero phase angle means that the observer would be seeing the body in the direction opposite to the Sun.

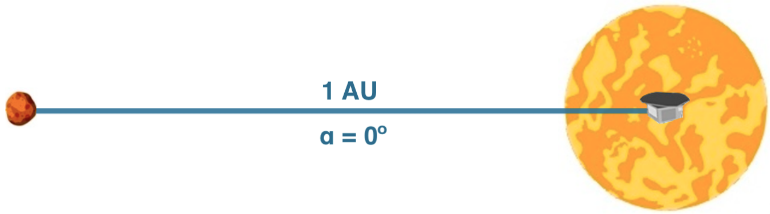

Figure 2.3: Illustration of the definition of absolute magnitude. The asteroid is placed at 1 au of both the Sun and the observer, in this case the LISA spacecraft. The solar phase angle α is 0 since the observer and the Sun are both superposed. Its absolute magnitude corresponds to 1.

sensitivity decreasing towards red (longer wavelengths) and violet (shorter wavelengths). The visual magnitude corresponding to this sensitivity of the eye which peaks at 550 nm and has a bandwidth of 88 nm [42]. The latter definition will be used in the following calculations and further ahead studies.

2.2.3 Density

Asteroids are classified according to taxonomies. These allow to group them into classes according to their reflectance spectra. Each class corresponds to one or a certain amount of reflective wavelengths on the surface of the asteroid which on the other hand provides clues unto the composition or density of the asteroid.

The asteroid taxonomy has been in development for almost 50 years but it was quickly established these classes should be described by a single letter which hints towards a mineralogical interpretation, such as the carbonaceous C, the silicaceous S, the metallic M, enstatite E and so on. In Figure F.1, we can see some of the different taxonomy classes from [43]. The density for some observed NEAs of different taxonomy classes is shown in Figure 2.4.

From observations, most NEAs lie in the silicaceous S ($\approx 55\%$) and carbonaceous C classes ($\approx 11\%$). As a consequence, we will assume the average density of $\rho = 2200$ kg/m^3 for the S class as an initial estimate of the density for computing the mass [30]. In Chapter 3, this value is only used as a placeholder since later a mass probability density function is used to deal with the lack of data for the asteroid density.

2.2.4 Diameter

A direct measurement of the size or shape of an asteroid is often unfeasible. Thus, there are several methods to estimate it. The most common method is estimation through thermal infrared observations and from the definition of photometric brightness. A diameter can be deduced from the reflected light observed assuming asteroid is a lambertian scatterer in a shape of disk [44]. This method allows to link physical properties as p_υ and H and calculate the diameter d in km:

$$d = \frac{1329}{\sqrt{p_\upsilon}} 10^{-0.2H}. \tag{2.5}$$

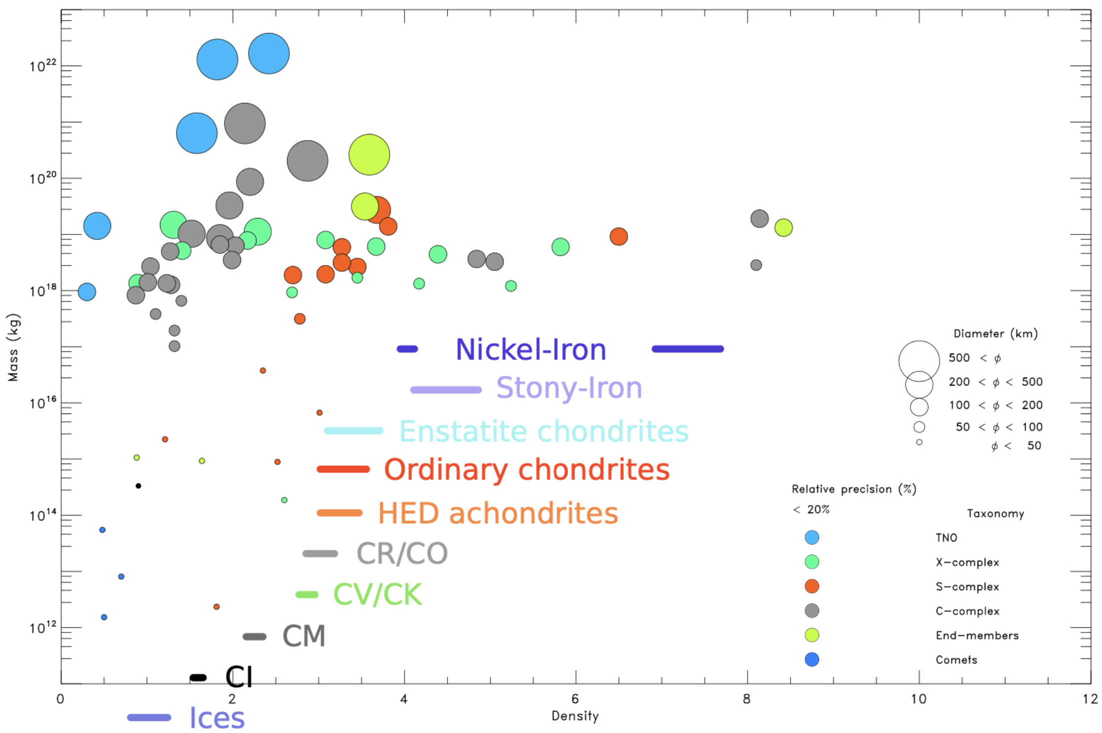

Figure 2.4: Mass vs density for some asteroids and their taxonomy classes [30]. The bodies are divided into 6 categories: Transneptunion Objects TNOs (light blue), comets (blue), and Asteroids divided into four taxonomic groups: S in red, C in grey, X in green, and End-members in yellow. Asteroids which taxonomy is unknown are plotted in black. The size of the symbols is a function of the object diameters. The typical range densities for some different compositions are displayed in different colors with the range line and corresponding name next to it. The density is shown as a normalized density compared to the water density $\rho_{\text{water}} = 1000\ \mathrm{kg/m^3}$

This formula will be important to estimate the diameter of the asteroids which do not provide such measurement.

2.2.5 Mass

The determination of the mass of an asteroid relies on the analysis of its gravitational effects on other objects close by, typically other asteroids. Nevertheless, these close approaches are rare and only a few accurate mass estimations exist.

The typical approach to define the mass m is using the ratio between the density and volume of the asteroid under the assumption that the volume can be modeled as a sphere of diameter d.

$$m = \frac{\rho}{V} = \frac{1}{6}\pi\rho\, d^3. \tag{2.6}$$

where ρ the density of the asteroid in kg/m^3 and V its volume in m^3. This equation will be used to estimate the mass in kg of the asteroids for which it has not been evaluated.

2.3 Signal

Here, it is presented how a signal is created and obtained from the LISA's detectors following a close approach. This signal is then used to draw conclusions on the detectability of NEAs using gravitational attraction and to determine their orbital and physical parameters.

2.3.1 Interferometry

As the LISA constellation moves along its orbit, the 3 spacecrafts are linked by their laser beams. In Figure 2.5, an illustration of the apparatus used in the LISA constellation and arm link between two spacecrafts is shown.

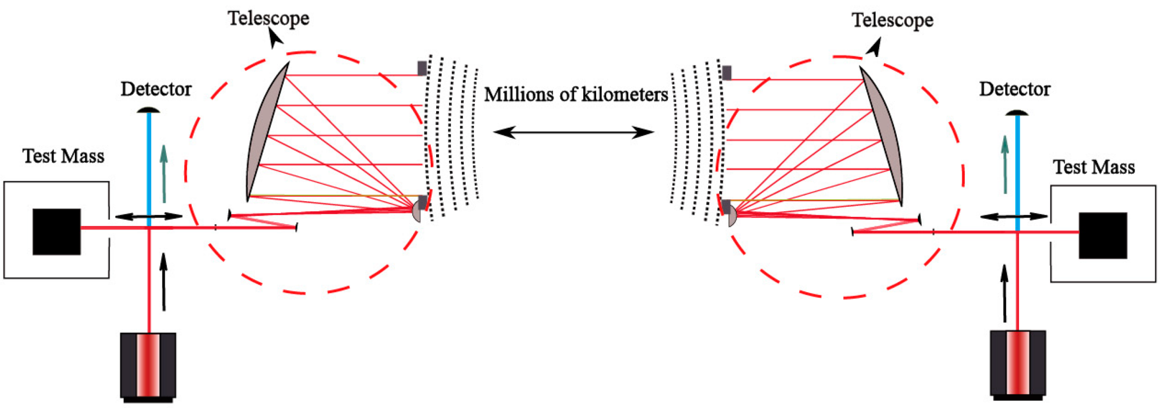

The arrows indicate the direction of propagation of the laser beam.

Figure 2.5: Interferometry between two spacecrafts of the LISA constellation [45]

As seen in Figure 2.5, there is a laser in each spacecraft. It will create a laser beam which will be reflected by the test mass into the telescope. In the telescope, the beam is expanded so that it can be able to travel the arm length distance (2.5 Mkm). In the end, it will be received by the telescope on the other spacecraft and the phase of the arriving light beam is going to be compared and checked to a local laser beam through the optical phase-locked loop system to detect potential changes due to gravitational waves. [45]

When the asteroid is coming closer to a spacecraft, it will start attracting the test mass in the spacecraft. At a point in time, the asteroid will be its closest to the spacecraft. We define this point in our simulations as the MOID (smallest distance possible between the two bodies) so that we have the best signal possible. The gravitational attraction due to the close approach induces an acceleration reaching a maximum at the MOID, which then decreases gradually. Evidently, this motion is described by the Newton's law of universal gravitation [46]. Because the LISA detection system is based on interferometry, what we will measure is the phase shifts due to a motion of the test masses. The induced acceleration will cause a variation in the velocity of the test mass, initially at rest, and as a consequence a Doppler shift will appear which creates a difference in the phase of the laser beams and a signal at the detectors. Using the 3 arms configuration (3 spacecrafts linked) and their joined information, it is possible to reconstruct a 3D signal and study its properties [47].

2.3.2 LISA Reference Frame

The principle of detection of LISA is based on a signal generated by the change in velocity, more precisely a phase difference on the laser arms (Doppler effect) due to the motion of the test masses [48]. In Figure 2.6, two pairs of arm links are shown: $(\tau_{13}, \tau_{32}, \tau_{21})$ and $(\tau_{31}, \tau_{12}, \tau_{23})$ corresponding to the emission and reception of light by the spacecraft, respectively.

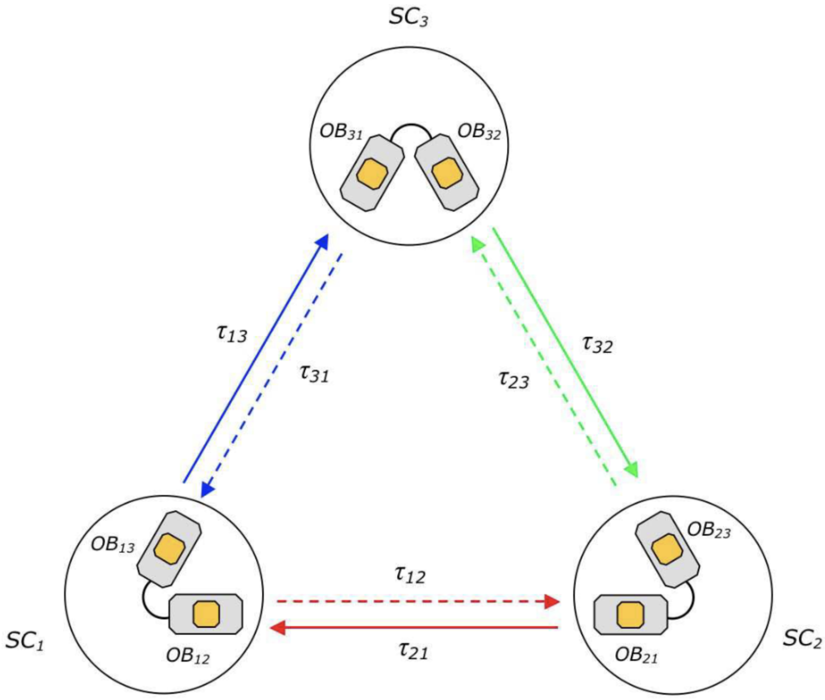

Figure 2.6: Definition of laser arms for LISA constellation. [49]. Each spacecraft (S/C) contains two optical benches (OBs) (grey rectangle), each with one test mass (yellow square) acting as a mirror, which will send (bold) or receive (dotted) the laser light from the other two spacecrafts. The laser arms are named τ_{ij} where i corresponds to the S/C emitting the laser and j the S/C receiving the laser. The same convention is used for naming the OBs.

In order to generate the signal being detected, the velocity needs to be converted to the LISA's reference frame, a reference frame defined by the three directions of LISA's arm links or laser arms. The origin of the reference frame is the same as the heliocentric ecliptic coordinate system, thus the change in velocity is converted from the heliocentric ecliptic coordinate system to LISA reference frame by just making the projection of the velocity into the different arm links. Following the standard LISA conventions, the directions of projection for the LISA's reference frame are defined in the clockwise direction and named after the spacecraft opposing the laser arm [50]:

$$\begin{aligned}\vec{n}_1 &= \vec{e}_{\tau_{32}};\\ \vec{n}_2 &= \vec{e}_{\tau_{13}};\\ \vec{n}_3 &= \vec{e}_{\tau_{21}}.\end{aligned} \tag{2.7}$$

In order to be able to find the directions of the LISA's reference frame $(\vec{n}_1, \vec{n}_2, \vec{n}_3)$, we need to calculate the position of the spacecrafts at the moment of the close approach and define the arm link vectors. Then, the change in velocity on the test masses is projected into the LISA arm links

$$\begin{aligned}&\Delta v_{12} = \Delta\vec{v}_1 \cdot \vec{n}_2, \qquad \Delta v_{21} = \Delta\vec{v}_2 \cdot \vec{n}_1, \qquad \Delta v_{31} = \Delta\vec{v}_3 \cdot \vec{n}_1,\\ &\Delta v_{13} = \Delta\vec{v}_1 \cdot \vec{n}_3, \qquad \Delta v_{23} = \Delta\vec{v}_2 \cdot \vec{n}_3, \qquad \Delta v_{32} = \Delta\vec{v}_3 \cdot \vec{n}_2.\end{aligned} \tag{2.8}$$

where Δv_{ij} is the change in velocity of the test mass in S/C i with arm link j and projected in the direction j.

2.3.3 Time Delay Interferometry

The first step in the LISA data analysis is to combine data from the individual instrument elements in order to produce the data to be analysed. Each spacecraft will collect and interfere light from two different lasers coming from the other spacecraft, as well as emit a laser beam. In the end, as the lasers are not perfect, they will oscillate in frequency, and these oscillations create the laser frequency noise. Earth-based detectors which have equal-arm interferometer detectors can cancel these laser frequency fluctuations by comparing phases of split beams propagated along the equal, non-parallel arms of the detectors. Nevertheless, in LISA such technique is not possible. The spacecrafts are moving in their orbits which will make that the arm-lengths or distance between the three spacecrafts are not the same throughout the time. In fact, the larger the difference between the arm-lenghts, the larger will be the magnitude of the laser frequency fluctuations affecting the detectors. And on top of it, this laser frequency noise is comparable to the amplitude of the gravitational waves to be detected.

To overcome this problem, a post-processing technique called Time Delay Interferometry (TDI) is applied. This technique consists in the generation of virtual equal arm Michelson Interferometers[2] which drastically reduce the impact of laser frequency noise. The TDI technique combines the signal generated by each laser on each spacecraft in a way that allows to deal with the noise and imperfections in the armlengths. It takes advantage from the fact that the same noise will affect different measurements at different times, meaning, even when there is no signal, the laser frequency noise will be there. As a consequence, it is possible to time-shift and recombine the measurements in order to cancel the noise and construct laser noise-free virtual interferometric signals [51]. In Figure 2.7, this TDI technique is explained for the beams arriving in S/C 1.

[2]The Michelson interferometer is a common configuration for optical interferometry invented by the 19/20th-century American physicist Albert Abraham Michelson. It consists in splitting a light source into two arms with the help of a beam splitter and reflect the result using a mirror to the same place. The two arms will then combine using the superposition principle and the changes in the resulting signal will allow to detect the desired entity.

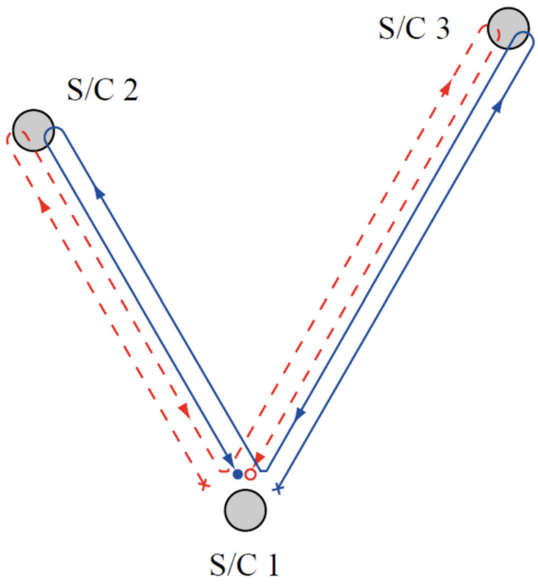

Figure 2.7: Illustration of TDI technique for S/C 1 [51]

The blue line represents a laser beam emitted from S/C 1 that goes bouncing in S/C 3 and S/C 2 and comes back to S/C 1. The red dotted line represents a fictional beam that does the same path but in an inverse way, first S/C 2 and then S/C 3 coming back to S/C 1. Even if the arm-lengths between spacecrafts are different, the total travel path for the real and fictional laser beams is the same, meaning that they will come back to S/C 1 with the same phases and the laser frequency fluctuations will be able to cancel each other by destructive interference as in the ground detectors (here represented by the filled and empty circles showing different phases at the end of both paths).

The resulting signals are characterized by new variables or channels being the most often used the Michelson TDI variables, X, Y and Z which resemble the typical variables or channels for the data stream using a standard Michelson interferometer. The TDI variables are defined [52]:

$$X(t) = [s_{21}(t) - s_{31}(t)] - [s_{21}(t - 2L_3/c) - s_{31}(t - 2L_2/c)]; \tag{2.9}$$

$$Y(t) = [s_{32}(t) - s_{12}(t)] - [s_{32}(t - 2L_1/c) - s_{12}(t - 2L_3/c)]; \tag{2.10}$$

$$Z(t) = [s_{13}(t) - s_{23}(t)] - [s_{13}(t - 2L_2/c) - s_{23}(t - 2L_1/c)]. \tag{2.11}$$

where s_{mn} is the phase shift measurement made at spacecraft n of the light received from spacecraft m, L_i is the length of the arm opposite to the spacecraft i and c the speed of light. The variables measure, for each spacecraft, the instantaneous phase shift on the test masses for both laser links and a delayed version of the phase shift which cancels out the noise.

Nevertheless, for scientific analysis, the variables X, Y and Z are not the best variables since they are not statistically independent. It has been shown that under some simplifying assumptions that these Michelson variables can be combined to produce the so-called quasi-orthogonal TDI channels: A, E, and T. These are defined as [48]:

$$A(t) = \frac{1}{\sqrt{2}}(Z - X), \qquad E(t) = \frac{1}{\sqrt{6}}(X - 2Y + Z), \qquad T(t) = \frac{1}{\sqrt{3}}(X + Y + Z). \tag{2.12}$$

In theory, A and E contain the data stream in which the signal may be detected and T acts as an empty channel or a channel where the signal is somewhat suppressed.

2.4 Noise

Sensitivity curves are useful for making a quick assessment of what signals may be detectable. Since we currently do not have the true noise estimation to use in our calculations, we can base ourselves in the sensitivity curve presented in Figure 1.2 to assess the noise for the simulations. The noise in this picture is represented by the green (containing the LISA related noises) and dotted black curve (also considering the galactic background). We will focus on the noises produced by the LISA constellation itself (green curve) in our simulations.

The instruments in the LISA constellation measure strain through free falling test masses. In order for the masses to be in free fall, there is a Disturbance Reduction System (DRS) acting on them, which attempt at minimizing the external and residual accelerations due to extraneous forces other then gravity acting on them. This system generates a noise in the low frequency spectrum, S_{acc}, described by [6]

$$S_{\text{acc}}^{1/2}(f) \leq 3 \times 10^{-15} \; \frac{\mathrm{m\,s^{-2}}}{\sqrt{\mathrm{Hz}}} \sqrt{1 + \left(\frac{0.4\,\mathrm{mHz}}{f}\right)^2} \sqrt{1 + \left(\frac{f}{8\,\mathrm{mHz}}\right)^4}. \tag{2.13}$$

where f is the frequency in mHz.

Furthermore, we determine the separation between the test masses due to interferometry. The total system responsible for this is called the Laser Interferometry Measurement System (IMS) and this system determines the limitation of the sensitity in the high frequencies spectrum due to internal noises. The noise in this system, S_{IMS}, is described by [6]

$$S_{\text{IMS}}^{1/2}(f) \leq 1.5 \times 10^{-11} \frac{\mathrm{m}}{\sqrt{\mathrm{Hz}}} \sqrt{1 + \left(\frac{2\,\mathrm{mHz}}{f}\right)^4}. \tag{2.14}$$

where the frequency is again defined in mHz.

Thus, we define the total noise S_n in our simulations [6]

$$S_n(f) = \frac{10}{3L^2} \left(S_{\text{IMS}}(f) + \frac{4S_{\text{acc}}(f)}{(2\pi f)^4}\right) \left(1 + 0.6 \left(\frac{f}{19.09\,\mathrm{mHz}}\right)^2\right). \tag{2.15}$$

where $L = 2.5$ million km is the armlength between two test masses and the frequency is in mHz.

For completeness, the total sensitivity curve is obtained by adding the contribution coming from the galactic foreground, S_c, described in [53]. The galactic foreground is caused by the combination of signals of binary systems in the Milky Way and its a source of noise for the measurements. Its expression is displayed in Appendix F. Because this is a non-stationary source of noise, depending on the time of observation, it goes down as the mission progresses and the impact on the sensitivity curves is small, we ignore it in the simulations performed.

2.5 Signal-to-Noise Ratio

When doing signal processing and assessing detectability, it is preferable to express the signals and noise in the frequency domain, more specifically in terms of Fourier Transforms (FT) and Power Spectral Density (PSD). The FT is a reconstruction of the signal in the frequency domain by re-writing it as a sum of sinusoidals of certain frequencies. The PSD, on the other hand, is the distribution of a signal's power over frequency and tells us how much power is contained in a given frequency band, allowing us to better understand the characteristics of the signal in question. For the analysis performed in this work, both concepts are used.

We can rewrite the time-series signal $x(t)$ in the frequency domain $\tilde{X}(f)$ using the FT definition [54]:

$$\tilde{X}(f) = \int_{-\infty}^{\infty} x(t) e^{-2\pi i f t} dt. \tag{2.16}$$

The FT of the signal is linked to the PSD using Parseval's Theorem [54]:

$$\mathrm{PSD}_x(f) = \lim_{T\to\infty} \frac{1}{2T} |\tilde{X}(f)|^2. \tag{2.17}$$

where T is the time interval for the limit.

In the analysis done in this work, we convert the interferometric signal $x(t)$ in the detectors to frequency domain using the FT. Furthermore, its PSD is calculated. As the detection depends on the signal, but also on the noise that is going to be distorting it, it is also important to analyse the noise. The analytic noise $n(t)$ is described in the LISA requirements documentation. It is written in the frequency domain, and its PSD is already computed. The expected analytical PSD of the noise, PSD_n, in each of the X, Y and Z channels after the post-processing technique TDI is [55]:

$$\mathrm{PSD}_n(2\pi f) = 64 \sin^2(2\pi f L)\, \sin^2(4\pi f L)\, (S_{\text{IMS}}(2\pi f) + (3 + \cos 4\pi f L) S_{\text{acc}}(2\pi f)) \,. \tag{2.18}$$

As the variables to be used in this work are A, E and T, the PSD of the noise to be used in the analysis is the one corresponding to these channels. It can be obtained from the PSD of the noise in X, Y, T as derived in [56]:

$$\begin{gathered}
\mathrm{PSD}_{n_A} = 32 \sin^2(2\pi f L)\, \sin^2(4\pi f L) \left((2 + \cos(2\pi f L)) S_{\text{IMS}}(2\pi f) + (3 + 2\cos(2\pi f L) + \cos(4\pi f L)) \frac{2 S_{\text{acc}}(2\pi f)}{(2\pi f)^4} \right); \\
\mathrm{PSD}_{n_E} = \mathrm{PSD}_{n_A}; \\
\mathrm{PSD}_{n_T} = 64 \sin^2(2\pi f L)\, \sin^2(4\pi f L) \left((1 - \cos(2\pi f L)) S_{\text{IMS}}(2\pi f) + 8 \sin^4(\pi f L) \frac{S_{\text{acc}}(2\pi f)}{(2\pi f)^4} \right).
\end{gathered} \tag{2.19}$$

where PSD_{n_c} is the PSD of the noise in channel c.

Having both the PSD of signal and noise, it is possible to compute the quantity allowing to assess the detectability. The Signal-to-Noise ratio (SNR) is a dimensionless measurement parameter used in the fields of science and engineering to compare the level of the signal to the level of background noise. By comparing both, it is possible to understand if the signal can be detected in a datastream polluted by noise. For the LISA constellation, the SNR is mathematically defined as [55]:

$$\mathrm{SNR}^2 = 8\int_0^{f_{\text{max}}} df\, \frac{\mathrm{PSD}_x(f)}{\mathrm{PSD}_n(f)}. \tag{2.20}$$

where f_{max} is a maximum frequency gives the range of integration for the SNR. The signals of asteroids are in the low frequency domain, so it is not needed to integrate above a certain f_{max} as the high frequency spectrum will be flooded with noise. [55]

As there are three channels (A, E and T) collecting different signals,there will be three different SNRs computations. Due to the fact that they are orthogonal and linearly independent channels, it is possible to sum up their contribution to obtain the final SNR of the simulation [56]:

$$\mathrm{SNR}^2 = \sum_i^{[A,E,T]} 8\int_0^{f_{\text{max}}} df\, \frac{\mathrm{PSD}_{x_i}(f)}{\mathrm{PSD}_{n_i}(f)} = \mathrm{SNR}_A^2 + \mathrm{SNR}_E^2 + \mathrm{SNR}_T^2. \tag{2.21}$$

As there is no intuition on how to choose an adequate minimum SNR threshold for asteroid detection through gravitational effects, we adopt the literature value of SNR$=5$. A SNR of 5 corresponds to a statistical significance of 5σ, meaning that the probability of a measurement done being a statistical fluctuation is and not the signal of an asteroid passing by is 0.00006% [57]. In Chapter 3.4, we conclude that the minimum value of SNR$=5$ is quite optimistic for the detection, meaning that, in the future, it might need be adjusted to SNR$=10$. Nevertheless, SNR$=5$ is the value used throughout this work.

2.6 Simulation

Now that all the concepts have been explained, a simulation is constructed. The objective of the simulation is to assess the detectability of the asteroid following a close approach to one of the spacecraft. Thus, all the close approach is simulated and a final analysis is done using the SNR quantity. The simulation pipeline is decomposed into several steps as shown in Figure 2.8.

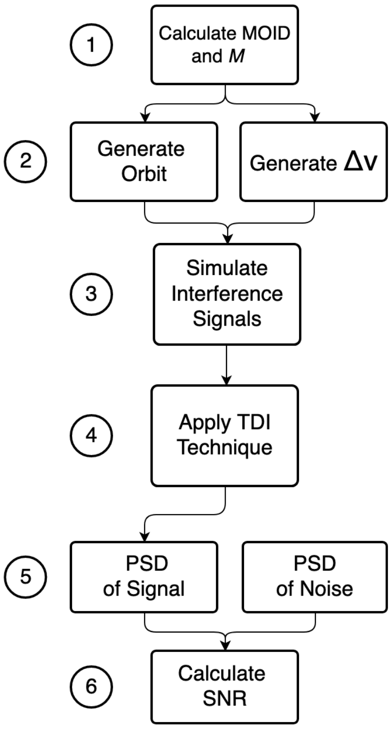

Figure 2.8: Flow diagram of the simulation steps

These steps are:

1. *Calculate MOID and* M: The MOID and respective position of the bodies in their orbit are calculated in order to create a close approach at the minimum possible distance.

2. *Generate Orbit* and *Generate* Δv: The LISA constellation orbits are simulated for the close approach. From that, the laser arms which depend on the position of the three spacecraft can be extracted. The gravitational effect is simulated from the close approach and the induced velocity Δv on the test masses is also retrieved. Having the induced velocity and laser arm vectors, the projection of the change in velocity on the test masses can be simulated.

3. *Simulate Interference Signals*: Since the variation on the velocity of the test masses is now known, it is possible to calculate the Doppler shift on the laser arms and find the interference pattern in the detectors.

4. *Apply TDI Technique*: As the interference pattern is known, the TDI post-processing technique is applied to get rid of the laser fluctuation noise and obtain a clearer signal.

5. *PSD of Signal* and *PSD of Noise*: The calculated time-series signal is then converted to the frequency domain using the FT and PSD techniques explained in Chapter 2.5 for analysis purposes. The PSD of noise is numerically simulated using the analytic expressions defined in the LISA requirements document.

6. *Calculate SNR*: The signal and noise are then used to calculate the SNR quantity, allowing us to assess the detectability of the asteroid during the close approach to the spacecraft.

The code implementation and the *Python* packages used are described in Appendix A.

2.6.1 Example

We simulate a close approach during a certain time[3] between one of LISA's spacecraft (in this case S/C 2)[4] and Asteroid 4179 Toutatis, a PHA due to its close proximity to the Earth's orbit. Its classical orbital elements and mass[5] at epoch 60200 are:

$$a = 2.54 \text{ au}, \quad e = 0.62, \quad i = 0.0079 \text{ rad}, \quad \Omega = 2.19 \text{ rad}, \quad \omega = 4.85 \text{ rad}, \quad m = 2.12 \times 10^{13} \text{ kg}.$$

The MOID between S/C 2 and the asteroid as well as the mean anomalies corresponding these orbital positions are:

$$\text{MOID} = 3.79 \times 10^{-4} \text{ au}, \qquad M_{NEA} = 6.19 \text{ rad}, \qquad M_{S/C\,2} = 2.74 \text{ rad},$$

where M_{NEA} is the value of the mean anomaly for the asteroid and $M_{S/C\,i}$ for S/C i.

After knowing these quantities, we simulate a close approach, as seen in Figure 2.9.

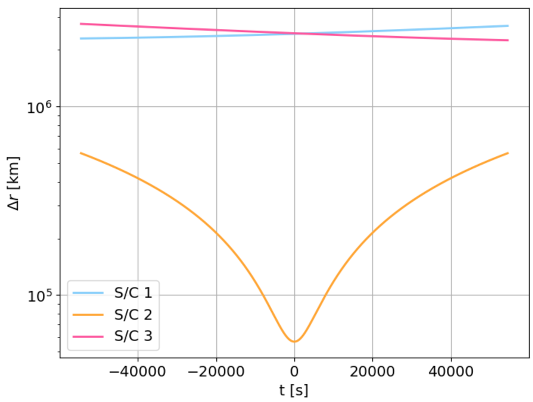

Figure 2.9: Magnitude of distance between S/C 2 and Asteroid 4179 Toutatis during a close approach

[3]Since the computational power to perform these simulations is not unlimited, we have to define a finite duration to perform it. We use the method described in Appendix C in order to define this duration or simulation time.

[4]The three spacecrafts are numbered according to their corresponding orbital elements that can be found in Appendix F.

[5]These classical orbital elements were obtained from the Near-Earth Object Coordination Centre (NEOCC) database, accessible in `https://neo.ssa.esa.int/`. The mass is calculated from Expression 2.6 using a density of $\rho = 2200$ kg/m^3. The value of diameter was calculated from Expression 2.5. The absolute magnitude was found in the database and the albedo of reference, $p_v = 0.14$, was used.

At $t = 0$ s, both bodies will be at the orbital positions defined by M_{NEA} and $M_{S/C\,2}$ corresponding to the minimum distance between the two, the MOID. Then, as both bodies continue to move along in their orbits, the distance between them increases again. As expected, as the asteroid is coming closer to S/C 2, it will start attracting its test masses. This attraction or change in acceleration of the test masses reaches a maximum at $t = 0$ s, the time at which the MOID occurs, and then decreases gradually as the distance between them increases again. This gravitational effect is displayed in Figure 2.10.

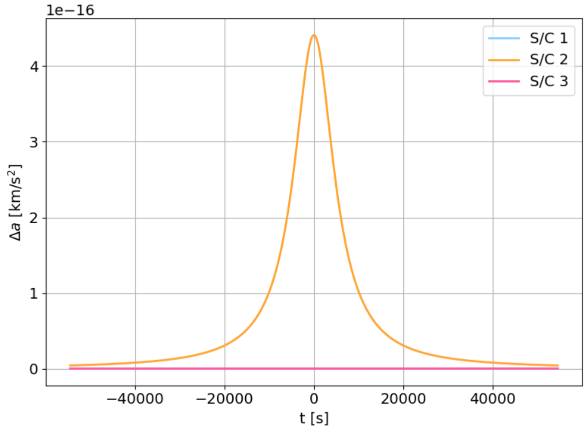

Figure 2.10: Magnitude of gravitational effect due to close approach between S/C 2 and Asteroid 4179 Toutatis. The curves of S/C 1 and S/C 3 are superposed.

The change in acceleration seems rather small (order of 10^{-16} km/s^2), but we cannot forget that LISA was designed to feel these very small variations of displacement like the ones caused by this gravitational effect.

The LISA interferometer detects the phase shift of the laser light. The phase shift is directly linked to the Doppler shift generated by the induced velocity on the test masses due to the close approach along the arms. Knowing the position of the LISA constellation, we figure out the direction of the laser arms, which allow to calculate the projection of the induced velocity by the close approach. These projections are displayed in Figure 2.11.

As the induced velocity in the arms is known, it is now possible to generate the signal in detectors and apply the TDI post-processing technique to get rid of the laser fluctuation noise. As mentioned in Chapter 2.3.3, the variables A, E and T are used for a better signal analysis. In Figure 2.12, the signal in these three channels after applying the TDI technique is shown.

For the current close approach, the channel that captured the most signal was E and the intensity of the channel T is around a factor 1000 smaller, thus it is clearly visible that T is highly suppressed signal channel. If no close approach was detected, the signal in all the three channels would be close to none.

Since the characterization of the LISA noise is in the frequency domain, for signal processing purposes, it is better to transform the time-series signal into a signal in the frequency domain using the FT and PSD techniques. In Figure 2.13, the obtained PSD for the signals in the three TDI channels and the noise defined using the LISA requirements in Chapter 2.5 are shown.

The SNR is quite related with the plots displayed in Figure 2.13. It is directly proportional to the area between the two curves, as seen from the Expression 2.21 defined in Chapter 2.5. f_{max} defines the

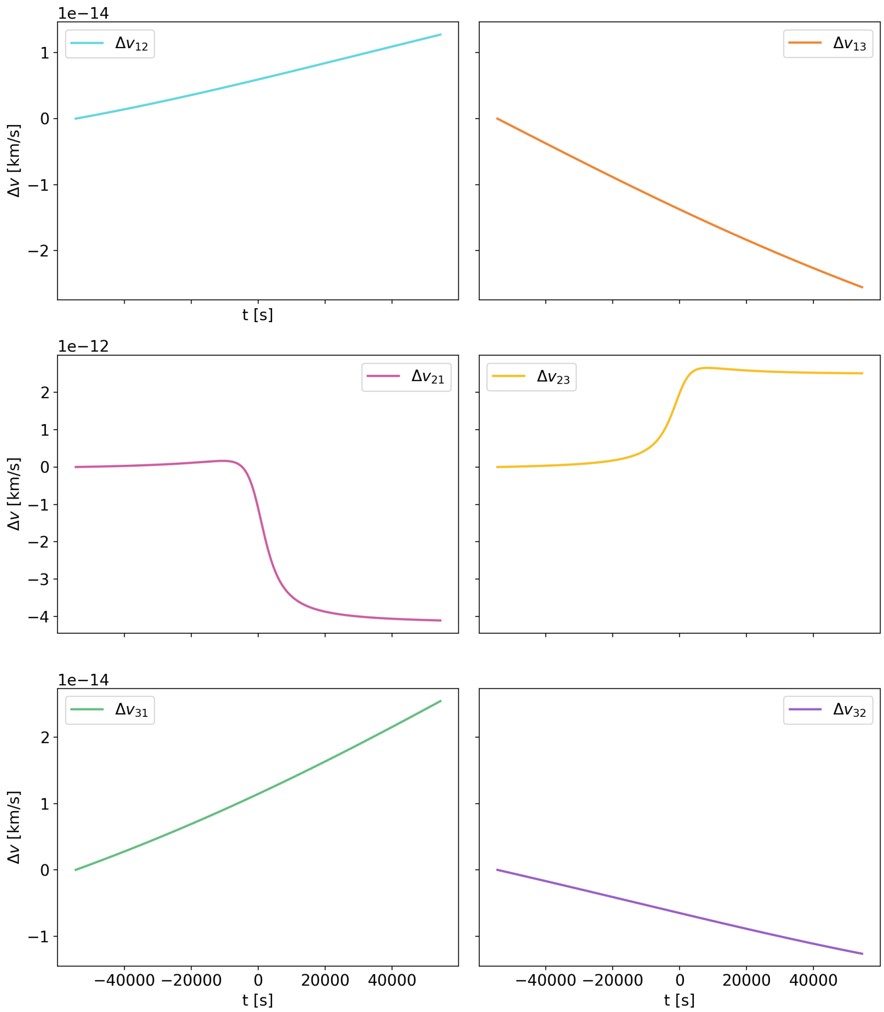

Figure 2.11: Projected induced velocities into LISA reference frame due to close approach between S/C 2 and Asteroid 4179 Toutatis

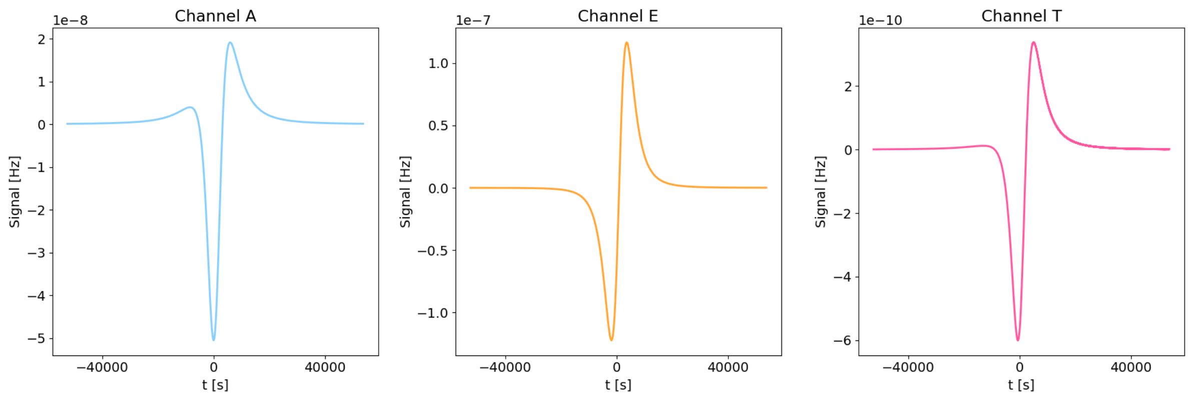

Figure 2.12: Signal after TDI for the close approach of Asteroid 4179 Toutatis to S/C 2

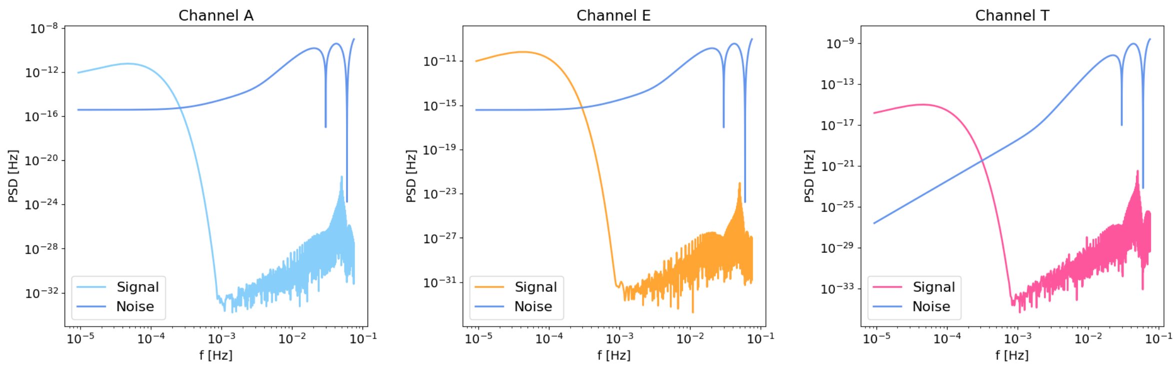

Figure 2.13: PSD of signal and noise for the close approach between Asteroid 4179 Toutatis and S/C 2

range of interest for the integration which is where the signal is above the noise. Whenever the signal is below the noise, it means that the data stream will be flooded in noise and it will be quite difficult to retrieve it. For this close approach, the SNR obtained is:

$$\mathrm{SNR}^{\mathrm{S/C}\ 2}_{4179\ \mathrm{Toutatis}} = 27746.48. \tag{2.22}$$

As it is above the minimum SNR, we can consider that if this close approach would happen in real life, we would be able to detect it quite clearly. In the next chapters, the simulation is used as the basic block from which we build up the results. In the studies to choose the suitable candidates for detection (Chapter 3.2) and assessment of the probability of detection (Chapter 3.3) use the SNR as the last step and these values are analysed in diverse conditions. On the other hand, for the uncertainty in the measurement study (Chapter 3.4), the SNR is replaced by a calculation of the Fisher matrix, which ends up being the last step of the simulation for each asteroid.

Chapter 3

Studies and Results

3.1 Hypothesis

3.1.1 Fictitious NEA Population

While more than 30000 NEAs have been found so far (as shown in Figure 1.4), the current NEA distribution is considered quite incomplete. It is thought that only brightest asteroids ($H \sim 14$) have been fully discovered which skews already the population of detected NEAs. Yet, the remaining population ($H > 14$) is considered highly skewed as it was constructed from different asteroid survey programs with considerably different detection techniques which are not independent of H. In the end, it means that, additionally, the current population of NEAs contains an observational bias. [58]

During activities related to ESA's Space-Situational Awareness (SSA) programme, a tool was developed to generate a NEO population based on the debiased model proposed in [59] and simulate their observations. This tool is called *NEOPOP*[1].

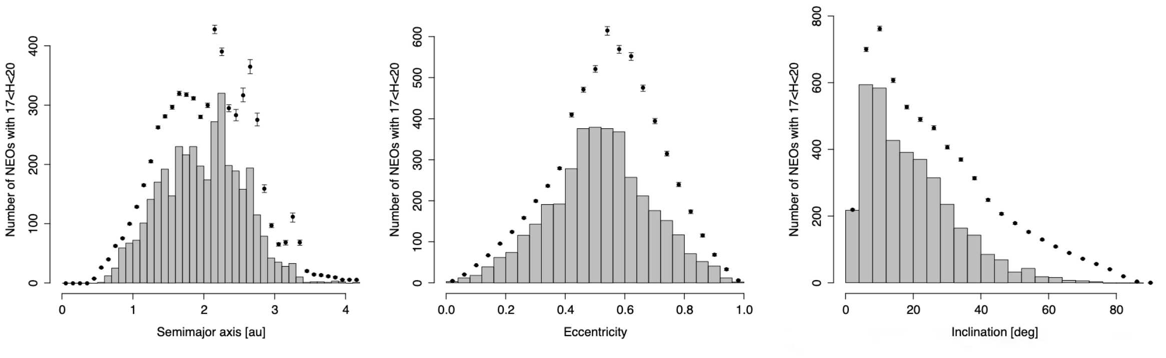

Figure 3.1: Debiased model for the distributions of the a, e and i for NEAs with $17 < H < 20$ [59]. The detected distribution is displayed by the gray bars while the debiased model predicts that the corresponding height of the bars should be given by the points with an uncertainty provided by the error bars.

[1] The NEOPOP generator tool can be easily accessed in `https://neo.ssa.esa.int/neo-population-generator`

For all the studies presented in the next sections, we took advantage of the population generation feature of the NEOPOP tool to generate a NEAs population so we can study it. Like that, we are able to synthesise a bigger population than the one found through observations as well as to eliminate the observational bias which could impact the results of the studies. The generated population is composed by more then 50000 asteroids for $17 < H < 25$. The orbital elements and physical properties of some of these asteroids can be found in Appendix F.

3.1.2 Launch Date

As of 25 January 2024, LISA was adopted, meaning that ESA recognised that the mission concept and technology are sufficiently mature, giving a green light to its construction. The launch date of the full constellation is fixed for mid 2035 [60], but it is not fully settled yet. As such, a flexible launch date concept was adopted. A random initial state of the LISA constellation defined in Appendix F is used as a starting point for the simulations. And then, the LISA constellation is shifted so that it matches the MOID position for the tested asteroid at all times.

3.1.3 Kepler Orbits

All orbits used in the simulations are Kepler orbits. In reality, the orbits of the LISA constellation and the asteroids are not Kepler orbits. Even though, the orbits for the LISA constellation were designed to minimize non-gravitational perturbations[2], it will still change over the period of its mission lifetime mainly due to the gravitational attraction caused by the Earth. Additionally, for the NEAs' orbits, other phenomena can be expected as perturbation caused by solar wind pressure and gravitational pull of other Solar System's bodies. On top of these, small asteroids $(10 \text{ cm} \leq d \leq 10 \text{ km})$ suffer from an additional effect called Yarkovsky effect. The Yarkovsky effect causes rotating asteroids to drift widely over time, making it hard to predict their long-term orbits [61]. All of these effects are not taken into account during the simulations.

3.1.4 LISA Position and Motion

It is assumed throughout the simulations that the position and motion of the LISA constellation is known perfectly all the time. Thus, the probability of detection and uncertainties of the measurements are overestimated. In reality, it is predicted that the position of LISA will be known to a few kilometers and the velocity to a few meters per second [62], which may not change much the results nor make such an overestimation of the results.

[2]By being in an orbit relatively similar to Earth's orbit, LISA can be shielded from non gravitational perturbations like the solar wind pressure. Additionally, the inclination of LISA's triangle was chosen to minimize the gravitational impact of other bodies on the LISA spacecrafts and diminish the average rate of change of the lengths of the arms of the triangle over the five year operations period of the mission [5].

3.1.5 Probability Density Functions of Physical Properties

In Section 3.3, the mass independent probability of detection for an asteroid or groups of asteroids is calculated. To get rid of the mass, the mass dependent probabiltiy of detection is integrated over a mass probability density function for the fictitious population. In order to calculate this mass probability density function, we based ourselves in Equation 2.6 to compute the mass, and we related it to the probability density functions of the physical properties used to compute it: the albedo p_v, absolute magnitude H and density ρ.

Due to the the lack of information in the matter, it was assumed that the three physical properties are statistically independent. Additionally, since there is only a limited amount of measurements for the density of NEAs, two probability density function models were assumed: a uniform distribution and a gamma distribution. Detailed explanations are provided in 3.3.1.

3.1.6 Close Approach and Sphere of Influence

A simulation assumes a single close approach between one NEA and one spacecraft which as seen as point particles. It means that it can be modeled as a two-body interaction and we can draw a sphere of influence around the body. This hypothesis was used in all simulations, especially in Section 3.3. Nevertheless, the complexity of the LISA system and some of the results of the study done in Section 3.3 showed that it is not always the case (see Appendix D: Deviation from the Sphere of Influence).

3.2 Choosing Suitable Candidates for Detection

The first study assesses which asteroids could be interesting candidates for detection. It would be a waste of computational resources to probe the full population as not all asteroids may be detectable. Therefore, it becomes important to draw some criteria to allow to predict beforehand if an asteroid could be potentially detected.

Since the gravitational effect follows Newton's law of gravitation, quantities such as the mass and MOID are analysed firstly. Then, different 3D geometries of the LISA constellation at the close approach are tested. The LISA 3D geometry consists of the plane of the constellation to the orbit of the asteroid and is a relevant criteria as it defines the direction of the laser arm links and affects the interferometric signal. From these criteria, it is possible to evaluate the asteroid and determine if it is worth to test it.

3.2.1 Mass and MOID

To be able to draw the minimum mass and MOID for detection, the current observable population is studied. For each asteroid, a close approach to one spacecraft is simulated (S/C 2) and the SNR is found. The strength of the signal is directly related to the SNR, so the greater the signal, the greater the SNR. The signal is generated by the gravitational effect of the close approach, so it is possible to deduce immediately the effect of the two features: the bigger the mass is or the smaller the MOID is the bigger the SNR is.

Out of the 34712 NEAs, only 120 corresponding to 0.35% of the population had a SNR above the minimum threshold of detectability (SNR $= 5$) for a close approach with S/C 2. The mass and MOID for the detected asteroids are shown in Figure 3.2. Note that for some of these asteroids, their masses were calculated through Equation 2.6 using $\rho = 2200$ kg/m^3 and $p_v = 0.14$ whenever there was a lack of measurements for these quantities.

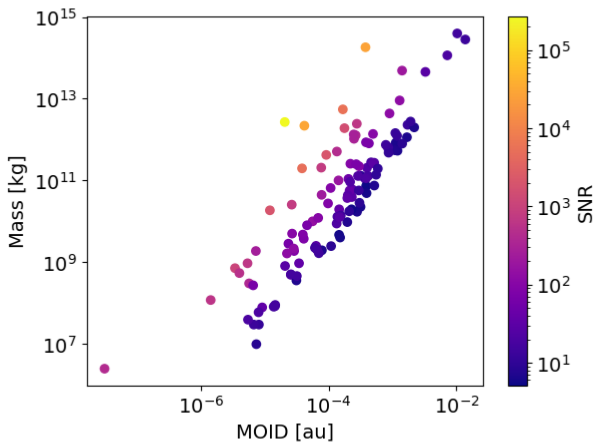

Figure 3.2: SNR, mass and MOID for the asteroids with SNR ≥ 5 for the observed population of NEAs. Each point corresponds to a tested asteroid. The color code corresponds to the SNR for that same asteroid. The red line is the threshold line relating mass and MOID and an asteroid containing a MOID and mass above it can be considered a potential detectable candidate.

3.2.2 LISA Geometry

Since the signal is obtained from interferometry between the three spacecraft and that it is captured along the arm-link directions, it is clear that the direction in which the asteroid passes close to the spacecraft will have an impact in the signal obtained. The signal captured when the asteroid passes parallel to the arm is forcibly different to the one captured when the asteroid passes perpendicularly to the arm. As such, another variable to be studied is the LISA geometry, corresponding to the position of the constellation and arm link directions at the moment of the close approach. As certain geometries allow to pick up more signal than others, to test this, the direction of the MOID was fixed and the orbit of the asteroid was rotated by an angle γ around this axis of rotation, as illustrated in Figure 3.3.

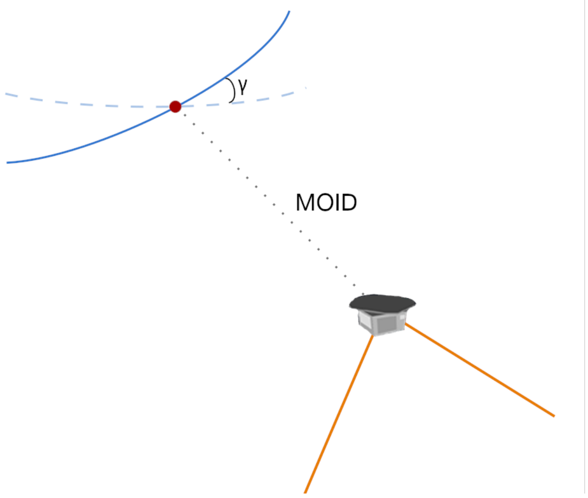

Figure 3.3: Rotation of NEA's path around the MOID by angle γ. The original orbital path is displayed with the strong blue while the rotated path is shown in dashed light blue. γ is the angle of rotation around the axis defined by the MOID and in dotted grey the axis of rotation defined by the MOID is shown. The red point corresponds to the MOID point for the asteroid and it is common for the both orbital paths. The armlinks with the other LISA spacecraft are shown in orange.

In Figure 3.4, we can see the variation of the SNR for Asteroid 4179 Toutatis for the rotation γ of its initial orbit around the axis defined by the MOID. It is possible to see that the original orbit (red dot) is passing in an unfavourable way for the interferometry and that, if the orbit was rotated by around $250°$, the collected interferometric signal would be much greater, allowing for a clearer detection. For this asteroid, the value for the original orbit (SNR $= 27746.48$) is actually closer to the possible minimum SNR$_{min} = 25183.59$ and its maximum happens around $250°$ and is more than twice as big, SNR$_{max} = 63314.80$.

As all asteroid orbits and close approaches are different, it is not possible to set a global optimal angle to maximize the interferometric signal. It would have to be studied case by case.

3.2.3 Minimum Threshold for Detection

As all asteroid orbits and close approaches are different, it is not possible to set a global optimal angle in which the asteroids would need to pass by to maximize the interferometric signal. It would

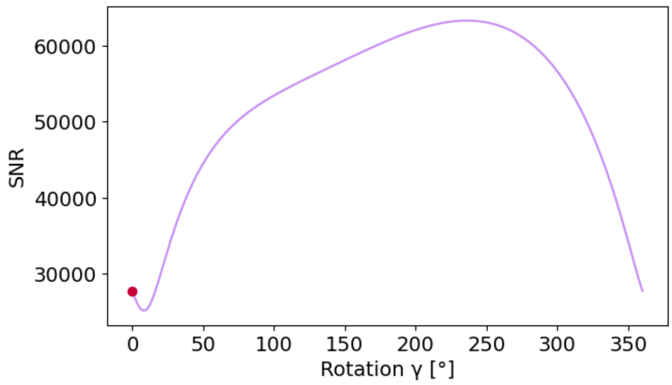

Figure 3.4: Variation of SNR for Asteroid 4179 Toutatis for close approach to S/C 2 due to different LISA Geometries. The red dot corresponds to the SNR at the current LISA geometry, i.e, a rotation of $\gamma = 0°$.

have to be studied case by case. Yet, with this first study it was intended to assess roughly if the asteroid is potentially detectable or not. Therefore, we studied for the currently observed population their variation of SNR for different γ. For each asteroid, the worst and best values of SNR were retained[3], giving us the worst and best signal for that asteroid. The percentage of detectable asteroids decreases to 0.26% corresponding to only 91 asteroids detected considering the worst interferometric signal for each asteroid. On the other hand, for a favourable LISA geometry, the percentage increases to 0.45% corresponding to 156 asteroids detected. In Figure 3.5 and 3.6, the mass, MOID and SNR diagrams for the unfavourable and favorable LISA geometries leading to the worst and best interferometric signals are shown, respectively.

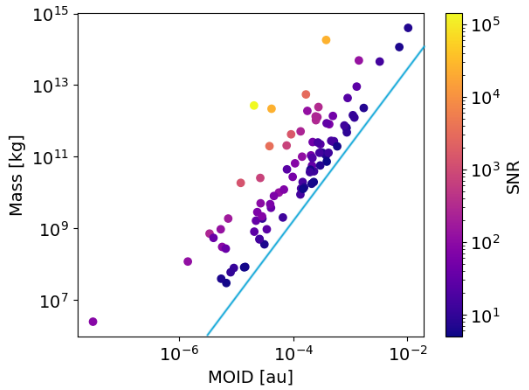

Figure 3.5: Minimum SNR, mass and MOID for asteroids with SNR≥ 5 from the observed population of NEAs. The blue line represents the minimum threshold of detection for the case in which the interferometric signal obtained for each asteroid is always the worst possible, corresponding to the individual γ giving the smallest SNR.

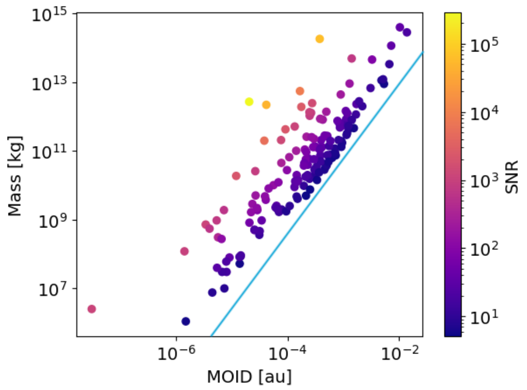

Figure 3.6: Maximum SNR, mass and MOID for asteroids with SNR≥ 5 from the observed population of NEAs. The blue line represents the minimum threshold of detection for the case in which the interferometric signal obtained for each asteroid is always the best possible, corresponding to the individual γ giving the greatest SNR.

In both plots, a blue line was inserted. It corresponds to the minimum threshold for detectability in terms of mass and MOID. For Figure 3.5, that line represents the minimum threshold for when the

[3]The values of minimum, maximum and current SNR for the LISA geometry at the close approach obtained for some of the observed asteroids are displayed in Appendix F

interferometric signal is always the worst possible. That would mean that any asteroid lying above is certaintly detectable. For Figure 3.6, the opposite scenario is shown. As the interferometric signal is always the best possible, we allow masses and MOIDs which in the original orbit would not allow detectability but, in the case that the close approach is favorable for the interferometry, the asteroid may be detected. This means that for this second diagram, the line allows a more optimistic scenario for the detection of asteroids. The difference between the two lines (from Figure 3.5 and Figure 3.6) is only a shift to the right.

Any of the two scenarios is valid and allows to draw the minimum threshold for detection for the mass and MOID variables. We opted by selecting the second diagram and a more permissive line. The minimum threshold drawn from Figure 3.6 corresponds to:

$$m\,[\mathrm{kg}] \geq 6.92 \times 10^{16}\ \mathrm{MOID}\,[\mathrm{au}]^{\,2.06} \tag{3.1}$$

According to the minimum threshold defined, the mass is related to almost the square of the distance. This behaviour is predicted by Newton's second law where there is a dependency of the inverse square of the distance. The slight deviation from two comes from the fact that the LISA spacecraft is not actually a point mass but an extended system composed of three spacecrafts. Through multiple decomposition of the system, it would be possible to see that the three spacecrafts add a little contribution to the exponent making it increase as seen in Equation 3.1. As a consequence of this study, the asteroids being tested in the following studies always obey this minimum threshold.

3.2.4 Discussion of Results

In this first study, three factors affecting the detectability were tested: the mass, the MOID and the LISA geometry. It is clear that the heavier the asteroid, the greater the signal will be and thus more likely to be detected. On the other hand, the closer it passes by, the stronger the signal will be and so again, the more likely to be detected. Nevertheless, the LISA geometry is a factor more unpredictable. Some close approaches happen in a favourable way for interferometry than others and, as every close approach is unique, it is not possible to draw a global conclusion. For some asteroids, the variation of SNR by the LISA geometry can be as great as a factor 10 between the $\mathrm{SNR}_{\mathrm{min}}$ and the $\mathrm{SNR}_{\mathrm{max}}$, while, for the most, it is around a factor 3.

Joining all these factors together, it is possible to predict if an asteroid is likely to be detected or not having a certain mass and a certain MOID and a minimum threshold can be drawn. The LISA geometry allows to shift curve to be a more optimistic or less permissive. As it is preferable to test all possible cases even if some do not lead to detection, the adopted threshold corresponds to the more permissive scenario, defined by Equation 3.1 calculated numerically.

3.3 Assessing the Probability of Detection of Asteroids

In this second study, the probability of detection for a certain asteroid or group of asteroids is computed. Two scenarios with different hypothesis are analysed:

1. *Non-Fixed Orbit*: scenario where the probability of detection is determined for an asteroid with defined semi-major axis, eccentricity and inclination and with a close approach at the MOID.

2. *Fixed Orbit*: scenario where the probability of detection is determined for an asteroid with a well defined orbit but a close approach not at the MOID, meaning other encounters generating the weaker signal are assessed.

In the first scenario, the idea is to assess the probability of detection for one unknown asteroid. This is relevant because the LISA mission might detect asteroids not yet observed, and this study allows to assess the probability of such phenomenon. On the other hand, the second scenario allows to study the detection of known asteroids which is also interesting since LISA can be used to perform complementary measurements, especially for the mass, on known asteroids.

To calculate the probability of detection for each scenario, several steps are followed. Initially, a probability of detection for an asteroid or group of asteroids with a certain mass is found for each scenario. Then, the probability density function for the mass is used to eliminate the dependency on the mass. To calculate the probability density function for the mass, the probability density function of the albedo, absolute magnitude and density are used. Due to the lack of measurements, the probability density function of the density is hypothesized using two models: one uniform distribution and a gamma distribution. These models are compared to assess the impact of the lack of information on the density of the asteroids in the final results. Finally, the found probability of detection, independent of the mass, is adjusted to match the LISA mission optimistic lifetime of 10 years. In this study, the fictitious population will be used for both scenarios.

3.3.1 Getting the Mass Probability Density Function

The probability density function (pdf) for the mass allows to determine the likelihood of an asteroid having a certain mass. The final probability of detection is independent of the mass of the asteroid, which means that the mass is integrated out with the help of its pdf. To assess it, we come back to the Equation 2.6 defining the mass. It is possible to rewrite it as a function of the density ρ, albedo p_v and absolute magnitude H:

$$m = f(\rho)\, g(p_v)\, h(H) = \left(\frac{\pi}{6}\rho\right)\left(a^3 p_v^{-\frac{3}{2}}\right)\left(e^{-\frac{3\ln 10}{5}H}\right). \tag{3.2}$$

where $a = 1329$ km. Assuming that the physical properties are statistically independent of each other, it is possible to derive the mass probability density function $p_m(m)$:

$$p_m(m) = \frac{20\,a^2}{3\pi \ln 10} \iint \frac{1}{\nu\, m} \left(\frac{t}{\nu}\right)^{\frac{2}{3}} p_\rho \left(\frac{6}{\pi} t\right) p_{p_v} \left(a^2 \left(\frac{t}{\nu}\right)^{\frac{2}{3}}\right) p_H \left(-\frac{5}{3} \frac{\ln m - \ln \nu}{\ln 10}\right) dt\, d\nu. \tag{3.3}$$

where $t = \frac{\pi}{6}\rho$ and $\nu = \left(a^3 p_v^{-\frac{3}{2}}\right)\left(e^{-\frac{3\ln 10}{5}H}\right)$, $p_\rho(\rho)$ is the probability density function for the density, $p_{p_v}(p_v)$ is the probability density function for the albedo and $p_H(H)$ is the probability density function for the absolute magnitude. The details of this derivation can be found in Appendix B. To use this expression, we need to derive the probability density functions for each physical property.

Probability Density Function for Albedo

A simplified model of the albedo distribution based on three categories for the albedo is presented in [39]. The pdf for the albedo, $p_{p_v}(p_v)$, is approximated by a piece-wise function with a flat probability for the first two categories and an exponentially decaying probability for the last category:

$$p_{p_v}(p_v) = C_N \begin{cases} c_1, & p_v < 0.1 \\ c_2, & 0.1 \le p_v < 0.3 \\ c_2 \left(\frac{1}{2.6}\right)^{\frac{p_v - 0.3}{0.1}}, & 0.1 \le p_v \le 1 \\ 0, & \text{otherwise} \end{cases} . \tag{3.4}$$

where c_i the constant probability for the category i and C_N is the constant of normalization so that the total probability for an albedo $p_v \in [0, 1]$ is one. Figure 3.7 illustrates this simplified probability density function.

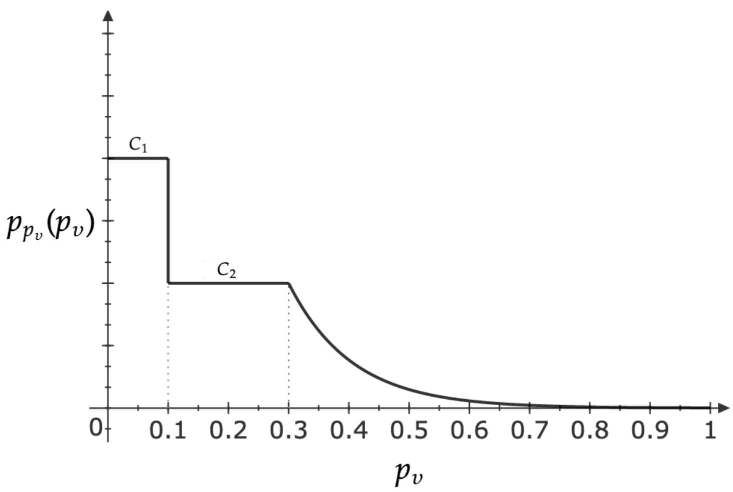

Figure 3.7: Simplified albedo probability density function for NEOPOP population

The NEOPOP model provides the quantities c_1 and c_2 for each asteroid generated, which allows to build the individual probability density function for the albedo of the asteroid.

Probability Density Function for Absolute Magnitude

The pdf for the absolute magnitude is defined by the model of the NEOPOP generator described in [59]. It is valid for all the asteroids of the fictitious population. The pdf for the absolute magnitude is presented in Figure 3.8.

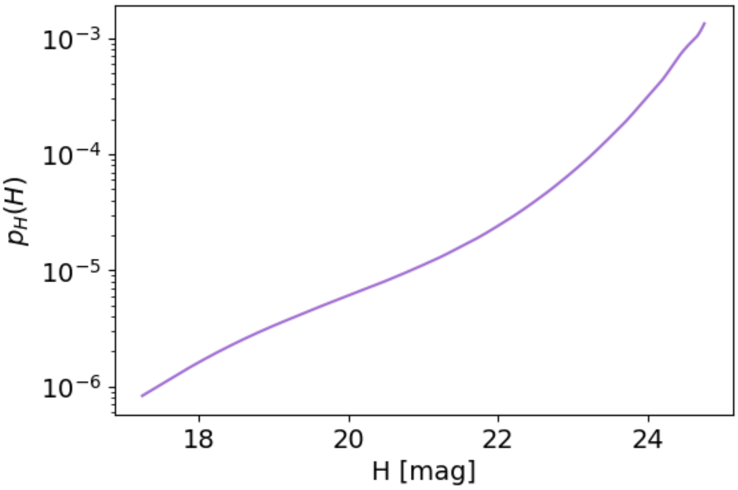

Figure 3.8: Probability density function of absolute magnitude for the asteroids of the fictitious population

Note that the absolute magnitude model is between $H \in [17, 25]$, as this is the expected interval of values for the asteroids orbiting around the Earth [59].

Probability Density Function for Density

We cannot generalize a probability density function for the density due to the lack of measurements. To overcome this, two pdf models were designed.

The first model is a simple model: an uniform distribution between the interval of densities $\rho \in [2000, 4000]\ \mathrm{kg/m^3}$. The chosen interval corresponds to the interval of measurements of the S taxonomy class, as it is the more likely class for NEA composition [30].

In second model, we assumed that the density could be given by a gamma function, so its pdf would be defined by the pdf of a gamma distribution $f(\rho,\, a)$ defined as:

$$f(\rho,\, a) = k\,\frac{\rho^{a-1}e^{-\rho}}{\Gamma(a)}. \tag{3.5}$$

where the density $\rho \geq 0\ \mathrm{kg/m^3}$, $a = 2$ the gamma constant and $k = 1000$ the multiplying factor to express the function in $\mathrm{kg/m^3}$. $\Gamma(a)$ corresponds to the gamma function.

This second model allows to assess the impact of a more complex pdf for the density, which is the case when we insert the contribution of the other than S taxonomy classes into the composition of the NEAs. Using two different models for the pdf allows to compare the effect of the pdf of the density in the results and the repercussions of not having an accurate model due to the lack of data. In Figures 3.9 and 3.10, the uniform and gamma pdf models are presented, respectively.

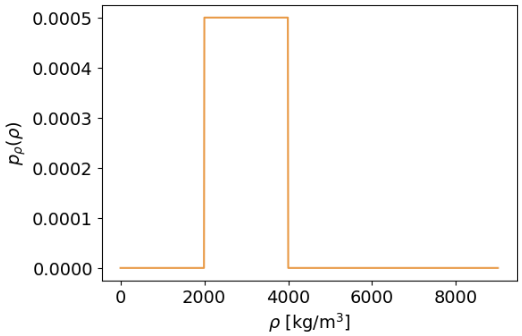

Figure 3.9: Uniform probability density function for the density of the fictitious population

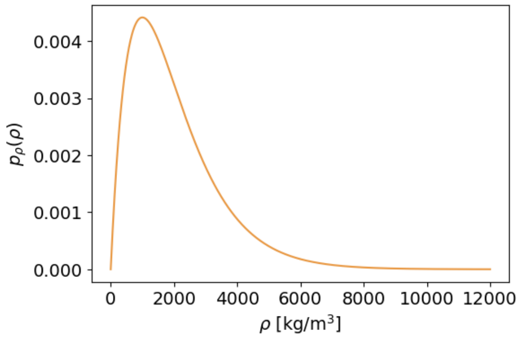

Figure 3.10: Gamma probability density function for the density of the fictitious population

Probability Density Function of Mass

There are two options to compute the pdf of the mass: either insert the pdfs of the physical properties in the pdf found analytically presented in Equation 3.3, or sample the individual pdfs of the physical properties, insert the found values into Equation 2.6 to calculate a value of mass and repeat this for thousands of samples. The second method was used as it simplifies the numerical computation. The resulting pdfs for the mass for Asteroid 4644 (for illustration purposes) using an uniform and gamma pdf for the density are shown in Figures 3.11 and 3.12, respectively. For Asteroid 4644, the pdf of the albedo was calculated using $c_1 = 0.14$, $c_2 = 0.59$ and $C_N = 5.17$. Note that the mass pdf needs to be recalculated for each asteroid due to their unique albedo pdf generated by the NEOPOP model.

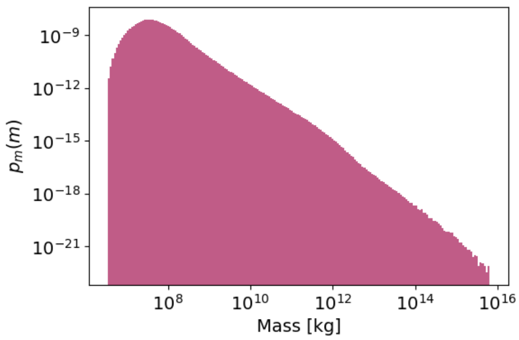

Figure 3.11: Mass probability density function for Asteroid 4644 using uniform probability density function for density

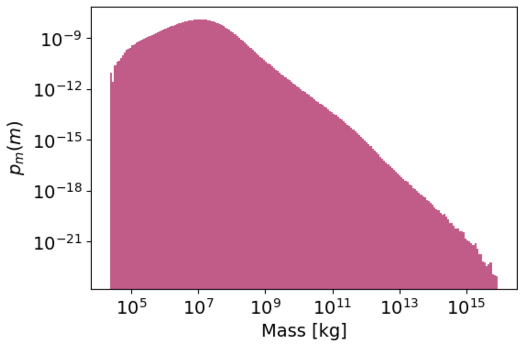

Figure 3.12: Mass probability density function for Asteroid 4644 using gamma probability density function for density

The two mass probability density functions are different. Since the uniform model only considers densities $\rho \in [2000, 4000]\ \mathrm{kg/m^3}$, the respective mass probability density function (Figure 3.11) allows masses between approximately $m \in [2\times10^6,\ 8\times10^{15}]\ \mathrm{kg}$ with a peak happening around $m = 10^8\ \mathrm{kg}$. The second model for the mass pdf allows a variation of the mass in a bigger range $m \in [8\times10^4,\ 6\times10^{15}]\ \mathrm{kg}$, with a lower upper range and a peak around $m = 10^7\ \mathrm{kg}$, due to the nature of gamma pdf for the density. It is expected that the second model will generate asteroids with lower masses, which decreases the strength of the signal and ending up decreasing the probability of detection. In fact, the results for this study showed a decrease in 20% for the probability of detection using the second model.

3.3.2 Computing the Probability of Detection

The probability of detection P_{det} of a certain asteroid or group of asteroids during the LISA lifetime of 10 years is calculated through:

$$P_{\text{det}} = \frac{10\,\text{yr}}{T_{\text{syn}}\,[\text{yr}]} \int_m p_{\text{det}}(m)\, p_m(m)\, dm. \tag{3.6}$$

where $p_m(m)$ is the probability density function of the mass, allowing to calculate an mass independent probability of detection and T_{syn} corresponds to the synodic period for the MOID. This integral allows to get rid of the mass dependency by integrating over the mass parameter space. The normalization using the synodic period is needed since the mass dependant probability of detection $p_{\text{det}}(m)$ is the probability of detection for a certain mass m in a parameter space during the synodic period. The synodic period T_{syn} for the asteroid and S/C is given by:

$$\frac{1}{T_{\text{syn}}} = \left| \frac{1}{T_{\text{NEA}}} - \frac{1}{T_{\text{S/C}}} \right|. \tag{3.7}$$

where T_{NEA} is the orbital period of the NEA and $T_{\text{S/C}}$ is the orbital period for the S/C. Out of curiosity, the distribution of T_{syn} for the synthetic population with S/C 2 are presented in Appendix F.

Mass Dependent Probability of Detection

The computation of the mass dependent probability of detection $p_{\text{det}}(m)$ follows the same principle for both scenarios. It is calculated from an area corresponding to the parameters allowing detection $A_{\text{det}}(m)$ for a given mass m, over the total area of the parameter space:

$$p_{\text{det}}(m) = \frac{A_{\text{det}}(m)}{(2\pi)^2}. \tag{3.8}$$

This is because we assume that the parameters are uniformly distributed in the parameter space. For the non-fixed orbit scenario, the parameters are the orbital elements $(\Omega,\, \omega)$ which are varied in the interval of $[0,\, 2\pi]\,\text{rad}$. For the fixed orbit, since we assess a close approach not happening at the MOID, the parameters correspond to the mean anomalies of the bodies in question $(M_{\text{NEA}},\, M_{\text{S/C}})$ which are also varied in the interval of $[0,\, 2\pi]\,\text{rad}$. So, the area of the 2D parameter space corresponds to $(2\pi)^2\,\text{rad}^2$.

In this work, the mass dependent probability $p_{\text{det}}(m)$ is calculated for different masses in the range of the $p_m(m)$, so that a curve can be constructed. This curve is, then, fitted so that the results can be extrapolated to allow the integration with the pdf of the mass $p_m(m)$ over the range of potential masses m and compute the mass independent probability of detection P_{det}. It is expected that the probability $p_{\text{det}}(m)$ can be fitted to something close to $p_{\text{det}}(m) \propto m^{0.4}$. This is because of the concept of Sphere of Influence (SoI), $r_{\text{SoI}} \propto m^{0.4}$, firstly introduced by Laplace in 1805 to investigate close encounters of comets with Jupyter and the Earth [63]. As the mass is increased, the signal gets stronger and the probability of detection increases. And since the impact of the change in mass is equivalent to a change in distance, we can expect the behavior of the SoI.

3.3.3 Assessing the Area of Detection

Non-Fixed Orbit Scenario

The NEOPOP software generates a random pair of (Ω, ω) for each asteroid. However, those values are important since they alter the 3D geometry of the orbit and the value of the MOID. Some pairs of (Ω, ω) can generate close approaches which allow the potential detection of the asteroid while others not. Nevertheless, finding out which combinations of (Ω, ω) correspond to such close approaches is a relatively hard 3D problem to solve analytically.

One way to test and obtain all valid combinations numerically is through an exhaustive search over the whole parameter range $[0, 2\pi]$ for both elements. Nevertheless, this is not a viable solution as it is quite computationally expensive due to its exponential complexity in space and time. As a consequence, a Local Search Algorithm (LSA) was designed to limit the search of the 2D grid on the promising pairs of (Ω, ω).

The LSA corresponds to a brute force search guided by a heuristic. The heuristic allows to find fast the relevant combinations of Ω and ω. It takes advantage from the fact that Ω and ω correspond to angles of rotation of the orbit in the 3D space. Once a pair (Ω, ω) with a small MOID is found, a small change to both elements $(\Omega + \Delta\Omega,\ \omega + \Delta\omega)$ will provide another small MOID. Thus, after a promising pair is found, the search is limited to the surrounding.

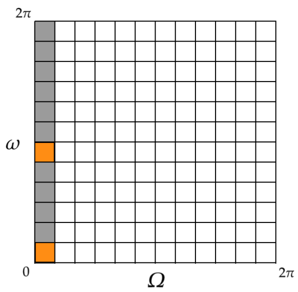

(a): Initial search state

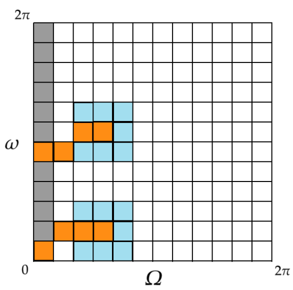

(b): Exploration at time t_1

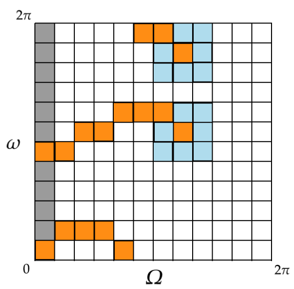

(c): Exploration at time t_2

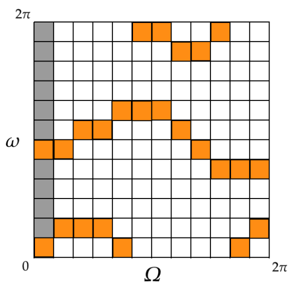

(d): Result of exploration

Figure 3.13: Illustration of search for promising (Ω, ω) using LSA. In (a), the initial probing mechanism is shown. All the positions tested in the first column are shown in grey, while the promising pairs of (Ω, ω) are shown in orange. As soon as these pairs are found, the search is guided by the heuristic which only evaluates the neighborhood, shown in blue for (b) and (c) at different times of exploration (with $t_1 < t_2$). In (d), when no more neighbors are to be tested, the search is concluded. Note that this algorithm acts in a mirror way, meaning that it recognises that $0 \equiv 2\pi$ for both angles. So if the promising pair is found in the upper limit, the search will continue in the lower limit.

Before applying the LSA, the space of potential solutions is discretized, i.e, a 2D grid where Ω and ω vary between $[0,\ 2\pi]$ is created. Then, the next is to find the initial promising pairs (Ω_0, ω_0). As it is not possible to predict these values without effort beforehand, the algorithm searches the first column of the grid, $(0, \omega_i)$ for $i = 1, 2, \ldots, N$, where N^2 is the number of pairs (Ω, ω) in the grid[4]. After having found these initial pairs, we start the search in their surroundings, i.e, the frontier. The search is stopped when there are no more points in the frontier to test. This is illustrated in Figure 3.13.

To select a promising candidate for detection, the results of the study in Chapter 3.2 to find a suitable candidate of detection are used. As the asteroid has an initial mass calculated using the H obtained from the model, a minimum MOID for the pairs of $(\Omega,\ \omega)$ can be calculated through Equation 3.1. If the MOID is lower or equal to the minimum MOID, then the pair $(\Omega,\ \omega)$ is considered valid.

The LSA generates diagrams as the ones shown in Figure 3.14 for Asteroid 4644. In the three diagrams, the mass of the asteroid was varied from its initial mass m_0 calculated using the mass equation model and the standard values for the density ρ and albedo p_v.

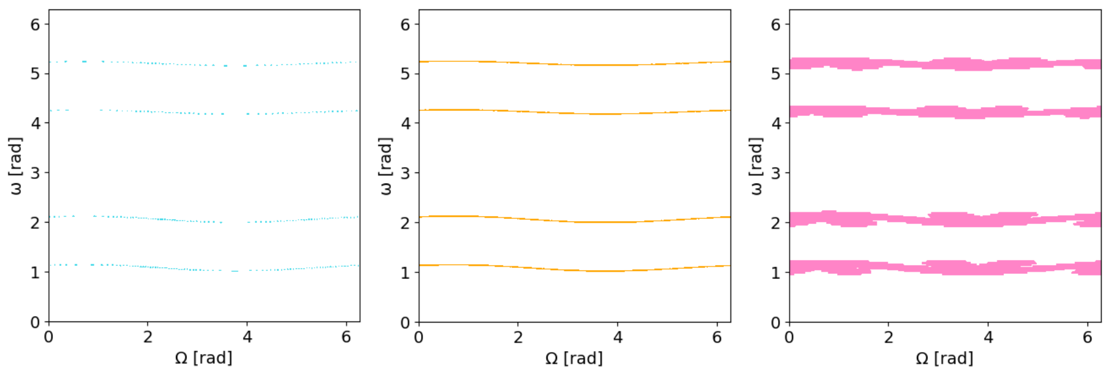

(a): $m = 0.001\, m_0$ (b): $m = m_0$ (c): $m = 1000\, m_0$

Figure 3.14: SNR as a function of (Ω, ω) for Asteroid 4644 of fictitious population. The lines represent the values of (Ω, ω) for $\mathrm{SNR} \geq 5$ not discriminated by color.

For Asteroid 4644, four strips are found in the three diagrams. In the first, the strips are more faded since the mass m is a factor 1000 compared to the initial mass m_0, calculated with the standard values and the generated H. On the other hand, for a mass m 1000 times bigger than the original mass, the strips become thicker. The irregularities in the thickening depend on the 3D spatial geometry of the orbit. We note that not all asteroids present four strips and that the patterns depend on the other orbital elements, so these diagrams, being unique, need to be simulated for all studied asteroids.

These $(\Omega,\ \omega)$ diagrams correspond to a variation in the phase space to construct a new asteroid's orbit with a new MOID. The area of detection is calculated from the area of the colored strips, where the SNR ≥ 5. By varying the mass m, it is possible to calculate a different area of detection $A_{\text{det}}(m)$ which helps drawing the curve $p_{\text{det}}(m)$ for the non-fixed orbit scenario.

[4]The grid is squared since there is no reason to be believe that one variable should be discretized more finely than the other.

Fixed Orbit Scenario

A close approach at the MOID is the ideal scenario, but not realistic. Additionally, the orbits of the asteroids are defined so, all orbital elements are fixed. As the MOID allows a detection with the best signal, we start simulating at the MOID and we assess a potential delay for the asteroid and the spacecraft, individually, by a variation of their mean anomaly M_{NEA} or $M_{\text{S/C}}$. Since there are two bodies in motion, there are four cases of delays/missed approach. These are illustrated in Figure 3.15.

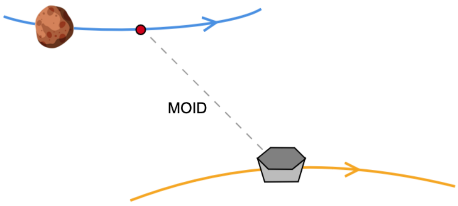

(a): S/C at MOID: asteroid is late

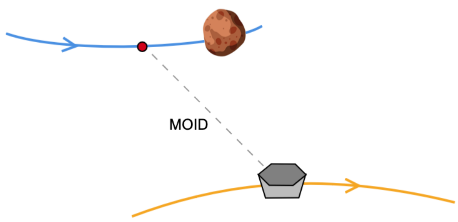

(b): S/C at MOID: asteroid is ahead

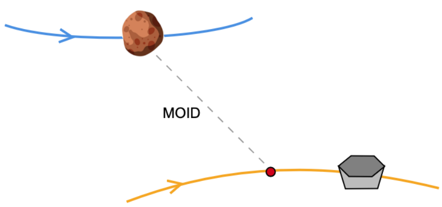

(c): Asteroid at MOID: S/C is late

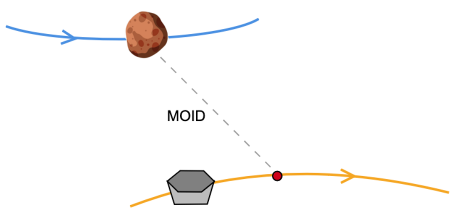

(d): Asteroid at MOID: S/C is ahead

Figure 3.15: Missed close approach scenarios. The red point represents the position of the MOID for the body in question in its orbit.

If we inspect more closely these four missed close approaches, we can see that Figure 3.14(c) is what will happen in the future of Figure 3.14(a) whenever the asteroid reaches the MOID. The same applies to 3.14(d) and 3.14(b). So effectively, it is enough to vary both variables, M_{NEA} and $M_{\text{S/C}}$, to produce all the scenarios.

These delays have an impact in the signal. Firstly because it won't be at the MOID, it will be at a new distance $d >$ MOID, meaning its intensity will decrease[5]. On the other hand, the shape of the signal will also change as the LISA geometry at the close approach will be different. An example of the signals and new shapes for a missed close approach when the asteroid is late is shown in Figure 3.16. As seen in Figure 3.16, the amplitude of the signal in case of a delay decreased. This is more pronounced in channel A. Additionally, the shape of the signal became different, especially for channels A and T. There was already a big decrease of SNR in the order of 20% for only a delay of $50\,\text{s}$ corresponding to a point a couple of thousand of kilometers away from the MOID.

[5]There is a small probability that the signal intensity may increase which is due to the LISA geometry. This means that very close to the MOID, if the distance is not sufficiently small and the LISA geometry is more favourable, we can have a case of a temporarily higher signal. Nevertheless, the trend is for the signal to decrease as we get away from the MOID.

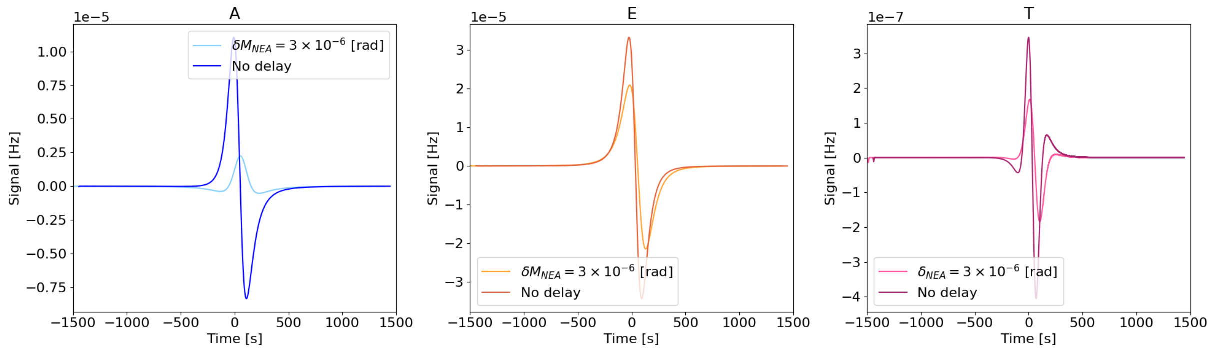

Figure 3.16: Signal in A, E and T channels when the asteroid is late of $\delta M_{\text{NEA}} = 3 \times 10^{-6}$ rad. This delay corresponds to approximately $50\,\text{s}$ which means a difference of already a couple of thousand of kilometers away from the MOID. The SNR decreased by 20% compared to the close approach at the MOID.

Since M varies linearly with time, a linear relationship can be found between M_{NEA} and $M_{\text{S/C}}$. This means that if both bodies are late or early enough by a certain amount, they still meet at the MOID. This is easily proven if we assess the time of passage at the MOID, t_{MOID}, for both bodies:

$$t_{\text{MOID}_{\text{NEA}}} = t_{\text{MOID}_{\text{S/C}}}. \tag{3.9}$$

The time of passage is easily rewritten as (for the asteroid as an example):

$$t_{\text{MOID}_{\text{NEA}}} = \frac{1}{n_{\text{NEA}}} \underbrace{\left(M_{\text{MOID}_{\text{NEA}}} - n_{\text{NEA}} T_0\right)}_{\Delta M_{\text{NEA}}}. \tag{3.10}$$

where $n_{\text{NEA}} = 2\pi / T_{\text{NEA}}$. Meaning that, it is possible to relate both mean anomalies:

$$\Delta M_{\text{NEA}} = \frac{T_{\text{S/C}}}{T_{\text{NEA}}} \Delta M_{\text{S/C}}. \tag{3.11}$$

From this relationship, we see that there are pairs of delays for each body $(\Delta M_{\text{NEA}}, \Delta M_{\text{S/C}})$ that allows them to meet at the MOID, and generate the strongest signal. The origin of the diagram where this line is designed corresponds to an arrival at the MOID where no delay happened.

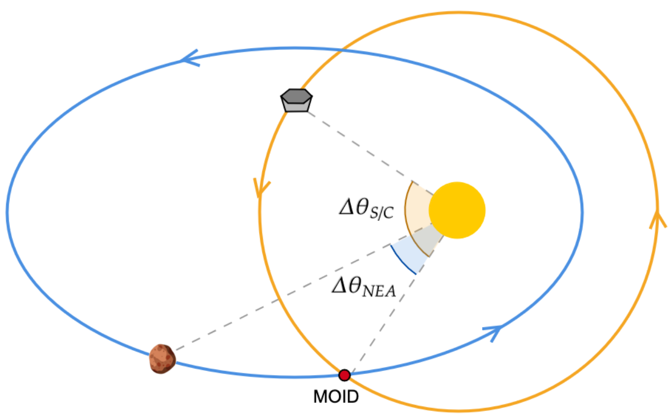

Figure 3.17: $\Delta\theta$ for both bodies to arrive at the MOID at the same time. These $\Delta\theta$ are calculated from the respective ΔM deduced from Equation 3.11. Note that for $\Delta M = 0$, $\Delta\theta = 0$ and both bodies are at the MOID.

The relationship works either when the body is late ($\delta M > 0$) or in advance ($\delta M < 0$). Nevertheless, a variation of M does not mean the bodies move linearly, though. To know the actual delay angle in their orbit, it is needed to recalculate the delay for the true anomaly, $\Delta\theta$, from the mean anomaly, ΔM to $\Delta\theta$, as shown in Figure 3.17.

In Figure 3.18, the SNR phase diagram for Asteroid 4644 with a mass $m = m_0$ for different values of $(\Delta M_{\text{NEA}}, \Delta M_{\text{S/C}})$ in the interval $[0,\, 0.001]$ rad is shown. The linear relationship for the $(\Delta M_{\text{NEA}}, \Delta M_{\text{S/C}})$ delay (Equation 3.11) appears naturally, showing the highest SNR. It is also possible to see the isolines for a delay causing a signal with a SNR $= 5$, in white.

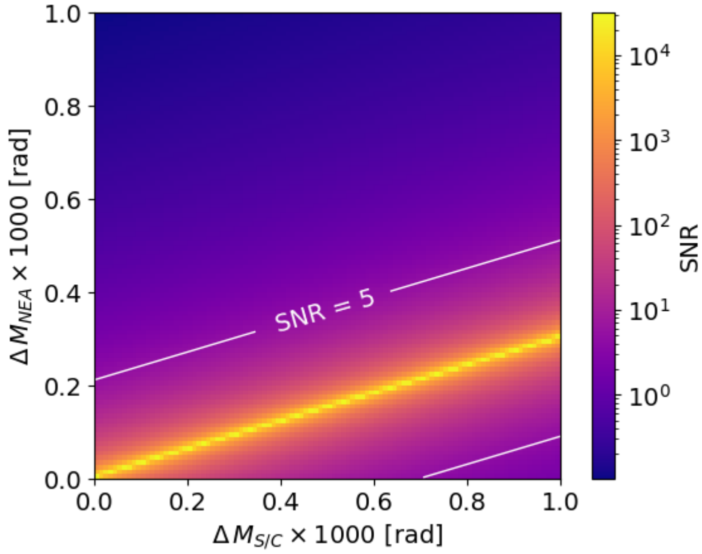

Figure 3.18: SNR as a function of the δM_{NEA} of the asteroid and $\delta M_{\text{S/C}}$ of the spacecraft for a mass $m = m_0$. The yellow line corresponds to the relationship illustrated by Equation 3.11 for the MOID, and in white the isolines at SNR $= 5$ are shown.

To detect the area of detectability $A_{\text{det}}(m)$, we draw the previous phase diagram for different masses for the variables $(\Delta M_{\text{NEA}}, \Delta M_{\text{S/C}})$ and we calculate the area of the strips[6] where SNR ≥ 5. The pair $(\delta M_{\text{NEA}}, \delta M_{\text{S/C}})$ is defined as the individual delays generating a signal with SNR $= 5$ when the other body is found at the MOID at the original time. This pair is used to calculate the area of detectability for a certain mass m for the fixed orbit scenario:

$$A_{\text{det}}(m) = 2 \times 2\pi \left(\delta M_{\text{NEA}}(m) + \frac{T_{\text{S/C}}}{T_{\text{NEA}}} \delta M_{\text{S/C}}(m) \right). \tag{3.12}$$

By varying the mass m, it is possible to calculate the curve $p_{\text{det}}(m)$. The effect of an increase in mass is relatively the same as in the non-fixed scenario. The heavier the asteroid, the wider the strips and the area of detectability increases.

[6] Note that actually there are actually two strips, so a factor 2 in the calculation of the area. This is due to the mirroring effect of the angle between 0 and 2π. To be able to visualize this, one needs to see that we can calculate the same area in the interval of $\delta M \in [0,\, 2\pi]$ rad instead, and that, in the end, there will be two parallelograms, one passing at the origin $(0,\, 0)$ and another one passing at the $(2\pi,\, 2\pi)$. An illustration of this idea is shown in Figure F.3 of Appendix F.

3.3.4 Example

Asteroid 4644 is an asteroid from the fictitious population having an original MOID $= 1.22 \times 10^{-5}$ au with S/C 2 with whom we generate an original close approach having a SNR $= 28240.29$. It was already used in some of the previous illustrations. Its orbital elements and physical properties are:

$$a = 2.23 \text{ au}, \quad e = 0.65, \quad i = 0.16 \text{ rad}, \quad \Omega = 0.0025 \text{ rad}, \quad \omega = 4.17 \text{ rad}, \quad m_0 = 1.34 \times 10^{11} \text{ kg}.$$

For this asteroid, we constructed both curves $p_{\text{det}}(m)$ for the non-fixed orbit (phase diagram of (Ω, ω)) and fixed orbit scenarios (phase diagram of $(\Delta M_{\text{NEA}}, \Delta M_{\text{S/C}})$) by calculating some points for different masses m (in blue) and fitting a line (in dotted grey). These are shown in Figures 3.19 and 3.20, respectively.

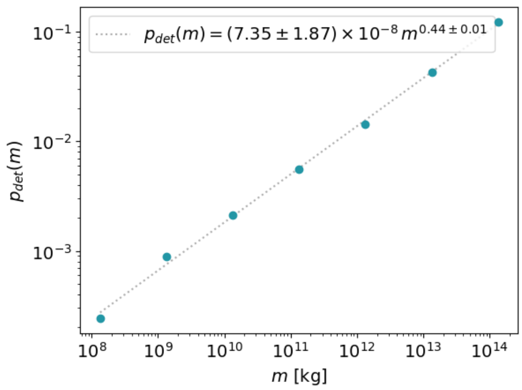

Figure 3.19: Probability of detection for the non-fixed orbit scenario as a function of mass for Asteroid 4644. Each point represents a value of $p_{\text{det}}(m)$ calculated for a certain mass m. A linear fit of the $p_{\text{det}}(m)$ curve is shown in dotted grey.

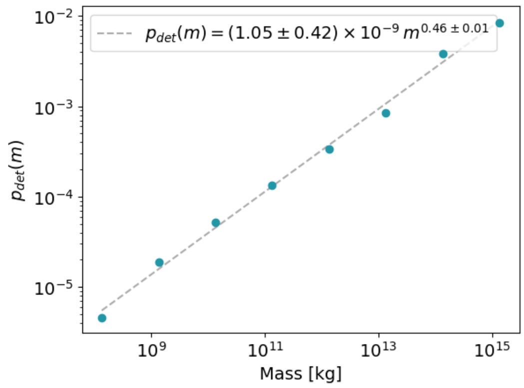

Figure 3.20: Probability of detection for the fixed orbit study as a function of mass for Asteroid 4644. Each point represents a value of $p_{\text{det}}(m)$ calculated for a certain mass m. A linear fit of the $p_{\text{det}}(m)$ curve is shown in dotted grey.

The linear fit allows us to infer the probability of detection for other masses not tested and save computational resources. From the observed plots, we see that the fit gives a dependency on the mass around of $p_{\text{det}}(m) \propto m^{0.4}$. It is actually slightly higher than the expected value since the close approach is slightly more complex than the model described by Laplace.

If we knew precisely the mass of the asteroid being observed with LISA, the probability of detection would correspond to a point in these curves. Nevertheless, the mass is most likely not known so it would be best to have a probability of detection independent of such property. That's why, we constructed the mass probability density function models (Figures 3.11 and 3.12). Using these models we integrate out the mass from the calculated mass dependant probability of detection curve.

For the non-fixed orbit scenario, the resulting mass independent probabilities of detection P_{det} for Asteroid 4644 using an uniform density pdf (model 1) and a gamma density pdf (model 2) to construct the mass pdf are:

$$P_{\text{det}}^{\text{non-fixed}}{}_{(1)} = 3.44 \times 10^{-3}, \quad P_{\text{det}}^{\text{non-fixed}}{}_{(2)} = 2.78 \times 10^{-3}$$

For the fixed orbit scenario, the resulting mass independent probabilities of detection P_{det} for Asteroid 4644 for the same models are:

$$P_{\text{det}}^{\text{fixed}}{}_{(1)} = 7.33 \times 10^{-5}, \quad P_{\text{det}}^{\text{fixed}}{}_{(2)} = 5.87 \times 10^{-5}$$

As expected, the probability of detection decreases for this second scenario because we fixed more parameters, even though we allowed flexibility on the close approach. Now, this probability means that we are able to detect with a certain likelihood this specific asteroid with fixed $(a, e, i, \Omega, \omega)$ during the lifetime of LISA but the detection does not need to happen in the MOID.

For both pairs of probabilities (both non-fixed and fixed orbit scenarios), the second mass pdf generates a 20% lower value compared to the first model. This is compatible with the analysis previously done for the mass pdf. The second model gives more probability to smaller masses for the asteroid, while the first has a longer tail in the higher masses.

3.3.5 Discussion of Results

Several more asteroids were tested for the two scenarios: non-fixed orbit scenario where a phase diagram of (Ω, ω) is used to calculate the mass dependant probability of detection, and a fixed orbit scenario where a phase diagram of $(\Delta M_{\text{NEA}}, \Delta M_{\text{S/C}})$ is used for the same effect. The results are displayed in Table 3.1.

			Non-Fixed Orbit		Fixed Orbit	
Name	SNR	T_{syn} [yr]	$P_{\text{det (1)}}$	$P_{\text{det (2)}}$	$P_{\text{det (1)}}$	$P_{\text{det (2)}}$
1836	51520.68	1.71	$3.06^{+3.72}_{-1.67} \times 10^{-3}$	$2.47^{+2.97}_{-1.34} \times 10^{-3}$	$9.40^{+5.52}_{-3.48} \times 10^{-5}$	$7.58^{+4.42}_{-2.79} \times 10^{-5}$
4644	28240.29	1.42	$3.44^{+1.78}_{-1.17} \times 10^{-3}$	$2.78^{+1.42}_{-0.94} \times 10^{-3}$	$7.33^{+6.16}_{-3.34} \times 10^{-5}$	$5.88^{+4.88}_{-2.66} \times 10^{-5}$
6135	235.80	3.27	$1.51^{+1.13}_{-0.64} \times 10^{-3}$	$1.21^{+0.90}_{-0.52} \times 10^{-3}$	$7.31^{+33.74}_{-5.98} \times 10^{-5}$	$5.78^{+26.30}_{-4.72} \times 10^{-5}$
8775	62177.07	2.03	$1.27^{+0.08}_{-0.07} \times 10^{-2}$	$1.03^{+0.06}_{-0.06} \times 10^{-2}$	$1.07^{+1.00}_{-0.52} \times 10^{-4}$	$8.68^{+8.00}_{-4.15} \times 10^{-5}$
11545	3470.39	1.30	$1.45^{+0.40}_{-0.32} \times 10^{-3}$	$1.18^{+0.32}_{-0.25} \times 10^{-3}$	$9.40^{+3.26}_{-2.45} \times 10^{-5}$	$7.98^{+2.62}_{-1.97} \times 10^{-5}$
13323	8801.66	8.77	$5.33^{+4.35}_{-2.39} \times 10^{-4}$	$4.29^{+3.46}_{-1.91} \times 10^{-4}$	$4.18^{+3.59}_{-1.93} \times 10^{-5}$	$3.36^{+2.86}_{-1.54} \times 10^{-5}$
14414	120.68	1.35	$7.73^{+6.42}_{-3.50} \times 10^{-3}$	$6.22^{+5.11}_{-2.80} \times 10^{-3}$	$6.11^{+30.54}_{-5.07} \times 10^{-5}$	$4.81^{+23.65}_{-3.98} \times 10^{-5}$
19021	11.94	185.09	$2.34^{+1.02}_{-0.71} \times 10^{-5}$	$1.91^{+0.82}_{-0.57} \times 10^{-5}$	$6.94^{+53.75}_{-6.12} \times 10^{-7}$	$5.35^{+40.81}_{-4.71} \times 10^{-7}$

Table 3.1: Results for Probability of detection study for the non-fixed and fixed orbits cases for 8 asteroids of the fictitious population. (1) uses the uniform distribution (Figure 3.9) for the probability density distribution of ρ. (2) uses the gamma function (Figure 3.10) for the probability density distribution of ρ. The MOID and the synodic periods T_{syn} were calculated with S/C 2. More results can be found in Appendix F.

The two models for the density pdf used to generate the mass pdf were studied: model (1) considering a uniform distribution between $\rho \in [2000, 4000]\ \mathrm{kg/m^3}$, and model (2) considering a gamma distribution with $a = 2$ and $k = 1000$.

As seen, the probability of detection for the fixed orbit approach is always smaller than the non-fixed orbit one. It makes sense as the second study has more constraints than the first one. Furthermore, the probability of detection using the gamma probability density function for the density keeps its trend of being 20% lower compared to the uniform probability density function for the density. Moreover, the smaller the SNR, the less likely the detection of the asteroid, and thus, its probability of detection decreases.

Asteroid 8775 has the greatest probability of detection in both cases being also the one with the lowest uncertainties. We can also see that there are uncertainties on the probability of detection, and that these are not symmetrical. We tend to underestimate the probability when we use the fitted curve for $p_{\text{det}}(m)$. The errors are usually on the order of 50% being able to up to 100%. Although in terms of relative error it seems a lot, the probabilities found are very small, thus a small variation causes great relative errors. While looking at it from the absolute point of view, the errors make the probability still stay in the same order of magnitude and are not that big.

Another interesting result from both these studies is that from the fitting done to the mass dependent probability of detection $p_{\text{det}}(m)$ for both studies, from all the data collected, we can see that it is proportional to the mass as:

$$p_{\text{det}}(m) \propto m^{0.45 \pm 0.03}. \tag{3.13}$$

This alludes to the concept of sphere of influence. In our case, it becomes a sphere of detectability around the MOID and the sphere decreases radius it the mass of the asteroid is smaller, meaning that it needs a closer approach to be detected. Again, due to the complexity of the LISA system and that it is not a point mass, the exponent doesn't match perfectly what is defined in Laplace's equation. Being above 0.4 is consistent with the contributions of the other spacecrafts to the measurement done and to the detection of the asteroid.

Some of the asteroids, we can see that for the fixed orbit scenario, we underestimate the probability of detection sometimes by a significant amount. The study is under the assumption that there is only a single close approach to a specific spacecraft but this may not be the reality. As soon as its region of influence becomes considerable, it can generate smaller signals on the other spacecraft which allow to collect much more information and increase its probability of detection. And, when the delay is sufficiently important, it may end up placing the asteroid in a favourable position for a close approach with another spacecraft. This translates by a faulty fit for the curve $p_{\text{det}}(m)$ which then translates to a bigger uncertainty for the positive error. A more complete explanation of this phenomenon which affects several asteroids in a certain scale can be consulted in Appendix D: Deviation from the Sphere of Influence.

These results allow to see we can predict the order of magnitude of the probability of detection within a certain uncertainty interval. Moreover, the non-fixed and fixed orbit scenarios have different assumptions but they are not mutually exclusive, so it is possible and envisioned to join these together.

If we end up calculating new SNR phase diagrams taking into account (Ω, ω) and the ΔM delays, it is possible to calculate a $p_{det}(m)$ curve which encompasses both effects. So, we can calculate a probability of detection for an asteroid defined by $(a,\, e,\, i)$ but not assuming a close approach at the MOID. Additionally, if we want to calculate a probability of detection for the fictitious population and not just a group of asteroids with well defined $(a,\, e,\, i)$, we can also integrate out these variables using the probability density functions of $(a,\, e,\, i)$ of the NEOPOP model shown in Figure 3.1. But for that we would need a lot of computational power and, right now, we are limited by computational time[7], and we can only envision it as future work.

[7] For a single asteroid, the average computational time needed for the first study is around one day and for the second study around two hours using a MacBook Pro with a chip M1 Max and a memory of 32GB.

3.4 Assessing the Uncertainty in Measurements

In this final study, we assess the uncertainty in the asteroid orbital elements and physical properties assuming a measurement is done with the LISA mission.

The determination of the uncertainty in signals is valuable as it is often employed as a proxy for the amount of information that can be collected by the detectors. However, to predict the parameter-estimation performance of future observations is a complex matter even if there are theoretical descriptions of the expected signals and realistic descriptions of the noise and of the detectors. There are a few analytical techniques that can be applied to make such prediction. In the source-modeling and gravitational waves' community, the analytical tool of choice has been the Fisher Information theory [64]. The Fisher-matrix formalism allows to calculate the uncertainty in the parameters making some assumptions on the noise probability and measurements in a singularly economical way due to its compactness and accessibility. Therefore, we adopted this technique.

In the first part of this study, the Fisher Matrix $\boldsymbol{F}$ is derived for the parameters $\boldsymbol{\theta}$ to be extracted from the signal after detection. Then, from the Fisher Matrix, the Covariance Matrix $\boldsymbol{C}$ is deduced, which provides the standard deviation $\boldsymbol{\sigma}$ for the measured parameters. Finally, the Correlation Matrix $\boldsymbol{X}$ is computed so that the parameters' dependency for the signal and the relations between the different uncertainties is known.

Since the LISA mission captures signal in three different TDI channels, their individual information can be joined to compute a final Fisher Matrix and subsequent results gathering all the information of the full system.

3.4.1 Fisher Information

The Fisher Information concept allows to quantify the amount of information an observation carries about a set of parameters. In order to explain it, we will base and adapt the work in [65, 66]. We start by defining the output of the detector, i.e, the data stream $g(t, \boldsymbol{\theta})$ as:

$$g(t, \boldsymbol{\theta}) = \begin{cases} n(t), & \text{if no signal is present;} \\ n(t) + x(t, \boldsymbol{\theta}), & \text{if signal } x(t, \boldsymbol{\theta}) \text{ is present.} \end{cases} \tag{3.14}$$

where $\boldsymbol{\theta}$ is a vector containing the unknown parameters we pretend to extract, $n(t)$ the noise on the data stream and $x(t, \boldsymbol{\theta})$ is the potential signal characterized by the parameters $\boldsymbol{\theta}$. The data stream corresponds to the time-series data collected in the detectors, with or without containing a signal.

For an NEA, the parameters to be extracted from a LISA measurement correspond to the orbital elements and the mass, so $\boldsymbol{\theta}$ can be defined as the vector:

$$\boldsymbol{\theta} = \begin{bmatrix} a & e & i & \Omega & \omega & m \end{bmatrix}. \tag{3.15}$$

where the semi-major axis a is in au, the angles i, Ω and ω in rad and the mass m in kg.

We intend to define the error bars on the detection of the signal $x(t, \boldsymbol{\theta})$ given that we collected the datastream $g(t, \boldsymbol{\theta})$ and that we have a model $m(t, \boldsymbol{\theta})$ that explains the data, i.e, the model of the signal. In other words, we want to define the covariance of the model $m(t, \boldsymbol{\theta})$. For that, Bayes' Theorem is used. We can define the probability $P(x \,|\, g)$ of presence of the signal $x(t, \boldsymbol{\theta})$ given the observed datastream $g(t, \boldsymbol{\theta})$:

$$\underbrace{P(x \,|\, g)}_{\text{posterior}} = \frac{\overbrace{P(g \,|\, x)}^{\text{likelihood}} \; \overbrace{P(x)}^{\text{prior}}}{\underbrace{P(g)}_{\text{evidence}}}. \tag{3.16}$$

where $P(g \,|\, x)$ is the probability of observing $g(t, \boldsymbol{\theta})$ assuming the signal $x(t, \boldsymbol{\theta})$ is present, $P(x)$ is the probability that the signal $x(t, \boldsymbol{\theta})$ defined by the parameters $\boldsymbol{\theta}$ is present, and $P(g)$ is the probability that the datastream $g(t, \boldsymbol{\theta})$ is observed.

As we know nothing about the posterior probability $P(x \,|\, g)$ itself, we use the previous relationship to relate it to the likelihood probability $P(g \,|\, x)$ that we can deduce while making some informed assumptions. As the prior probability $P(x)$ is not known either, we adopt an uninformative prior based on the principle of indifference which states that in the absence of any relevant evidence, we should distribute the probability equally among all the possible outcomes under consideration. On the other hand, the evidence probability $P(g)$ is typically used either as a normalization probability or a comparator between different models for the signal. It allows us to assess how well the model predicts the signal.

Note that all the results presented below correspond to the matrix form of the Fisher Information due to the nature of the parameters $\boldsymbol{\theta}$ to be studied.

Likelihood

From Equation 3.16, it can be seen that the posterior probability $P(x \,|\, g)$ is proportional to the likelihood probability. This means that by analysing the error bars defined with the likelihood, we end up analysing the error bars on the model that is defined by the posterior probability.

To be able to determine the likelihood, we can perform an experiment where we measure N data points (g_k, t_k) where $k = 1, 2, ..., N$ in a case where the datastream contains the signal. On top of it, we assume we have the model $m(t, \boldsymbol{\theta})$ that describes such signal. The noise $n(t)$ on the data is assumed white Gaussian noise, $\mathcal{N}(0,\, \sigma^2)$, with a variance σ^2. In this case, the probability $P(g_k \,|\, x_k)$ of observing one measurement of the datastream g_k given that it contains the signal x_k is:

$$P(g_k \,|\, x_k) = \frac{1}{\sqrt{2\pi\sigma_k^2}} \, e^{-\frac{(g_k - m(t_k, \boldsymbol{\theta}))^2}{2\sigma_k^2}}. \tag{3.17}$$

The likelihood $\mathcal{L}(g \,|\, x,\, \boldsymbol{\theta})$ is the probability of doing independent measurements of all g_k, given by:

$$\begin{aligned} \mathcal{L}(g \,|\, x;\, \boldsymbol{\theta}) &= \prod_{k=1}^{N} P(g_k \,|\, x_k) \\ &\propto e^{-\sum_{k=1}^{N} \frac{(g_k - m(t_k, \boldsymbol{\theta}))^2}{2\sigma_k^2}}. \end{aligned} \tag{3.18}$$

In practice, it is often convenient to work with the natural logarithm of the Likelihood, i.e, the Log-Likelihood $\ell(g \,|\, x;\, \boldsymbol{\theta})$:

$$\begin{aligned}\ell(g \,|\, x;\, \boldsymbol{\theta}) &= \log \mathcal{L}(g \,|\, x;\, \boldsymbol{\theta}) \\ &= -\frac{1}{2} \sum_{k=1}^{N} \frac{(g_k - m(t_k, \boldsymbol{\theta}))^2}{\sigma_k^2} + q.\end{aligned} \tag{3.19}$$

where q is a constant related to the product of the normalization of the measurement probabilities.

In Statistics, we can perform a estimation of the parameters $\boldsymbol{\theta}$ of an assumed model given the observed datastream using the Maximum Likelihood Estimation method. It relies on maximizing the likelihood function (or log-likelihood function as it is also a monotonic function with the same maximum) where the observed data is the most probable under the assumed statistical model.

In our case, the maximization of the log likelihood function leads to the formalism of the Least Squares Estimation method, meaning, we intend to estimate the parameters $\boldsymbol{\theta}$ that allow to minimize the residuals or error between the model $m(t, \boldsymbol{\theta})$ and the signal $x(t, \boldsymbol{\theta})$ in the datastream $g(t, \boldsymbol{\theta})$. The constant c becomes irrelevant in this minimization as it does not change the result of the estimation method.

$$\max_{\boldsymbol{\theta}} \ell(g \,|\, x;\, \boldsymbol{\theta}) \equiv \min_{\boldsymbol{\theta}} \sum_{k=1}^{N} \frac{(g_k - m(t_k, \boldsymbol{\theta}))^2}{\sigma_k^2}. \tag{3.20}$$

We define $\boldsymbol{\theta}_{\text{min}}$ as the parameters that minimize the Least Squares problem.

$$\boldsymbol{\theta}_{\text{min}} = \underset{\boldsymbol{\theta}}{\operatorname{argmin}} \sum_{k=1}^{N} \frac{(g_k - m(t_k, \boldsymbol{\theta}))^2}{\sigma_k^2} = \mathrm{LSQ}(\boldsymbol{\theta}). \tag{3.21}$$

It is possible to rewrite the Least Squares problem using a Taylor Expansion.

$$\mathrm{LSQ}(\boldsymbol{\theta}) = \mathrm{LSQ}(\boldsymbol{\theta}_{\text{min}}) + (\boldsymbol{\theta}_{\text{min}} - \boldsymbol{\theta}) \underbrace{\partial_{\boldsymbol{\theta}} \mathrm{LSQ}(\boldsymbol{\theta})|_{\boldsymbol{\theta}_{\text{min}}}}_{=0} + \frac{1}{2} (\boldsymbol{\theta}_{\text{min}} - \boldsymbol{\theta})^2 \; \partial^2_{\boldsymbol{\theta}} \mathrm{LSQ}(\boldsymbol{\theta})|_{\boldsymbol{\theta}_{\text{min}}} + \ldots \,. \tag{3.22}$$

The first term of the Taylor Expansion corresponds to the value of the Least Square problem at the parameters $\boldsymbol{\theta}_{\text{min}}$ minimizing it. That means if $\boldsymbol{\theta}_{\text{min}}$ is chosen carefully, $\mathrm{LSQ}(\boldsymbol{\theta}_{\text{min}})$ should be close to or tend to 0. The second term is 0 by the definition of minimization and derivative. On the other hand, higher orders than second order are just residuals and also average out. Thus, the only relevant term for this expansion is the second derivative. This means that the likelihood can be approximated to the second order derivative of the Taylor Expansion around $\boldsymbol{\theta}_{\text{min}}$:

$$\mathcal{L}(g \,|\, x;\, \boldsymbol{\theta}) \propto e^{-\frac{1}{4} (\boldsymbol{\theta}_{\text{min}} - \boldsymbol{\theta})^2 \; \partial^2_{\boldsymbol{\theta}} \mathrm{LSQ}(\boldsymbol{\theta})|_{\boldsymbol{\theta}_{\text{min}}}}. \tag{3.23}$$

This means that close to the maximum, the likelihood behaves as a Gaussian with a variance σ^2 of:

$$\frac{1}{\sigma^2} = \frac{1}{2} \partial^2_{\boldsymbol{\theta}} \mathrm{LSQ}(\boldsymbol{\theta})|_{\boldsymbol{\theta}_{\text{min}}}. \tag{3.24}$$

By applying a second derivative on the LSQ problem defined in Equation 3.21, we can evaluate it to:

$$\begin{aligned}\partial^2_{\boldsymbol{\theta}} \, \mathrm{LSQ}(\boldsymbol{\theta}) &= \sum_{k=1}^{N} \partial^2_{\boldsymbol{\theta}} \, \frac{(g_k - m(t_k, \boldsymbol{\theta}))^2}{\sigma_k^2} \\ &= 2 \sum_{k=1}^{N} \frac{(m(t_k, \boldsymbol{\theta}) - g_k) \, \partial^2_{\boldsymbol{\theta}} \, m(t_k, \boldsymbol{\theta}) + (\partial_{\boldsymbol{\theta}} \, m(t_k, \boldsymbol{\theta}))^2}{\sigma_k^2}\end{aligned} \tag{3.25}$$

At $\boldsymbol{\theta} = \boldsymbol{\theta}_{\text{min}}$, the first term $(m(t_k, \boldsymbol{\theta}) - g_k) \, \partial^2_{\boldsymbol{\theta}} \, m(t_k, \boldsymbol{\theta})$ corresponds to the residuals of the fit between the model $m(t_k, \boldsymbol{\theta})$ and the signal $x(t_k, \boldsymbol{\theta})$ present in the datastream g_k. So assuming, an accurate model of the signal, this term averages out. This means that:

$$\partial^2_{\boldsymbol{\theta}} \mathrm{LSQ}(\boldsymbol{\theta})|_{\boldsymbol{\theta}_{\text{min}}} = 2 \sum_{k=1}^{N} \frac{(\partial_{\boldsymbol{\theta}} \, m(t_k, \boldsymbol{\theta})|_{\boldsymbol{\theta}_{\text{min}}})^2}{\sigma_k^2} \tag{3.26}$$

Now, the previous equation can be rewritten in a more matrix friendly and generalized format:

$$\frac{1}{2} \partial_{\theta_i} \partial_{\theta_j} \mathrm{LSQ}(\boldsymbol{\theta})|_{\boldsymbol{\theta}_{\text{min}}} = \sum_{k=1}^{N} = \frac{\partial_{\theta_i} m(t_k, \boldsymbol{\theta})|_{\boldsymbol{\theta}_{\text{min}}} \, \partial_{\theta_j} m(t_k, \boldsymbol{\theta})|_{\boldsymbol{\theta}_{\text{min}}}}{\sigma_k^2} = C_{ij}^{-1} \tag{3.27}$$

where $F_{ij} = C_{ij}^{-1}$ corresponds to the Fisher Matrix element i, j, and C_{ij} the Covariance Matrix element i, j of the model.

The derivatives of the model and the covariances are inversely proportional. This means that if the model depends strongly on the parameters, the covariances will be small and thus, the signal can be determined quite well. On the other hand, if the model doesn't depend strongly on the parameters, their determination can become difficult due to the large covariance. This alludes to the need of a somewhat precise model when detecting NEAs in the LISA datastream.

Through Parseval's Theorem (Equation 2.17), one can easily calculate the PSD_n of the noise. Nevertheless, in the frequency domain, the variance of the noise is nothing less than the variance than the average power of the noise, i.e, the integral of the PSD over the frequency spectrum. Consequently, the variance of the noise σ^2 can be rewritten as:

$$\sigma^2 = \int_{-\infty}^{\infty} \mathrm{PSD}_n(f) \, df. \tag{3.28}$$

We considered so far the model $m(t, \boldsymbol{\theta})$ in the time domain, but we can also translate it to the frequency domain. With the help of the definition of Fourier Transform (Equation 2.16), we end up with a frequency domain model, $\tilde{m}(f, \boldsymbol{\theta})$. Now, using the definition of inner product between two signals in the frequency domain and the previous definition of variance, it can be shown that we can rewrite the Fisher Matrix element F_{ij} as:

$$F_{ij} = \int_{-\infty}^{\infty} \frac{(\partial_{\theta_i}\tilde{m}(f,\boldsymbol{\theta}))\,(\partial_{\theta_j}\tilde{m}(f,\boldsymbol{\theta}))^* + (\partial_{\theta_i}\tilde{m}(f,\boldsymbol{\theta}))^*\,(\partial_{\theta_j}\tilde{m}(f,\boldsymbol{\theta}))}{\mathrm{PSD}_n(f)}\,df = C_{ij}^{-1}. \tag{3.29}$$

From its definition, it can be seen that the Fisher Matrix $\boldsymbol{F} = \boldsymbol{C}^{-1}$ is a symmetric matrix, but also invertible so that it is possible to extract the covariances for the parameters. The relevant part of the Covariance Matrix $\boldsymbol{C}$ is its diagonal, which contains the variance for the parameters $\boldsymbol{\theta}$. We can define the diagonal matrix $\boldsymbol{D}$ containing the standard deviations of the measured parameters $\boldsymbol{\theta}$ as:

$$\boldsymbol{D} = \begin{bmatrix} \sqrt{C_{\theta_1}} & 0 & 0 \\ 0 & \ddots & 0 \\ 0 & 0 & \sqrt{C_{\theta_M}} \end{bmatrix} \tag{3.30}$$

where $\boldsymbol{\theta}$ contains M unknown parameters. Finally, we can calculate the Correlation Matrix $\boldsymbol{X}$ using this diagonal matrix $\boldsymbol{D}$ for scaling purposes.

$$\boldsymbol{X} = \boldsymbol{D}^{-1}\boldsymbol{C}\boldsymbol{D}^{-1} \tag{3.31}$$

The Correlation Matrix allows to measure the intensity and relation between the different parameters. It allow us to determine how correlated are the variables between them. And from it, we can assess the estimation of the parameters itself, meaning assess their stability or potential considerable errors in their measurement.

3.4.2 Example

Asteroid 1836 is an asteroid from the fictitious population having a MOID $= 4.61 \times 10^{-5}$ au with S/C 2 with whom we generate a close approach having a SNR $= 51520.68$. Its orbital elements and physical properties are:

$$a = 1.79 \text{ au}, \quad e = 0.53, \quad i = 0.15 \text{ rad}, \quad \Omega = 1.14 \text{ rad}, \quad \omega = 2.09 \text{ rad}, \quad m_0 = 2.84 \times 10^{12} \text{ kg}.$$

The objective of this study lies on calculating both the Covariance and Correlation Matrix to assess how well can we determine the parameters $\boldsymbol{\theta} = [a,\, e,\, i,\, \Omega,\, \omega,\, m]$. According to Equation 2.15, the PSD of the noise is defined as $\mathrm{PSD}_n(f) = S_n(f)$. The model of the signal $m(t, \boldsymbol{\theta})$ is exactly the signal in the detectors after applying the TDI technique on our simulation (see *4. Apply TDI Technique* in Page 25). Since it is computationally expensive to calculate the derivative of the model $m(t, \boldsymbol{\theta})$ for each pair of $(\theta_i,\, \theta_j)$, the definition of derivative through its limit is used considering a variation of the parameters $\Delta\boldsymbol{\theta}$:

$$\Delta\boldsymbol{\theta} = \begin{bmatrix} 10^{-6}a & 10^{-6}e & 10^{-4}i & 10^{-6}\Omega & 10^{-6}\omega & 10^{-2}\,m_0 \end{bmatrix}.$$

The chosen values allow to calculate a sufficiently accurate derivative without compromising the numerical precision of the computations. For illustration purposes, the signals in the TDI channels for the current asteroid parameters $\boldsymbol{\theta}$ with the impact of individual variations $\Delta\boldsymbol{\theta}$ on each parameter are illustrated in Figure 3.21.

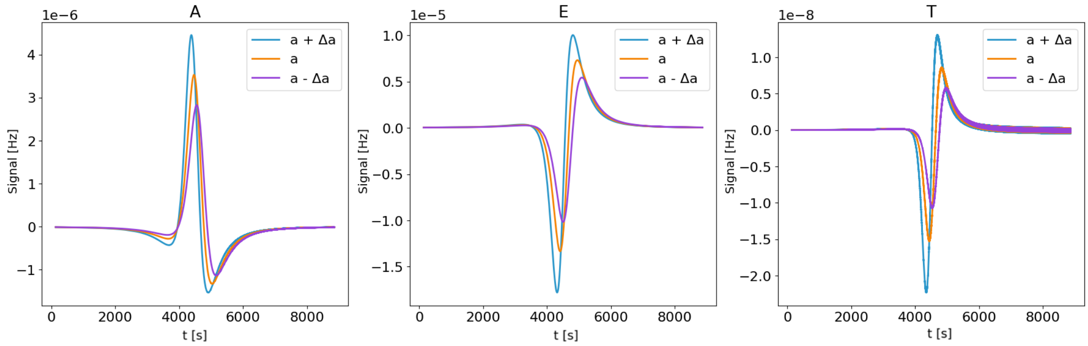

(a): TDI Signal when varying the semi-major axis a by $\Delta\, a = 10^{-5}\, a$

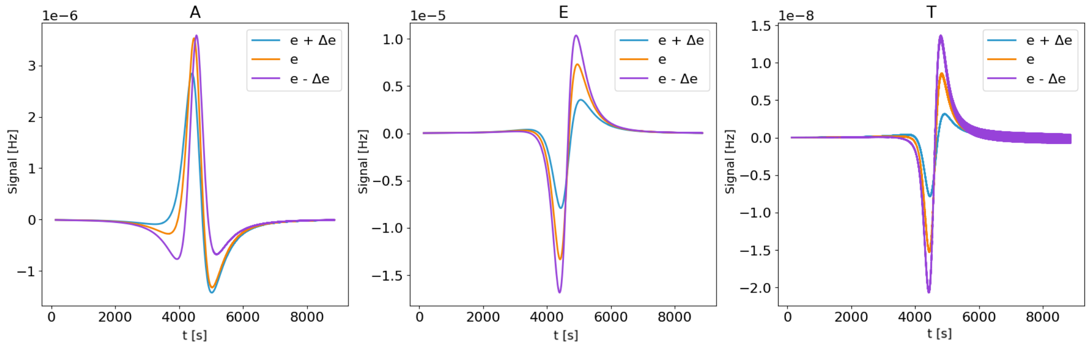

(b): TDI Signal when varying the eccentricity e by $\Delta\, e = 10^{-5}\, e$

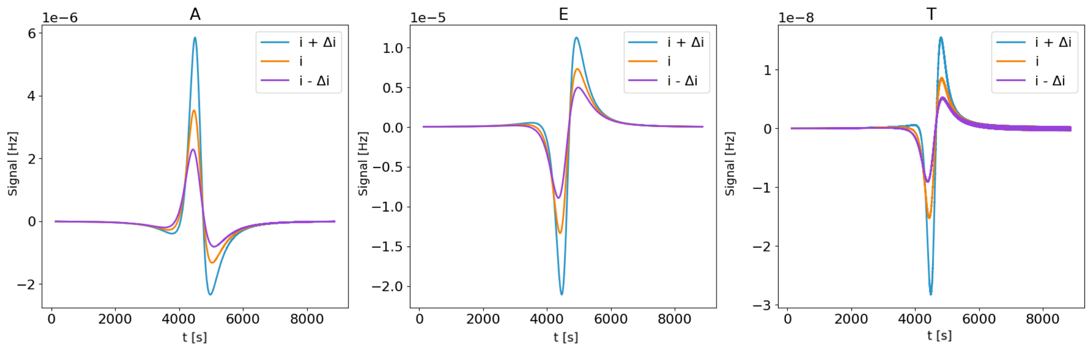

(c): TDI Signal when varying the inclination i by $\Delta\, i = 10^{-3}\, i$

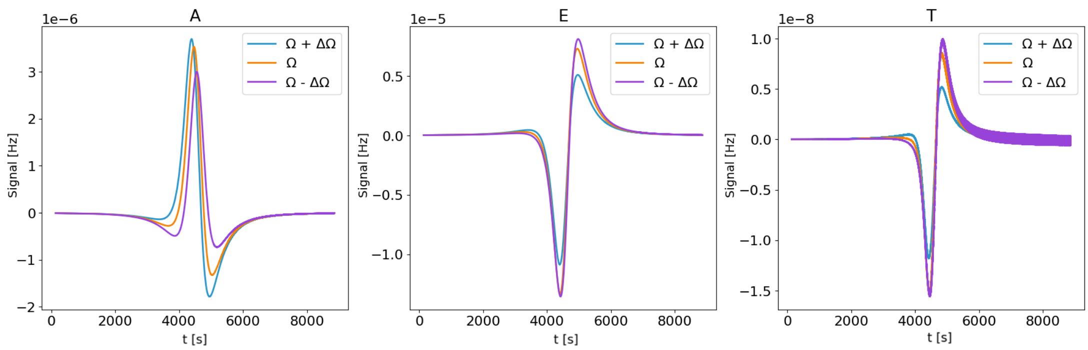

(d): TDI Signal when varying the longitude of ascending node Ω by $\Delta\, \Omega = 10^{-5}\, \Omega$

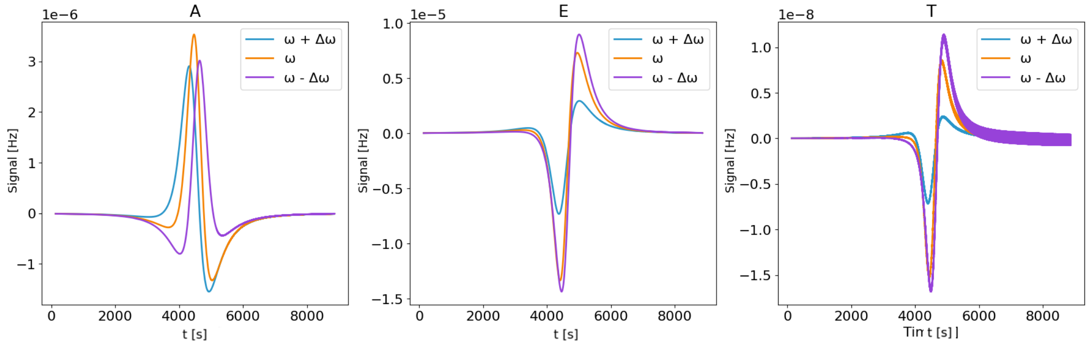

(e): TDI Signal when varying the argument of perihelion ω by $\Delta\,\omega = 10^{-5}\,\omega$

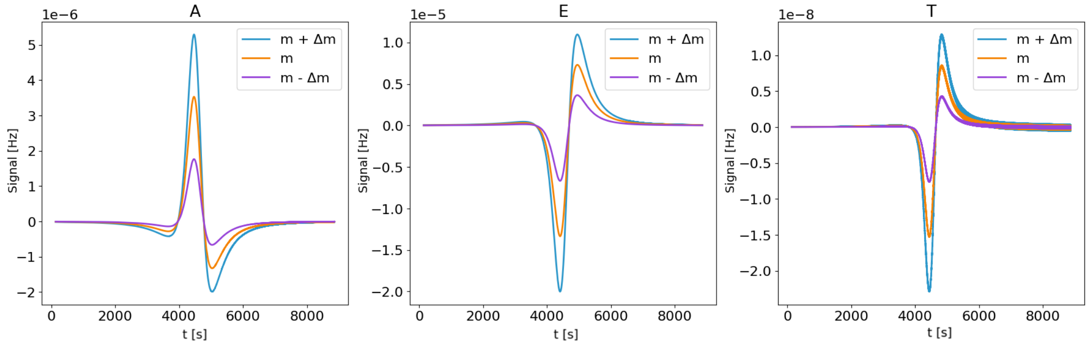

(f): TDI Signal when varying the mass m by $\Delta\,m = 0.5\,m$

Figure 3.21: Time-series TDI signal for Asteroid 1836 for variations of its parameters $\boldsymbol{\theta}$ according to $\Delta\boldsymbol{\theta} = \begin{bmatrix}10^{-5}a & 10^{-5}e & 10^{-3}i & 10^{-5}\Omega & 10^{-5}\omega & 0.5\,m_0\end{bmatrix}$. Note that each subfigure shows the TDI signal where only the respective element is varied. The presented values $\Delta\boldsymbol{\theta}$ were chosen for visualization purposes. The close approach at the MOID corresponds to $t_0 = 4700\,\mathrm{s}$.

For this asteroid in particular, we can see the impact of the variation of the different parameters. If we increase the semi-major axis, the MOID is anticipated and increase slightly the signal captured. On the other hand, a decrease in the eccentricity delays the MOID for a later time in the orbit. Surprisingly, in this case, an increase in inclination has only a direct impact in the amplitude of the signal while keeping the MOID in the same place. Additionally, an increase in the longitude of ascending node allows to have an anticipated MOID and while the signal in channel A increases, in channel E it decreases. A variation in the argument of perihelion changes the shape of the signal in channel A while impacting the amplitude in channel E. Finally, like the inclination, but here quite expected, changing the mass impacts only the amplitude of the signal. As expected, in channel T we can also see the impact of the variation of the parameters, but quite attenuated (usually 2 or 3 orders of magnitude below) and polluted with high frequency noise due to the design of the channel as an empty channel.

Each channel contains an individual data-stream, thus an individual signal and, as seen in Chapter 2.5, an individual noise. Thus, we can compute for each channel a fisher matrix as well as the corresponding covariance matrix. Additionally, it is possible to combine the information of the three fisher matrices to have a better estimate on the parameters and decrease the uncertainty (see Appendix E: Adding Fisher Matrices). So, we compute the individual fisher matrices and we add them together to find the final fisher matrix from which we can compute the covariance and correlation matrices. For Asteroid 1836, the resultant Fisher Matrix $\boldsymbol{F_{1836}}$ and Covariance Matrix $\boldsymbol{C_{1836}}$ are:

$$\boldsymbol{F_{1836}} = 10^{26} \begin{array}{c} \begin{matrix} a & e & i & \Omega & \omega & m \end{matrix} \\ \begin{pmatrix} 4.40 & -8.98 & 0.06 & -0.30 & -0.48 & 1.82\times10^{-17} \\ -8.98 & 35.38 & -0.82 & 4.81 & 7.31 & -1.03\times10^{-16} \\ 0.06 & -0.82 & 0.03 & -0.16 & -0.26 & 3.01\times10^{-18} \\ -0.30 & 4.81 & -0.16 & 1.10 & 1.59 & -1.73\times10^{-17} \\ -0.48 & 7.31 & -0.26 & 1.59 & 2.40 & -2.66\times10^{-17} \\ 1.82\times10^{-17} & -1.03\times10^{-16} & 3.01\times10^{-18} & -1.73\times10^{-17} & -2.66\times10^{-17} & 3.53\times10^{-34} \end{pmatrix} \end{array} \begin{matrix} a \\ e \\ i \\ \Omega \\ \omega \\ m \end{matrix}$$

$$\boldsymbol{C_{1836}} = 10^{-21} \begin{array}{c} \begin{matrix} a & e & i & \Omega & \omega & m \end{matrix} \\ \begin{pmatrix} 8.41 & 4.82 & 49.42 & -16.47 & 3.35 & 4.25\times10^{14} \\ 4.82 & 2.77 & 28.38 & -9.46 & 1.93 & 2.48\times10^{14} \\ 49.42 & 28.38 & 352.99 & -117.86 & 40.49 & 9.79\times10^{15} \\ -16.47 & -9.46 & -117.86 & 39.36 & -13.56 & -3.29\times10^{15} \\ 3.35 & 1.93 & 40.49 & -13.56 & 8.26 & 2.60\times10^{15} \\ 4.25\times10^{14} & 2.48\times10^{14} & 9.79\times10^{15} & -3.29\times10^{15} & 2.60\times10^{15} & 1.37\times10^{30} \end{pmatrix} \end{array} \begin{matrix} a \\ e \\ i \\ \Omega \\ \omega \\ m \end{matrix}$$

The standard deviation for each parameter $\boldsymbol{\sigma_{1836}}$ is the squared root of the diagonal of the Covariance Matrix $\boldsymbol{C_{1836}}$:

$$\boldsymbol{\sigma_{1836}} = \begin{array}{c} \begin{matrix} \sigma_a & \sigma_e & \sigma_i & \sigma_\Omega & \sigma_\omega & \sigma_m \end{matrix} \\ \begin{pmatrix} 9.17\times10^{-11}\,\mathrm{au} & 5.26\times10^{-11} & 5.94\times10^{-10}\,\mathrm{rad} & 1.98\times10^{-10}\,\mathrm{rad} & 9.09\times10^{-11}\,\mathrm{rad} & 3.71\times10^{4}\,\mathrm{kg} \end{pmatrix} \end{array}$$

The standard deviation σ_m for the mass can be translated to a normalized standard deviation $\sigma_m^* = \sigma_m/m \times 100$ corresponding to the percent accuracy on the mass. For this asteroid, the normalized standard deviation is $\sigma_m^* = 1.31 \times 10^{-6}\,\%$.

Finally, the illustrated Correlation Matrix $\boldsymbol{X_{1836}}$ is shown in Figure 3.22.

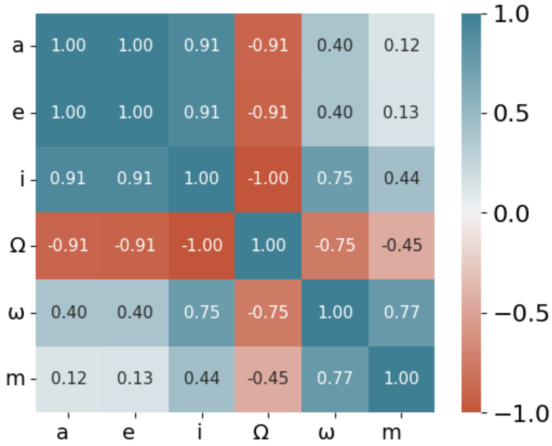

Figure 3.22: Correlation matrix $\boldsymbol{X_{1836}}$ for Asteroid 1836. The correlation scale goes from 1 (strong blue) to -1 (strong red), where the first means strongly directly correlated and the second strongly inversely correlated. A correlation value of 0 indicates no correlation between the variables. This correlation matrix is a unique matrix for the signal generated to Asteroid 1836 due to its orbital geometry as well as the geometry of the close approach and the LISA constellation at that time.

Note that the correlation matrix varies in the interval $[-1, 1]$ and, when it is is closer to -1 and 1 it corresponds to a strong inverse and direct correlation.

Due to the difference in order of magnitudes between the mass and the orbital elements we can see that there are discrepancies between the values in the Fisher matrix $\boldsymbol{F_{1836}}$, and, consequently in the Covariance matrix $\boldsymbol{C_{1836}}$. Nevertheless, the relevant results are the standard deviations for the parameters $\boldsymbol{\theta}$ and the Correlation Matrix.

From these, it can also be seen from the order of magnitude of the uncertainties that, if we have a model of Asteroid 1836 and if we manage to detect it at the MOID, we will be able to determine its properties with vast precision. This would be quite revolutionary because in a sole measurement, we would attain the parameters with standards of deviation $\boldsymbol{\sigma_{1836}}$ with an incredible accuracy. Moreover, the mass would be observed with a precision never seen before except for methods relying on close approaches with the asteroid. Notwithstanding, this level of precision would be possible because Asteroid 1836 contains a SNR of 51520.68, meaning that if detected, its signal would be quite clear and visible in the data-stream as it would not be flooded with noise.

Additionally, from the Correlation Matrix $\boldsymbol{X_{1836}}$, it is possible to distinguish the correlations related to the features on the signal. For the signal of Asteroid 1836, we can see that the longitude of ascending noise Ω is negatively correlated to all the other elements. An increase in Ω would generate a signal that would correspond to a decrease in the other parameters. This means that an increase in Ω, is as if we decreased the mass in a small way (due to the weak negative correlation) and the signal's amplitude would decrease. This effect is actually visible in Figure 3.20(d) especially for the Channel E. Furthermore, it is clear that the mass m is not strongly correlated to a, e, i and Ω, so errors in their measurements will not affect much the measurement of the mass m. Yet, there is a relatively strong correlation between $(a,\, e)$, meaning that they act in the same way, both elements modulate the amplitude of the signal somewhat in the same way (as seen in Figures 3.20(a) and 3.20(b)), so their uncertainties are related, i.e, if the measurement of e is more uncertain, so will be the one of a. There are other strong correlations for this signal, such as the pairs $(a,\, i)$, $(i,\, \omega)$ and $(\omega,\, m)$. Again the reasoning is the same, for these pairs if one measurement gets more uncertain, it will impact its pair, which can then impact the other elements it is correlated to. A matrix dominated by strong correlations means that, in the end, the model needs to be quite precise, otherwise a small variation will cause big uncertainties. As a consequence, to be able to detect this asteroid especially its orbit in a very accurate way, the model needs to be quite precise too. Note that these correlations are unique to this signal due to its distinct orbit and close approach to S/C 2.

3.4.3 Discussion of Results

In Table 3.2, the results for the standard deviation $\boldsymbol{\sigma}$ and Correlation Matrix $\boldsymbol{X}$ for other seven asteroids of the fictitious population are shown. The SNR is also presented to provide an idea of the quality of the signal detected.

Asteroid	SNR	Standard Deviation for $\boldsymbol{\theta}$	Correlation Matrix $\boldsymbol{X}$
1279	491.23	$\sigma_a = 2.04 \times 10^{-6}\,\mathrm{au}$ $\sigma_e = 1.31 \times 10^{-6}$ $\sigma_i = 2.04 \times 10^{-7}\,\mathrm{rad}$ $\sigma_\Omega = 1.17 \times 10^{-6}\,\mathrm{rad}$ $\sigma_\omega = 6.50 \times 10^{-6}\,\mathrm{rad}$ $\sigma_m^* = 3.17 \times 10^{-4}\,\%$	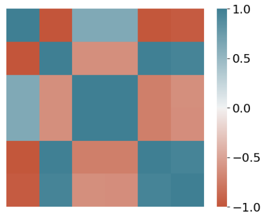
4644	28240.29	$\sigma_a = 2.62 \times 10^{-13}\,\mathrm{au}$ $\sigma_e = 1.17 \times 10^{-13}$ $\sigma_i = 1.29 \times 10^{-12}\,\mathrm{rad}$ $\sigma_\Omega = 3.42 \times 10^{-13}\,\mathrm{rad}$ $\sigma_\omega = 7.00 \times 10^{-14}\,\mathrm{rad}$ $\sigma_m^* = 1.09 \times 10^{-7}\,\%$	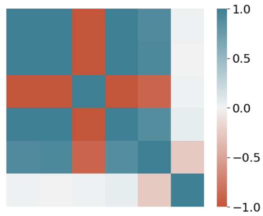
6135	235.80	$\sigma_a = 6.84 \times 10^{-7}\,\mathrm{au}$ $\sigma_e = 1.07 \times 10^{-6}$ $\sigma_i = 1.02 \times 10^{-5}\,\mathrm{rad}$ $\sigma_\Omega = 2.25 \times 10^{-6}\,\mathrm{rad}$ $\sigma_\omega = 2.59 \times 10^{-6}\,\mathrm{rad}$ $\sigma_m^* = 1.91 \times 10^{-3}\,\%$	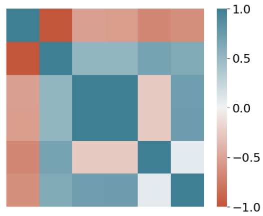
8117	6.28	$\sigma_a = 7.12 \times 10^{-5}\,\mathrm{au}$ $\sigma_e = 1..93 \times 10^{-4}$ $\sigma_i = 4.80 \times 10^{-4}\,\mathrm{rad}$ $\sigma_\Omega = 9.45 \times 10^{-6}\,\mathrm{rad}$ $\sigma_\omega = 4.68 \times 10^{-4}\,\mathrm{rad}$ $\sigma_m^* = 0.16\,\%$	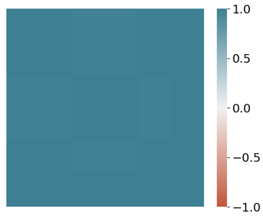
11545	3470.39	$\sigma_a = 5.30 \times 10^{-9}\,\mathrm{au}$ $\sigma_e = 2.93 \times 10^{-9}$ $\sigma_i = 1.33 \times 10^{-7}\,\mathrm{rad}$ $\sigma_\Omega = 1.46 \times 10^{-11}\,\mathrm{rad}$ $\sigma_\omega = 1.70 \times 10^{-8}\,\mathrm{rad}$ $\sigma_m^* = 1.14 \times 10^{-5}\,\%$	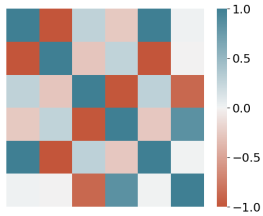
20406	90.67	$\sigma_a = 5.70 \times 10^{-7}\,\mathrm{au}$ $\sigma_e = 2.33 \times 10^{-6}$ $\sigma_i = 3.10 \times 10^{-5}\,\mathrm{rad}$ $\sigma_\Omega = 1.84 \times 10^{-7}\,\mathrm{rad}$ $\sigma_\omega = 1.31 \times 10^{-5}\,\mathrm{rad}$ $\sigma_m^* = 3.20 \times 10^{-3}\,\%$	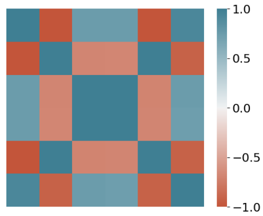
25414	19208.36	$\sigma_a = 2.18 \times 10^{-10}\,\mathrm{au}$ $\sigma_e = 3.98 \times 10^{-10}$ $\sigma_i = 2.70 \times 10^{-10}\,\mathrm{rad}$ $\sigma_\Omega = 1.70 \times 10^{-11}\,\mathrm{rad}$ $\sigma_\omega = 8.88 \times 10^{-10}\,\mathrm{rad}$ $\sigma_m^* = 3.07 \times 10^{-7}\,\%$	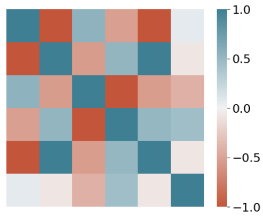

Table 3.2: Standard deviation and correlation matrix for some asteroids of the fictitious population. The orbital elements and physical properties of the tested asteroids can be found in Appendix F. The derivatives were calculated using $\boldsymbol{\Delta\theta} = \left[10^{-6}\,a \quad 10^{-6}\,e \quad 10^{-4}\,i \quad 10^{-6}\,\Omega \quad 10^{-6}\,\omega \quad 10^{-2}\,m\right]$. The SNR provided is the one for a close approach at the MOID.

It can be seen that the better we detect a signal, the lower the uncertainty as shown by the standard deviation. The correlation matrix is different for each signal as these are unique. Moreover, according to the tested population, if we detect an asteroid, its mass measurement will still be quite precise (minimum of $\sigma_m^* = 0.16\,\%$ for Asteroid 8117). This is logical, as the LISA detector is detecting variations in gravity which are quite related to the mass of the asteroid. Nevertheless, as seen from its correlation matrix, any error in one of the parameters, and the signal will not be correctly identified, which makes sense as its $\mathrm{SNR} = 6.28$ is quite low. In Tables F.4 and F.8, we can see the standard deviation for already observed asteroids and for more asteroids from the fictitious population. As observed from all these results, as soon as LISA observes well an asteroid, it will measure its orbital parameters in an accurate way with one sole measurement which can measure up to the traditional methods after multiple observations and with a great precision for the mass parameter.

Lastly, it can be seen from the results and, especially the correlation matrices, that the minimum SNR threshold for detectability is not the most suitable value. Signals with a SNR below a 10 are not well detected (flat correlation) and, even a small variation, can set off all the measurements of the parameters. So, a benchmark of $SNR = 10$ seems better suitable to be the minimum criterium for detectability.

Chapter 4

Conclusion

In this work, the possibility of using the LISA mission for the detection of NEAs was assessed. Through the different studies, several insights about the feasibility of such detections were gained.

Firstly, we understood the factors influencing NEA detectability such as: the asteroid's mass, its MOID with the spacecraft and complex geometric configurations of the LISA constellation. While heavier asteroids and those with closer approaches exhibit stronger signals, the unpredictability of LISA's geometry poses a challenge in the prediction of detectability. Some configurations are more favourable than others. However, by studying such situations, it became possible to delineate a minimum threshold for NEA detectability, providing a foundational framework for subsequent analyses.

The subsequent work delved deeper into the calculation of NEA detection probabilities through two distinct approaches. The first approach allows flexibility in orbital elements but fixes the close approach at the MOID. The second approach attempts at being more realistic and freezes the orbit to explore variations in close approach distances. Both approaches offered complementary perspectives and allowed to define an order of magnitude for the probability of detection in the different scenarios.

Finally, the uncertainty of the measurements of the LISA constellation, assuming a NEA would be detected was evaluated. By employing techniques such as the Fisher information and Bayesian statistics, we were able to derive the standard deviations and correlation of uncertainty for the asteroids in study. These analyses revealed the remarkable precision of LISA measurements, particularly if the signal is well modeled and detected. Additionally, insights from correlation matrices prompted a reassessment of the minimum SNR threshold for detectability, suggesting potential ways for refinements in future works.

In conclusion, these findings highlight the potential of using gravitational wave astronomy and the LISA mission in advancing our comprehension of the NEA population allowing for their detection and characterization. The research done does not point to a great number of close approaches and detections with the NEA population but, for the ones that will happen, we may be able to get insights into their properties, especially their mass, and, potentially, predict future close encounters with our planet.

4.1 Future Work

There are several directions for the future work, either in terms of improvements of the current work or in exploring different hypothesis and studies.

Regarding this work, the LISA system and the close approach was simplified to a two body interaction. In reality, the constellation is composed of three bodies which can all interact and contribute for the detection. In the future, it is envisioned a more realistic model for the LISA constellation and of a region of influence to improve the accuracy of some of the presented results.

Moreover, it was not presented how to extract the parameters from the signal, only how to calculate their uncertainties. The design of the models for the signals we expect to detect is a future direction of this work.

Finally, it was assumed that an asteroid could be modeled as a sphere of a certain diameter. This is typically done since because there is no way to estimate the size and shape of an asteroid without ray-tracing. But deviations from this simple model can lead to big uncertainties on the results. As prospective research, we can study the impact of different models for the shape and size of the asteroid in the results obtained.

Bibliography

[1] A. Einstein. Zur allgemeinen Relativitätstheorie. *Sitzungsberichte der Königlich Preussischen Akademie der Wissenschaften*, pages 778–786, Jan. 1915.

[2] A. Einstein. Näherungsweise Integration der Feldgleichungen der Gravitation. *Sitzungsberichte der Königlich Preussischen Akademie der Wissenschaften*, pages 688–696, Jan. 1916.

[3] A. Einstein. Über Gravitationswellen. *Sitzungsberichte der Königlich Preussischen Akademie der Wissenschaften*, pages 154–167, Jan. 1918.

[4] NASA Hubblesite. Gravitational Waves. `https://hubblesite.org/contents/articles/gravitational-waves`, Sept. 2022. Accessed: 27 November 2023.

[5] ESA. Laser Interferometer Space Antenna (LISA) Mission Concept. *LISA Project internal report number LISA-PRJ-RP-0001*, May 2009. URL `https://lisa.nasa.gov/archive2011/Documentation/LISA-PRJ-RP-0001.pdf`.

[6] P. Amaro-Seoane, H. Audley, S. Babak, J. Baker, E. Barausse, P. Bender, E. Berti, P. Binetruy, M. Born, D. Bortoluzzi, J. Camp, C. Caprini, V. Cardoso, M. Colpi, J. Conklin, N. Cornish, C. Cutler, K. Danzmann, R. Dolesi, L. Ferraioli, V. Ferroni, E. Fitzsimons, J. Gair, L. G. Bote, D. Giardini, F. Gibert, C. Grimani, H. Halloin, G. Heinzel, T. Hertog, M. Hewitson, K. Holley-Bockelmann, D. Hollington, M. Hueller, H. Inchauspe, P. Jetzer, N. Karnesis, C. Killow, A. Klein, B. Klipstein, N. Korsakova, S. L. Larson, J. Livas, I. Lloro, N. Man, D. Mance, J. Martino, I. Mateos, K. McKenzie, S. T. McWilliams, C. Miller, G. Mueller, G. Nardini, G. Nelemans, M. Nofrarias, A. Petiteau, P. Pivato, E. Plagnol, E. Porter, J. Reiche, D. Robertson, N. Robertson, E. Rossi, G. Russano, B. Schutz, A. Sesana, D. Shoemaker, J. Slutsky, C. F. Sopuerta, T. Sumner, N. Tamanini, I. Thorpe, M. Troebs, M. Vallisneri, A. Vecchio, D. Vetrugno, S. Vitale, M. Volonteri, G. Wanner, H. Ward, P. Wass, W. Weber, J. Ziemer, and P. Zweifel. LISA - A proposal in response to the ESA call for L3 mission concepts, Jan. 2017. URL `https://www.elisascience.org/files/publications/LISA_L3_20170120.pdf`.

[7] C. J. Moore, R. H. Cole, and C. P. L. Berry. Gravitational-wave sensitivity curves. *Classical & Quantum Gravity, 32(1):015014*, Dec. 2014. URL `https://dcc.ligo.org/public/0114/P1400129/003/noise_curve.pdf`.

[8] B. P. Abbott, R. Abbott, T. D. Abbott, M. R. Abernathy, F. Acernese, K. Ackley, C. Adams, T. Adams, P. Addesso, R. X. Adhikari, V. B. Adya, C. Affeldt, M. Agathos, K. Agatsuma, N. Aggarwal, O. D.

Aguiar, L. Aiello, A. Ain, P. Ajith, B. Allen, A. Allocca, P. A. Altin, S. B. Anderson, W. G. Anderson, K. Arai, M. C. Araya, C. C. Arceneaux, J. S. Areeda, N. Arnaud, K. G. Arun, S. Ascenzi, G. Ashton, M. Ast, S. M. Aston, P. Astone, P. Aufmuth, C. Aulbert, S. Babak, P. Bacon, M. K. M. Bader, F. Baldaccini, G. Ballardin, S. W. Ballmer, J. C. Barayoga, S. E. Barclay, B. C. Barish, D. Barker, F. Barone, B. Barr, L. Barsotti, M. Barsuglia, D. Barta, J. Bartlett, I. Bartos, R. Bassiri, A. Basti, J. C. Batch, C. Baune, V. Bavigadda, M. Bazzan, M. Bejger, A. S. Bell, G. Bergmann, C. P. L. Berry, D. Bersanetti, A. Bertolini, J. Betzwieser, S. Bhagwat, R. Bhandare, I. A. Bilenko, G. Billingsley, J. Birch, R. Birney, O. Birnholtz, S. Biscans, A. Bisht, M. Bitossi, C. Biwer, M. A. Bizouard, J. K. Blackburn, C. D. Blair, D. G. Blair, R. M. Blair, S. Bloemen, O. Bock, M. Boer, G. Bogaert, C. Bogan, A. Bohe, C. Bond, F. Bondu, R. Bonnand, B. A. Boom, R. Bork, V. Boschi, S. Bose, Y. Bouffanais, A. Bozzi, C. Bradaschia, V. B. Braginsky, M. Branchesi, J. E. Brau, T. Briant, A. Brillet, M. Brinkmann, V. Brisson, P. Brockill, J. E. Broida, A. F. Brooks, D. A. Brown, D. D. Brown, N. M. Brown, S. Brunett, C. C. Buchanan, A. Buikema, T. Bulik, H. J. Bulten, A. Buonanno, D. Buskulic, C. Buy, R. L. Byer, M. Cabero, L. Cadonati, G. Cagnoli, C. Cahillane, J. C. Bustillo, T. Callister, E. Calloni, J. B. Camp, K. C. Cannon, J. Cao, C. D. Capano, E. Capocasa, F. Carbognani, S. Caride, J. Casanueva Diaz, C. Casentini, S. Caudill, M. Cavaglià, F. Cavalier, R. Cavalieri, G. Cella, C. B. Cepeda, L. Cerboni Baiardi, G. Cerretani, E. Cesarini, S. J. Chamberlin, M. Chan, S. Chao, P. Charlton, E. Chassande-Mottin, H. Y. Chen, Y. Chen, C. Cheng, A. Chincarini, A. Chiummo, H. S. Cho, M. Cho, J. H. Chow, N. Christensen, Q. Chu, S. Chua, S. Chung, G. Ciani, F. Clara, J. A. Clark, F. Cleva, E. Coccia, P. Cohadon, A. Colla, C. G. Collette, L. Cominsky, M. Constancio, A. Conte, L. Conti, D. Cook, T. R. Corbitt, A. Corsi, S. Cortese, C. A. Costa, M. W. Coughlin, S. B. Coughlin, J. Coulon, S. T. Countryman, P. Couvares, E. E. Cowan, D. M. Coward, M. J. Cowart, D. C. Coyne, R. Coyne, K. Craig, J. D. E. Creighton, J. Cripe, S. G. Crowder, A. Cumming, L. Cunningham, E. Cuoco, T. Dal Canton, S. L. Danilishin, S. D'Antonio, K. Danzmann, N. S. Darman, A. Dasgupta, C. F. Da Silva Costa, V. Dattilo, I. Dave, M. Davier, G. S. Davies, E. J. Daw, R. Day, S. De, D. DeBra, G. Debreczeni, J. Degallaix, M. De Laurentis, S. Deléglise, W. Del Pozzo, T. Denker, T. Dent, V. Dergachev, R. De Rosa, R. T. DeRosa, R. DeSalvo, R. C. Devine, S. Dhurandhar, M. C. Díaz, L. D. Fiore, M. D. Giovanni, T. D. Girolamo, A. D. Lieto, S. D. Pace, I. D. Palma, A. D. Virgilio, V. Dolique, F. Donovan, K. L. Dooley, S. Doravari, R. Douglas, T. P. Downes, M. Drago, R. W. P. Drever, J. C. Driggers, M. Ducrot, S. E. Dwyer, T. B. Edo, M. C. Edwards, A. Effler, H. Eggenstein, P. Ehrens, J. Eichholz, S. S. Eikenberry, W. Engels, R. C. Essick, T. Etzel, M. Evans, T. M. Evans, R. Everett, M. Factourovich, V. Fafone, H. Fair, S. Fairhurst, X. Fan, Q. Fang, S. Farinon, B. Farr, W. M. Farr, M. Favata, M. Fays, H. Fehrmann, M. M. Fejer, E. Fenyvesi, I. Ferrante, E. C. Ferreira, F. Ferrini, F. Fidecaro, I. Fiori, D. Fiorucci, R. P. Fisher, R. Flaminio, M. Fletcher, J. Fournier, S. Frasca, F. Frasconi, Z. Frei, A. Freise, R. Frey, V. Frey, P. Fritschel, V. V. Frolov, P. Fulda, M. Fyffe, H. A. G. Gabbard, J. R. Gair, L. Gammaitoni, S. G. Gaonkar, F. Garufi, G. Gaur, N. Gehrels, G. Gemme, P. Geng, E. Genin, A. Gennai, J. George, L. Gergely, V. Germain, A. Ghosh, A. Ghosh, S. Ghosh, J. A. Giaime, K. D. Giardina, A. Giazotto, K. Gill, A. Glaefke, E. Goetz, R. Goetz, L. Gondan, G. González, J. M. Gonzalez Castro, A. Gopakumar, N. A. Gordon, M. L. Gorodetsky, S. E.

Gossan, M. Gosselin, R. Gouaty, A. Grado, C. Graef, P. B. Graff, M. Granata, A. Grant, S. Gras, C. Gray, G. Greco, A. C. Green, P. Groot, H. Grote, S. Grunewald, G. M. Guidi, X. Guo, A. Gupta, M. K. Gupta, K. E. Gushwa, E. K. Gustafson, R. Gustafson, J. J. Hacker, B. R. Hall, E. D. Hall, G. Hammond, M. Haney, M. M. Hanke, J. Hanks, C. Hanna, M. D. Hannam, J. Hanson, T. Hardwick, J. Harms, G. M. Harry, I. W. Harry, M. J. Hart, M. T. Hartman, C. Haster, K. Haughian, A. Heidmann, M. C. Heintze, H. Heitmann, P. Hello, G. Hemming, M. Hendry, I. S. Heng, J. Hennig, J. Henry, A. W. Heptonstall, M. Heurs, S. Hild, D. Hoak, D. Hofman, K. Holt, D. E. Holz, P. Hopkins, J. Hough, E. A. Houston, E. J. Howell, Y. M. Hu, S. Huang, E. A. Huerta, D. Huet, B. Hughey, S. Husa, S. H. Huttner, T. Huynh-Dinh, N. Indik, D. R. Ingram, R. Inta, H. N. Isa, J. Isac, M. Isi, T. Isogai, B. R. Iyer, K. Izumi, T. Jacqmin, H. Jang, K. Jani, P. Jaranowski, S. Jawahar, L. Jian, F. Jiménez-Forteza, W. W. Johnson, D. I. Jones, R. Jones, R. J. G. Jonker, L. Ju, H. K, C. V. Kalaghatgi, V. Kalogera, S. Kandhasamy, G. Kang, J. B. Kanner, S. J. Kapadia, S. Karki, K. S. Karvinen, M. Kasprzack, E. Katsavounidis, W. Katzman, S. Kaufer, T. Kaur, K. Kawabe, F. Kéfélian, M. S. Kehl, D. Keitel, D. B. Kelley, W. Kells, R. Kennedy, J. S. Key, F. Y. Khalili, I. Khan, S. Khan, Z. Khan, E. A. Khazanov, N. Kijbunchoo, C. Kim, C. Kim, J. Kim, K. Kim, N. Kim, W. Kim, Y. Kim, S. J. Kimbrell, E. J. King, P. J. King, J. S. Kissel, B. Klein, L. Kleybolte, S. Klimenko, S. M. Koehlenbeck, S. Koley, V. Kondrashov, A. Kontos, M. Korobko, W. Z. Korth, I. Kowalska, D. B. Kozak, V. Kringel, B. Krishnan, A. Królak, C. Krueger, G. Kuehn, P. Kumar, R. Kumar, L. Kuo, A. Kutynia, B. D. Lackey, M. Landry, J. Lange, B. Lantz, P. D. Lasky, M. Laxen, A. Lazzarini, C. Lazzaro, P. Leaci, S. Leavey, E. O. Lebigot, C. H. Lee, H. K. Lee, H. M. Lee, K. Lee, A. Lenon, M. Leonardi, J. R. Leong, N. Leroy, N. Letendre, Y. Levin, J. B. Lewis, T. G. F. Li, A. Libson, T. B. Littenberg, N. A. Lockerbie, A. L. Lombardi, L. T. London, J. E. Lord, M. Lorenzini, V. Loriette, M. Lormand, G. Losurdo, J. D. Lough, H. Lück, A. P. Lundgren, R. Lynch, Y. Ma, B. Machenschalk, M. MacInnis, D. M. Macleod, F. Magaña-Sandoval, L. M. Zertuche, R. M. Magee, E. Majorana, I. Maksimovic, V. Malvezzi, N. Man, V. Mandic, V. Mangano, G. L. Mansell, M. Manske, M. Mantovani, F. Marchesoni, F. Marion, S. Márka, Z. Márka, A. S. Markosyan, E. Maros, F. Martelli, L. Martellini, I. W. Martin, D. V. Martynov, J. N. Marx, K. Mason, A. Masserot, T. J. Massinger, M. Masso-Reid, S. Mastrogiovanni, F. Matichard, L. Matone, N. Mavalvala, N. Mazumder, R. McCarthy, D. E. McClelland, S. McCormick, S. C. McGuire, G. McIntyre, J. McIver, D. J. McManus, T. McRae, D. Meacher, G. D. Meadors, J. Meidam, A. Melatos, G. Mendell, R. A. Mercer, E. L. Merilh, M. Merzougui, S. Meshkov, C. Messenger, C. Messick, R. Metzdorff, P. M. Meyers, F. Mezzani, H. Miao, C. Michel, H. Middleton, E. E. Mikhailov, L. Milano, A. L. Miller, A. Miller, B. B. Miller, J. Miller, M. Millhouse, Y. Minenkov, J. Ming, S. Mirshekari, C. Mishra, S. Mitra, V. P. Mitrofanov, G. Mitselmakher, R. Mittleman, A. Moggi, M. Mohan, S. R. P. Mohapatra, M. Montani, B. C. Moore, C. J. Moore, D. Moraru, G. Moreno, S. R. Morriss, K. Mossavi, B. Mours, C. M. Mow-Lowry, G. Mueller, A. W. Muir, A. Mukherjee, D. Mukherjee, S. Mukherjee, N. Mukund, A. Mullavey, J. Munch, D. J. Murphy, P. G. Murray, A. Mytidis, I. Nardecchia, L. Naticchioni, R. K. Nayak, K. Nedkova, G. Nelemans, T. J. N. Nelson, M. Neri, A. Neunzert, G. Newton, T. T. Nguyen, A. B. Nielsen, S. Nissanke, A. Nitz, F. Nocera, D. Nolting, M. E. N. Normandin, L. K. Nuttall, J. Oberling, E. Ochsner, J. O'Dell, E. Oelker, G. H. Ogin, J. J. Oh, S. H. Oh, F. Ohme,

M. Oliver, P. Oppermann, R. J. Oram, B. O'Reilly, R. O'Shaughnessy, D. J. Ottaway, H. Overmier, B. J. Owen, A. Pai, S. A. Pai, J. R. Palamos, O. Palashov, C. Palomba, A. Pal-Singh, H. Pan, C. Pankow, F. Pannarale, B. C. Pant, F. Paoletti, A. Paoli, M. A. Papa, H. R. Paris, W. Parker, D. Pascucci, A. Pasqualetti, R. Passaquieti, D. Passuello, B. Patricelli, Z. Patrick, B. L. Pearlstone, M. Pedraza, R. Pedurand, L. Pekowsky, A. Pele, S. Penn, A. Perreca, L. M. Perri, M. Phelps, O. J. Piccinni, M. Pichot, F. Piergiovanni, V. Pierro, G. Pillant, L. Pinard, I. M. Pinto, M. Pitkin, M. Poe, R. Poggiani, P. Popolizio, A. Post, J. Powell, J. Prasad, J. Pratt, V. Predoi, T. Prestegard, L. R. Price, M. Prijatelj, M. Principe, S. Privitera, R. Prix, G. A. Prodi, L. Prokhorov, O. Puncken, M. Punturo, P. Puppo, M. Pürrer, H. Qi, J. Qin, S. Qiu, V. Quetschke, E. A. Quintero, R. Quitzow-James, F. J. Raab, D. S. Rabeling, H. Radkins, P. Raffai, S. Raja, C. Rajan, M. Rakhmanov, P. Rapagnani, V. Raymond, M. Razzano, V. Re, J. Read, C. M. Reed, T. Regimbau, L. Rei, S. Reid, H. Rew, S. D. Reyes, F. Ricci, K. Riles, M. Rizzo, N. A. Robertson, R. Robie, F. Robinet, A. Rocchi, L. Rolland, J. G. Rollins, V. J. Roma, J. D. Romano, R. Romano, G. Romanov, J. H. Romie, D. Rosińska, S. Rowan, A. Rüdiger, P. Ruggi, K. Ryan, S. Sachdev, T. Sadecki, L. Sadeghian, M. Sakellariadou, L. Salconi, M. Saleem, F. Salemi, A. Samajdar, L. Sammut, E. J. Sanchez, V. Sandberg, B. Sandeen, J. R. Sanders, B. Sassolas, P. R. Saulson, O. E. S. Sauter, R. L. Savage, A. Sawadsky, P. Schale, R. Schilling, J. Schmidt, P. Schmidt, R. Schnabel, R. M. S. Schofield, A. Schönbeck, E. Schreiber, D. Schuette, B. F. Schutz, J. Scott, S. M. Scott, D. Sellers, A. S. Sengupta, D. Sentenac, V. Sequino, A. Sergeev, Y. Setyawati, D. A. Shaddock, T. Shaffer, M. S. Shahriar, M. Shaltev, B. Shapiro, P. Shawhan, A. Sheperd, D. H. Shoemaker, D. M. Shoemaker, K. Siellez, X. Siemens, M. Sieniawska, D. Sigg, A. D. Silva, A. Singer, L. P. Singer, A. Singh, R. Singh, A. Singhal, A. M. Sintes, B. J. J. Slagmolen, J. R. Smith, N. D. Smith, R. J. E. Smith, E. J. Son, B. Sorazu, F. Sorrentino, T. Souradeep, A. K. Srivastava, A. Staley, M. Steinke, J. Steinlechner, S. Steinlechner, D. Steinmeyer, B. C. Stephens, R. Stone, K. A. Strain, N. Straniero, G. Stratta, N. A. Strauss, S. Strigin, R. Sturani, A. L. Stuver, T. Z. Summerscales, L. Sun, S. Sunil, P. J. Sutton, B. L. Swinkels, M. J. Szczepańczyk, M. Tacca, D. Talukder, D. B. Tanner, M. Tápai, S. P. Tarabrin, A. Taracchini, R. Taylor, T. Theeg, M. P. Thirugnanasambandam, E. G. Thomas, M. Thomas, P. Thomas, K. A. Thorne, K. S. Thorne, E. Thrane, S. Tiwari, V. Tiwari, K. V. Tokmakov, K. Toland, C. Tomlinson, M. Tonelli, Z. Tornasi, C. V. Torres, C. I. Torrie, D. Töyrä, F. Travasso, G. Traylor, D. Trifirò, M. C. Tringali, L. Trozzo, M. Tse, M. Turconi, D. Tuyenbayev, D. Ugolini, C. S. Unnikrishnan, A. L. Urban, S. A. Usman, H. Vahlbruch, G. Vajente, G. Valdes, N. van Bakel, M. van Beuzekom, J. F. J. van den Brand, C. Van Den Broeck, D. C. Vander-Hyde, L. van der Schaaf, J. V. van Heijningen, A. A. van Veggel, M. Vardaro, S. Vass, M. Vasúth, R. Vaulin, A. Vecchio, G. Vedovato, J. Veitch, P. J. Veitch, K. Venkateswara, D. Verkindt, F. Vetrano, A. Viceré, S. Vinciguerra, D. J. Vine, J. Vinet, S. Vitale, T. Vo, H. Vocca, C. Vorvick, D. V. Voss, W. D. Vousden, S. P. Vyatchanin, A. R. Wade, L. E. Wade, M. Wade, M. Walker, L. Wallace, S. Walsh, G. Wang, H. Wang, M. Wang, X. Wang, Y. Wang, R. L. Ward, J. Warner, M. Was, B. Weaver, L. Wei, M. Weinert, A. J. Weinstein, R. Weiss, L. Wen, P. Weßels, T. Westphal, K. Wette, J. T. Whelan, B. F. Whiting, R. D. Williams, A. R. Williamson, J. L. Willis, B. Willke, M. H. Wimmer, W. Winkler, C. C. Wipf, A. G. Wiseman, H. Wittel, G. Woan,

J. Woehler, J. Worden, J. L. Wright, D. S. Wu, G. Wu, J. Yablon, W. Yam, H. Yamamoto, C. C. Yancey, H. Yu, M. Yvert, A. Zadrożny, L. Zangrando, M. Zanolin, J. Zendri, M. Zevin, L. Zhang, M. Zhang, Y. Zhang, C. Zhao, M. Zhou, Z. Zhou, X. J. Zhu, M. E. Zucker, S. E. Zuraw, and J. Zweizig. The basic physics of the binary black hole merger gw150914. *Annalen der Physik*, 529(1–2), Oct. 2016. ISSN 1521-3889. doi: 10.1002/andp.201600209. URL http://dx.doi.org/10.1002/andp.201600209.

[9] NASA Jet Propulsion Laboratory. NEO Basics. https://cneos.jpl.nasa.gov/about/basics.html. Accessed: 27 November 2023.

[10] ESA Near-Earth Objects Coordination Centre. Discovery Statistics. https://neo.ssa.esa.int/discovery-statistics. Accessed: 27 November 2023.

[11] C. Gauss. *Theoria motus corporum coelestium in sectionibus conicis solem ambientium*. Carl Friedrich Gauss Werke. sumtibus Frid. Perthes et I. H. Besser, 1809. URL https://books.google.fr/books?id=ORUOAAAAQAAJ.

[12] K. Muinonen, J. Berthier, A. Cellino, P. David, F. De Angeli, M. Delbó, A. Dell-Oro, L. Galluccio, D. Hestroffer, F. Mignard, T. Pauwels, F. Spoto, and P. Tanga. Gaia DR3 documentation Chapter 8: Solar System Objects. Gaia DR3 documentation, European Space Agency; Gaia Data Processing and Analysis Consortium., June 2022. URL https://gea.esac.esa.int/archive/documentation/GDR3/index.html.

[13] E. Bowell, J. Virtanen, K. Muinonen, and A. Boattini. Asteroid orbit computation. *Asteroids III*, 01 2002.

[14] J. Desmars, D. Bancelin, D. Hestroffer, and W. Thuillot. Statistical and numerical study of asteroid orbital uncertainty. *Astronomy & Astrophysics*, 554(A32), June 2013. doi: 10.1051/0004-6361/201321090. URL https://doi.org/10.1051/0004-6361/201321090.

[15] G. Michalak. Determination of asteroid masses — I. (1) Ceres, (2) Pallas and (4) Vesta. *Astronomy and Astrophysics*, 360:363–374, Aug. 2000. URL https://ui.adsabs.harvard.edu/abs/2000A&A...360..363M.

[16] G. Michalak. Determination of asteroid masses. II. (6) Hebe, (10) Hygiea, (15) Eunomia, (52) Europa, (88) Thisbe, (444) Gyptis, (511) Davida and (704) Interamnia. *Astronomy and Astrophysics*, 374:703–711, Aug. 2001. doi: 10.1051/0004-6361:20010731. URL https://ui.adsabs.harvard.edu/abs/2001A&A...374..703M.

[17] W. M. Folkner, J. G. Williams, and D. H. Boggs. The Planetary and Lunar Ephemeris DE 421. *Interplanetary Network Progress Report*, 42-178:1–34, Aug. 2009.

[18] J. Baer, S. R. Chesley, and R. D. Matson. Astrometric Masses of 26 Asteroids and Observations on Asteroid Porosity. *The Astronomical Journal*, 141(5):143, Mar. 2011. doi: 10.1088/0004-6256/141/5/143. URL https://dx.doi.org/10.1088/0004-6256/141/5/143.

[19] A. Fujiwara, J. Kawaguchi, D. K. Yeomans, M. Abe, T. Mukai, T. Okada, J. Saito, H. Yano, M. Yoshikawa, D. J. Scheeres, O. Barnouin-Jha, A. F. Cheng, H. Demura, R. W. Gaskell, N. Hirata, H. Ikeda, T. Kominato, H. Miyamoto, A. M. Nakamura, R. Nakamura, S. Sasaki, and K. Uesugi. The Rubble-Pile Asteroid Itokawa as Observed by Hayabusa. *Science*, 312(5778):1330–1334, June 2006. doi: 10.1126/science.1125841.

[20] M. Pätzold, T. P. Andert, B. Häusler, S. Tellmann, J. D. Anderson, S. W. Asmar, J. P. Barriot, and M. K. Bird. (21) Lutetia - Low Mass, High Density. *Science*, 334:491–492, Oct. 2011. doi: 10.1126/science.1209389. URL `https://www.science.org/doi/10.1126/science.1209389?url_ver=Z39.88-2003&rfr_id=ori:rid:crossref.org&rfr_dat=cr_pub%20%200pubmed`.

[21] J. Petit, D. D. Durda, R. Greenberg, T. Hurford, and P. Geissler. The Long-Term Dynamics of Dactyl's Orbit. *Icarus*, 130(1):177–197, 1997. ISSN 0019-1035. doi: https://doi.org/10.1006/icar.1997.5788. URL `https://www.sciencedirect.com/science/article/pii/S0019103597957882`.

[22] J. L. Margot, M. C. Nolan, L. A. M. Benner, S. J. Ostro, R. F. Jurgens, J. D. Giorgini, M. A. Slade, and D. B. Campbell. Binary Asteroids in the Near-Earth Object Population. *Science*, 296(5572): 1445–1448, 2002. doi: 10.1126/science.1072094. URL `https://www.science.org/doi/abs/10.1126/science.1072094`.

[23] W. Zielenbach. Mass Determination Studies of 104 Large Asteroids. *The Astronomical Journal*, 142(4):120, Oct. 2011. doi: 10.1088/0004-6256/142/4/120. URL `https://ui.adsabs.harvard.edu/abs/2011AJ....142..120Z`.

[24] P. Pravec and A. W. Harris. Binary asteroid population: 1. Angular momentum content. *Icarus*, 190(1):250–259, 2007. ISSN 0019-1035. doi: https://doi.org/10.1016/j.icarus.2007.02.023. URL `https://www.sciencedirect.com/science/article/pii/S0019103507001388`.

[25] E. F. Tedesco, P. V. Noah, M. Noah, and S. D. Price. The Supplemental IRAS Minor Planet Survey. *The Astronomical Journal*, 123(2):1056, Feb. 2002. doi: 10.1086/338320. URL `https://dx.doi.org/10.1086/338320`.

[26] E. L. Ryan and C. E. Woodward. Rectified Asteroid Albedos and Diameters from IRAS and MSX Photometry Catalogs. *The Astronomical Journal*, 140(4):933, Aug. 2010. doi: 10.1088/0004-6256/140/4/933. URL `https://dx.doi.org/10.1088/0004-6256/140/4/933`.

[27] M. E. Brown and C. A. Trujillo. Direct Measurement of the Size of the Large Kuiper Belt Object (50000) Quaoar. *The Astronomical Journal*, 127(4):2413, Apr. 2004. doi: 10.1086/382513. URL `https://dx.doi.org/10.1086/382513`.

[28] F. Marchis, M. Kaasalainen, E. Hom, J. Berthier, J. Enriquez, D. Hestroffer, D. Le Mignant, and I. de Pater. Shape, size and multiplicity of main-belt asteroids: I. Keck Adaptive Optics survey. *Icarus*, 185(1):39–63, 2006. ISSN 0019-1035. doi: https://doi.org/10.1016/j.icarus.2006.06.001. URL `https://www.sciencedirect.com/science/article/pii/S0019103506001990`.

[29] J. Drummond, J. Christou, and J. Nelson. Triaxial ellipsoid dimensions and poles of asteroids from AO observations at the Keck-II telescope. *Icarus*, 202(1):147–159, 2009. ISSN 0019-1035. doi: https://doi.org/10.1016/j.icarus.2009.02.011. URL `https://www.sciencedirect.com/science/article/pii/S001910350900075X`.

[30] B. Carry. Density of asteroids. *Planetary and Space Science*, 73(1):98–118, 2012. ISSN 0032-0633. doi: https://doi.org/10.1016/j.pss.2012.03.009. URL `https://www.sciencedirect.com/science/article/pii/S0032063312000773`.

[31] J. Hough. Long Baseline Gravitational Wave Detectors – Status and Developments. *Journal of Physics: Conference Series*, 66(1):012002, May 2007. doi: 10.1088/1742-6596/66/1/012002. URL `https://dx.doi.org/10.1088/1742-6596/66/1/012002`.

[32] D. Shoemaker. Ground-based Interferometric Gravitational-Wave Detectors in the LISA Epoch. *Classical and Quantum Gravity*, 20(10):S11, Apr. 2003. doi: 10.1088/0264-9381/20/10/302. URL `https://dx.doi.org/10.1088/0264-9381/20/10/302`.

[33] N. A. Robertson. Laser Interferometric Gravitational Wave Detectors. *Classical and Quantum Gravity*, 17(15):R19, Aug. 2000. doi: 10.1088/0264-9381/17/15/201. URL `https://dx.doi.org/10.1088/0264-9381/17/15/201`.

[34] P. McNamara, S. Vitale, and K. Danzmann. LISA Pathfinder. *Classical and Quantum Gravity*, 25(11):114034, May 2008. doi: 10.1088/0264-9381/25/11/114034. URL `https://dx.doi.org/10.1088/0264-9381/25/11/114034`.

[35] M. Armano, H. Audley, G. Auger, J. T. Baird, M. Bassan, P. Binetruy, M. Born, D. Bortoluzzi, N. Brandt, M. Caleno, L. Carbone, A. Cavalleri, A. Cesarini, G. Ciani, G. Congedo, A. M. Cruise, K. Danzmann, M. de Deus Silva, R. De Rosa, M. Diaz-Aguiló, L. Di Fiore, I. Diepholz, G. Dixon, R. Dolesi, N. Dunbar, L. Ferraioli, V. Ferroni, W. Fichter, E. D. Fitzsimons, R. Flatscher, M. Freschi, A. F. García Marín, C. García Marirrodriga, R. Gerndt, L. Gesa, F. Gibert, D. Giardini, R. Giusteri, F. Guzmán, A. Grado, C. Grimani, A. Grynagier, J. Grzymisch, I. Harrison, G. Heinzel, M. Hewitson, D. Hollington, D. Hoyland, M. Hueller, H. Inchauspé, O. Jennrich, P. Jetzer, U. Johann, B. Johlander, N. Karnesis, B. Kaune, N. Korsakova, C. J. Killow, J. A. Lobo, I. Lloro, L. Liu, J. P. López-Zaragoza, R. Maarschalkerweerd, D. Mance, V. Martín, L. Martin-Polo, J. Martino, F. Martin-Porqueras, S. Madden, I. Mateos, P. W. McNamara, J. Mendes, L. Mendes, A. Monsky, D. Nicolodi, M. Nofrarias, S. Paczkowski, M. Perreur-Lloyd, A. Petiteau, P. Pivato, E. Plagnol, P. Prat, U. Ragnit, B. Raïs, J. Ramos-Castro, J. Reiche, D. I. Robertson, H. Rozemeijer, F. Rivas, G. Russano, J. Sanjuán, P. Sarra, A. Schleicher, D. Shaul, J. Slutsky, C. F. Sopuerta, R. Stanga, F. Steier, T. Sumner, D. Texier, J. I. Thorpe, C. Trenkel, M. Tröbs, H. B. Tu, D. Vetrugno, S. Vitale, V. Wand, G. Wanner, H. Ward, C. Warren, P. J. Wass, D. Wealthy, W. J. Weber, L. Wissel, A. Wittchen, A. Zambotti, C. Zanoni, T. Ziegler, and P. Zweifel. Sub-Femto-g Free Fall for Space-Based Gravitational Wave Observatories: LISA Pathfinder Results. *Phys. Rev. Lett.*, 116:231101, June 2016. doi: 10.1103/PhysRevLett.116.231101. URL `https://link.aps.org/doi/10.1103/PhysRevLett.116.231101`.

[36] J.-Y. Vinet. LISA and asteroids. *Classical and Quantum Gravity*, 23(15):4939, July 2006. doi: 10.1088/0264-9381/23/15/012. URL https://dx.doi.org/10.1088/0264-9381/23/15/012.

[37] H. D. Curtis. *Orbital Mechanics: For Engineering Students*. Butterworth-Heinemann, Sept. 2013. ISBN 978-0-08-097747-8. doi: https://doi.org/10.1016/B978-0-08-097747-8.00012-8. URL https://www.sciencedirect.com/science/article/pii/B9780080977478000128.

[38] W. Wiesel. *Spaceflight Dynamics*. McGraw-Hill, 1997. ISBN 9780070701106. URL https://books.google.fr/books?id=ROZHAQAAIAAJ.

[39] A. Morbidelli, M. Delbo, M. Granvik, W. Bottke, R. Jedicke, B. Bolin, P. Michel, and D. Vokrouhlicky. Debiased albedo distribution for near earth objects. *Icarus*, 340:113631, 2020. ISSN 0019-1035. doi: https://doi.org/10.1016/j.icarus.2020.113631. URL https://www.sciencedirect.com/science/article/pii/S0019103519303872.

[40] P. Pravec, A. W. Harris, P. Kušnirák, A. Galád, and K. Hornoch. Absolute magnitudes of asteroids and a revision of asteroid albedo estimates from wise thermal observations. *Icarus*, 221(1):365–387, 2012. ISSN 0019-1035. doi: https://doi.org/10.1016/j.icarus.2012.07.026. URL https://www.sciencedirect.com/science/article/pii/S0019103512003028.

[41] H. Karttunen, P. Kröger, H. Oja, M. Poutanen, and K. J. Donner. *Fundamental Astronomy*. Springer Berlin, Heidelberg, Nov. 2016. doi: 10.1007/978-3-662-53045-0. URL https://doi.org/10.1007/978-3-662-53045-0.

[42] Near-Earth Objects Coordination Centre. Definitions and Assumptions. URL https://neo.ssa.esa.int/definitions-assumptions. Accessed: 31 January 2024.

[43] M. Mahlke, B. Carry, and P.-A. Mattei. Asteroid Taxonomy from Cluster Analysis of Spectrometry and Albedo. *Astronomy & Astrophysics*, 665(A26), 2022. doi: 10.1051/0004-6361/202243587. URL https://doi.org/10.1051/0004-6361/202243587.

[44] E. F. Tedesco, G. J. Veeder, J. W. Fowler, and J. R. Chillemi. *The IRAS Minor Planet Survey*. Phillips Laboratory, Dec. 1992. URL https://ntrs.nasa.gov/citations/19940005152.

[45] Z. Chen, C. Fang, Z. Wang, C. Yan, and Z. Wang. The Influence of On-Orbit Micro-Vibration on Space Gravitational Wave Detection. *Photonics*, 10(8), Dec. 2023. ISSN 2304-6732. doi: 10.3390/photonics10080908. URL https://www.mdpi.com/2304-6732/10/8/908.

[46] I. Newton, D. Bernoulli, C. MacLaurin, and L. Euler. *Philosophiae naturalis principia mathematica*, volume 1. excudit G. Brookman; impensis TT et J. Tegg, Londini, 1833.

[47] M. Otto. Time-Delay Interferometry Simulations for the Laser Interferometer Space Antenna. 2015. doi: 10.15488/8545. URL https://doi.org/10.15488/8545.

[48] T. A. Prince, M. Tinto, S. L. Larson, and J. W. Armstrong. LISA optimal sensitivity. *Physical Review D*, 66(12), Dec. 2002. ISSN 1089-4918. doi: 10.1103/physrevd.66.122002. URL http://dx.doi.org/10.1103/PhysRevD.66.122002.

[49] J. I. Thorpe. LISA long-arm interferometry. *Classical and Quantum Gravity*, 27(8):084008, Apr. 2010. doi: 10.1088/0264-9381/27/8/084008. URL https://dx.doi.org/10.1088/0264-9381/27/8/084008.

[50] Q. Baghi, N. Karnesis, J.-B. Bayle, M. Besançon, and H. Inchauspé. Uncovering gravitational-wave backgrounds from noises of unknown shape with LISA. *Journal of Cosmology and Astroparticle Physics*, 2023(04):066, Apr. 2023. ISSN 1475-7516. doi: 10.1088/1475-7516/2023/04/066. URL http://dx.doi.org/10.1088/1475-7516/2023/04/066.

[51] M. Tinto and S. V. Dhurandhar. Time-delay interferometry. *Living Reviews in Relativity*, 24(4), July 2005. doi: 10.1007/s41114-020-00029-6. URL https://doi.org/10.1007/s41114-020-00029-6.

[52] J. W. Armstrong, F. B. Estabrook, and M. Tinto. Time-delay interferometry for space-based gravitational wave searches. *The Astrophysical Journal*, 527(2):814, Dec. 1999. doi: 10.1086/308110. URL https://dx.doi.org/10.1086/308110.

[53] T. Robson, N. J. Cornish, and C. Liu. The Construction and Use of LISA Sensitivity Curves. *Classical and Quantum Gravity*, 36(10):105011, Apr. 2019. doi: 10.1088/1361-6382/ab1101. URL https://doi.org/10.1088%2F1361-6382%2Fab1101.

[54] S. Haykin. *Communication Systems*. Wiley Eastern, 2001. ISBN 9789971513054. URL https://books.google.fr/books?id=aqAVQwAACAAJ.

[55] S. Babak, M. Hewitson, and A. Petiteau. LISA Sensitivity and SNR Calculations, Aug. 2021. URL https://doi.org/10.48550/arXiv.2108.01167.

[56] D. Q. Nam, Y. Lemiere, A. Petiteau, J.-B. Bayle, O. Hartwig, J. Martino, and M. Staab. TDI Noises Transfer Functions for LISA, Nov. 2022. URL https://doi.org/10.48550/arXiv.2211.02539.

[57] L. Lyons. Discovering the significance of 5 sigma, Oct. 2013. URL https://doi.org/10.48550/arXiv.1310.1284.

[58] W. F. Bottke, R. Jedicke, A. Morbidelli, J.-M. Petit, and B. Gladman. Understanding the distribution of near-earth asteroids. *Science*, 288(5474):2190–2194, 2000. ISSN 00368075, 10959203. URL http://www.jstor.org/stable/3075378.

[59] M. Granvik, A. Morbidelli, R. Jedicke, B. Bolin, W. F. Bottke, E. Beshore, D. Vokrouhlický, D. Nesvorný, and P. Michel. Debiased orbit and absolute-magnitude distributions for near-earth objects. *Icarus*, 312:181–207, Sept. 2018. doi: 10.1016/j.icarus.2018.04.018. URL https://doi.org/10.1016%2Fj.icarus.2018.04.018.

[60] ESA. Capturing the ripples of spacetime: LISA gets go-ahead. https://www.esa.int/Science_Exploration/Space_Science/Capturing_the_ripples_of_spacetime_LISA_gets_go-ahead. Accessed: 17 March 2024.

[61] C. R. Nugent, J. L. Margot, S. R. Chesley, and D. Vokrouhlický. Detection of Semimajor Axis Drifts in 54 Near-Earth Asteroids: New Measurements of the Yarkovsky Effect. *The Astronomical Journal*, 144(2):60, July 2012. ISSN 1538-3881. doi: 10.1088/0004-6256/144/2/60. URL http://dx.doi.org/10.1088/0004-6256/144/2/60.

[62] W. Martens and E. Joffre. Trajectory Design for the ESA LISA Mission. *The Journal of the Astronautical Sciences*, 68(2):402–443, June 2021. ISSN 2195-0571. doi: 10.1007/s40295-021-00263-2. URL http://dx.doi.org/10.1007/s40295-021-00263-2.

[63] P.-S. Laplace. *Traité de Mécanique Céleste*. Courcier, 1805. URL http://sites.mathdoc.fr/cgi-bin/oeitem?id=OE_LAPLACE__4_1_0.

[64] M. Vallisneri. Use and abuse of the Fisher information matrix in the assessment of gravitational-wave parameter-estimation prospects. *Physical Review D*, 77(4), Feb. 2008. ISSN 1550-2368. doi: 10.1103/physrevd.77.042001. URL http://dx.doi.org/10.1103/PhysRevD.77.042001.

[65] L. S. Finn. Detection, Measurement, and Gravitational Radiation. *Phys. Rev. D*, 46:5236–5249, Dec. 1992. doi: 10.1103/PhysRevD.46.5236. URL https://link.aps.org/doi/10.1103/PhysRevD.46.5236.

[66] C. Cutler and E. E. Flanagan. Gravitational Waves from Merging Compact Binaries: How accurately can one extract the Binary's parameters from the Inspiral Waveform? *Phys. Rev. D*, 49:2658–2697, Mar. 1994. doi: 10.1103/PhysRevD.49.2658. URL https://link.aps.org/doi/10.1103/PhysRevD.49.2658.

[67] T. Wiśniowski and H.Rickman. Fast geometric method for calculating accurate minimum orbit intersection distances. *Acta Astronomica*, 63:293–307, Mar. 2013. URL https://acta.astrouw.edu.pl/Vol63/n2/pdf/pap_63_2_10.pdf.

[68] A. M. Annex, B. Pearson, B. Seignovert, B. T. Carcich, H. Eichhorn, J. A. Mapel, J. L. F. von Forstner, J. McAuliffe, J. D. del Rio, K. L. Berry, K.-M. Aye, M. Stefko, M. de Val-Borro, S. Kulumani, and S. ya Murakami. SpiceyPy: a Pythonic Wrapper for the SPICE Toolkit. *Journal of Open Source Software*, 5(46):2050, Feb. 2020. doi: 10.21105/joss.02050. URL https://doi.org/10.21105/joss.02050.

[69] C. H. Acton. Ancillary data services of NASA's Navigation and Ancillary Information Facility. *Planetary and Space Science*, 44(1):65–70, Jan. 1996. ISSN 0032-0633. doi: 10.1016/0032-0633(95)00107-7. URL https://doi.org/10.1016/0032-0633(95)00107-7.

[70] C. Acton, N. Bachman, B. Semenov, and E. Wright. A look towards the future in the handling of space science mission geometry. *Planetary and Space Science*, 150:9–12, Jan. 2018. ISSN 0032-0633. doi: https://doi.org/10.1016/j.pss.2017.02.013. URL https://www.sciencedirect.com/science/article/pii/S0032063316303129.

[71] J.-B. Bayle, A. Hees, M. Lilley, and C. L. Poncin-Lafitte. LISA Orbits, Apr. 2022. URL https://doi.org/10.5281/zenodo.6412992.

[72] J.-B. Bayle, E. Castelli, and N. Korsakova. LISA Glitch, Apr. 2022. URL https://doi.org/10.5281/zenodo.6452904.

[73] J.-B. Bayle, O. Hartwig, and M. Staab. LISA Instrument, Aug. 2023. URL https://doi.org/10.5281/zenodo.8270606.

[74] J.-B. Bayle and O. Hartwig. Unified model for the lisa measurements and instrument simulations. *Physical Review D*, 107(8), Apr. 2023. ISSN 2470-0029. doi: 10.1103/physrevd.107.083019. URL http://dx.doi.org/10.1103/PhysRevD.107.083019.

[75] M. Staab, J.-B. Bayle, and O. Hartwig. PyTDI, 2023. URL https://zenodo.org/records/8429119.

[76] O. Hartwig, J.-B. Bayle, M. Staab, A. Hees, M. Lilley, and P. Wolf. Time-delay interferometry without clock synchronization. *Physical Review D*, 105(12), June 2022. ISSN 2470-0029. doi: 10.1103/physrevd.105.122008. URL http://dx.doi.org/10.1103/PhysRevD.105.122008.

[77] J.-B. Bayle. psd, Dec. 2020. URL https://pypi.org/project/psd/.

[78] V. K. Rohatgi and A. K. M. E. Saleh. *An Introduction to Probability and Statistics*. John Wiley & Sons, Aug. 2015. ISBN 9781118799635. doi: 10.1002/9781118799635. URL https://onlinelibrary.wiley.com/doi/book/10.1002/9781118799635.

[79] L. Amendola and E. Sellentin. Optimizing parameter constraints: a new tool for Fisher matrix forecasts. *Monthly Notices of the Royal Astronomical Society*, 457(2):1490–1495, Feb. 2016. ISSN 0035-8711. doi: 10.1093/mnras/stw072. URL https://doi.org/10.1093/mnras/stw072.

Appendix A

Code Implementation

Several individual *Python* packages were put together to be able to create the simulation of the close approach. These are:

- *MOID FORTRAN routine*: As the calculation of the MOID is a difficult 3D geometrical problem, the iterative method and FORTRAN routine provided in [67] are used. These were adapted and wrapped into *Python* so that the MOID could be calculated as well as the respective M for each body to find the respective points in the orbit which the bodies would have the minimum distance between them.

- *SpiceyPy package and SPICE toolkit*: are packages [68–70] providing access and tools to interact with planetary and spacecraft ephemeris and ancillary engineering information using *Python*. It was used to calculate the position of the bodies from their orbital elements in the heliocentric ecliptic coordinate system.

- *LISA Orbits package*: is a Python package [71] which was created to standardize the LISA orbits and generate orbit files which are compatible with other packages for the purpose of simulating the LISA constellation motion in orbit. It is used to store and assess the orbits and laser arms of the LISA constellation during the simulation.

- *LISA Glitch package*: is a Python package [72] capable of generating glitch[1] files which contain and store the induced velocity profiles for the different test masses and are compatible with the next package in the simulation pipeline. In this case, the glitch is the perturbation caused by the close approach of the NEA to the spacecraft, meaning that the glitch file stores the signal for the simulation.

- *LISA Instrument package*: *LISA Instrument* [73] is a Python package which implements of the simulation model described in [74]. It allows to run quick or partial simulations considering the

[1] A glitch is considered a perturbation in the laser beams.

instrumental effects and noises of of the full measurement and analysis chain of LISA's interferemeter. It allows to obtain the frequency shift profiles[2] of the signal in the LISA detectors.

- *PyTDI package*: is a Python package [75] based on the models presented in [76] that is capable of applying the TDI technique for the measurements obtained using *LISA Instrument*. It is used to compute the interferometric signal on the channels A, E and T during a close approach.
- *psd package*: is a Python package [77] that contains easy-to-use tools for quick data visualization and spectral analysis. It converts time-series signals to the frequency domain and allows to compute their PSD. It is used to convert the signal into the frequency domain and assess the SNR.

[2]While we would be expecting to see phase shifts in the results of the numerical simulations, frequency shifts are obtained instead. This is due to the fact that the frequency of the lasers used in LISA is too high and in the end, programmatically speaking, there would be a numerical overflow and loss of precision while calculating phase shift instead. Thus, the signals obtained from the interferometer are expressed as frequency shifts.

Appendix B

Computing the Mass Probability Density Function

We intend to find the mass probability density function. For that, we need to go back to the mass equation and study its components. The mass equation can be written as a function of each of the physical properties, density ρ, albedo p_υ and absolute magnitude H:

$$m = f(\rho)\, g(p_\upsilon)\, h(H) = \underbrace{\left(\frac{\pi}{6}\rho\right)}_{t}\underbrace{\left(a^3 p_\upsilon^{-\frac{3}{2}}\right)}_{z}\underbrace{\left(e^{-\frac{3\ln 10}{5}H}\right)}_{w}. \tag{B.1}$$

where $a = 1329$ km. Since the mass depends on these variables, it is only logical that its probability density function (pdf) will also depend on the corresponding pdfs.

To find the pdfs of t, z and w, the theorem of Transformation of a Univariate Random Variable can be used [78]. It states that for a strictly increasing or decreasing function $y = f(x)$, the pdf of y can be calculated from the pdf of x using the following formula:

$$p_y(y) = \pm\, p_x(f^{-1}(y))\frac{d}{dy}f^{-1}(y) \tag{B.2}$$

where the $+$ applies to the strictly positive and $-$ to the strictly decreasing function.

t is a strictly positive function for any $\rho > 0\,\mathrm{kg\,m^{-3}}$ which is our study case. On the other hand, z and w are strictly decreasing functions for the range of $p_\upsilon \in [0, 1]$ and $H \in [17,\, 25]$. So, we can derive the pdfs of t, z and w using Equation B.2.

$$\begin{aligned} p_t(t) &= \frac{6}{\pi}\, p_\rho\left(\frac{6}{\pi}t\right) \\ p_z(z) &= -\frac{2a^2}{3} z^{-\frac{5}{3}}\, p_{p_\upsilon}\left(\frac{a^2}{z^{\frac{2}{3}}}\right) \\ p_w(w) &= -\frac{5}{3w\ln 10}\, p_H\left(-\frac{5}{3}\frac{\ln w}{\ln 10}\right) \end{aligned} \tag{B.3}$$

For two independent and continuous random variables B, C with probability density functions p_B and p_C respectively, the pdf of $D = BC$ is given by [78]:

$$p_D(d) = \int p_B(b)\ p_C\left(\frac{d}{b}\right)\frac{1}{|b|}\,db \tag{B.4}$$

where d and b are instances of the random variables D and B.

Due to the lack of information in the matter, we consider that the the physical properties alebdo p_v, absolute magnitude H and density ρ are independent from each other. This assumption allows us to apply Equation B.4 twice to calculate the final pdf for the mass $p_m(m)$:

$$\begin{aligned} p_m(m) &= \iint p_t(t)\, p_z\left(\frac{\nu}{t}\right)\ p_w\left(\frac{m}{\nu}\right)\frac{1}{|t||\nu|}\,dt\,d\nu \\ &= \frac{20\,a^2}{3\pi\ln 10}\iint \frac{1}{\nu\, m}\left(\frac{t}{\nu}\right)^{\frac{2}{3}}\ p_\rho\left(\frac{6}{\pi}t\right)p_{p_v}\left(a^2\left(\frac{t}{\nu}\right)^{\frac{2}{3}}\right)p_H\left(-\frac{5}{3}\frac{\ln m - \ln\nu}{\ln 10}\right)\ dt\,d\nu \end{aligned} \tag{B.5}$$

where $\nu = zw$.

Equation B.5 allows to define a mass pdf depending on the pdfs of the physical properties p_H, p_ρ and p_{p_v} and can be used to integrate out the mass of the probability of detection in Chapter 3.3: Assessing the Probability of Detection of Asteroids.

Appendix C

Find Duration of a Simulation

When performing a simulation, it is very important to define an appropriate duration. The duration is a result of a compromise between capturing the essence of the signal but minimizing the computational time. If the simulation is too short it will impact the results found, yet if it is too long it will take to much time to be performed.

Because each asteroid has a distinct signal and characteristic time[1], it is not possible to define a fixed duration for all simulations. Thus, we defined a method to calculate it. Firstly, we calculate the acceleration profile for a long period of time, i.e, a month[2]. From that, we define the time interval in which 99% of the acceleration profile is contained and we use this time interval as the duration for the simulation, as illustrated in Figure C.1 for Asteroid 10603 of the fictitious population. In this example, 99% of the acceleration profile corresponds to a simulation of $113000\,\mathrm{s}$ and a signal like the one represented in Figure C.2 for channels A, E and T which contains all the features of the close approach.

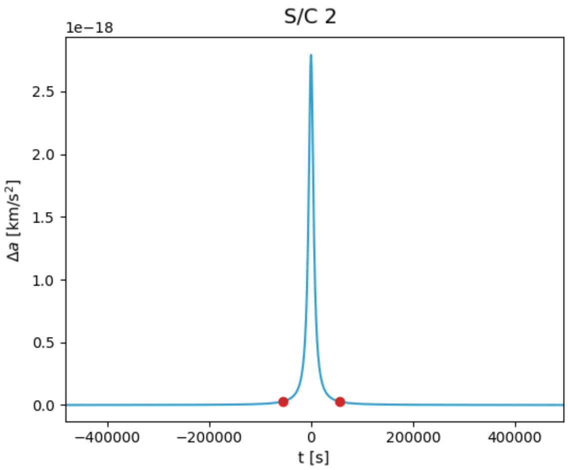

Figure C.1: Relative acceleration profile for Asteroid 10603 of the fictitious population for close approach with S/C 2. The red dots enclose the region containing 99% of the acceleration profile.

[1]The characteristic time corresponds to the time for the close approach. It is directly linked to the velocity that it has at and close to the MOID.

[2]A month is a good choice for the long duration as it is unrealistic to have close approaches lasting for one month to any of the spacecrafts. As a consequence, this duration allows to contain all the acceleration profile for the close approach.

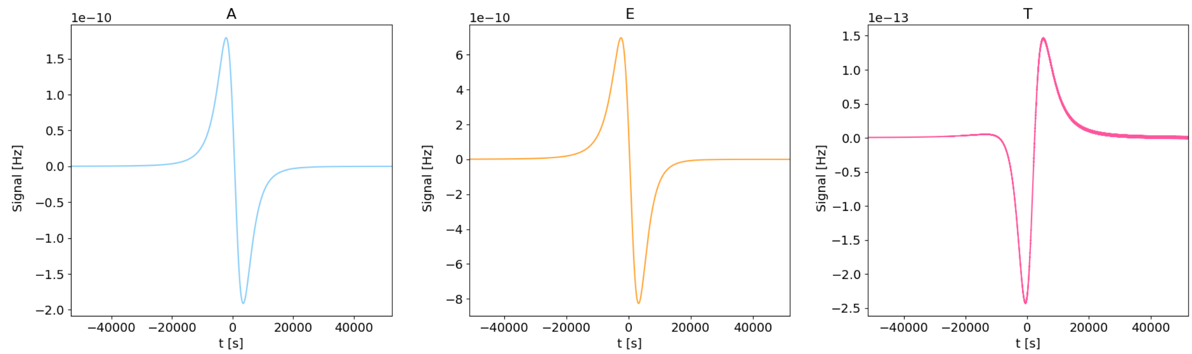

Figure C.2: Signal profile in TDI channels for Asteroid 10603 of fictitious population for close approach with S/C 2.

The value 99% was chosen as a compromise between containing the most signal possible and having a minimum duration allowing to decrease computational time. Several tests were performed with other values for the threshold for different asteroids and they can be seen in Figure C.3. Additionally, we can see the exponential behaviour of the simulation time as a function of the threshold for Asteroid 10603 in Figure C.4.

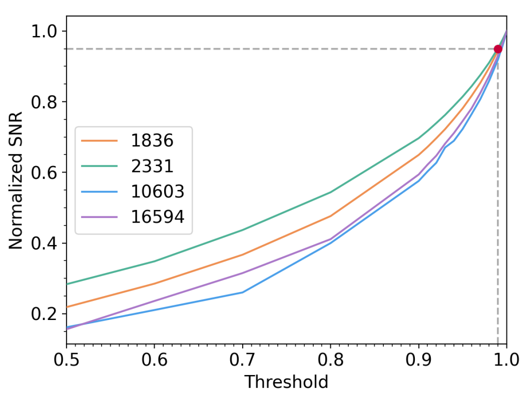

Figure C.3: Normalized SNR as a function of threshold for 4 asteroids. The normalized SNR corresponds to $\mathrm{SNR}_{\text{norm}} = \mathrm{SNR}_{\text{th}}/\mathrm{SNR}_{\text{max}}$ where SNR_{th} is the SNR at a given threshold and $\mathrm{SNR}_{\text{max}}$ is the value of SNR for a threshold of 99.999% of the acceleration profile. The dotted lines and red point refer to an Normalized SNR of 95% for a threshold of 99%.

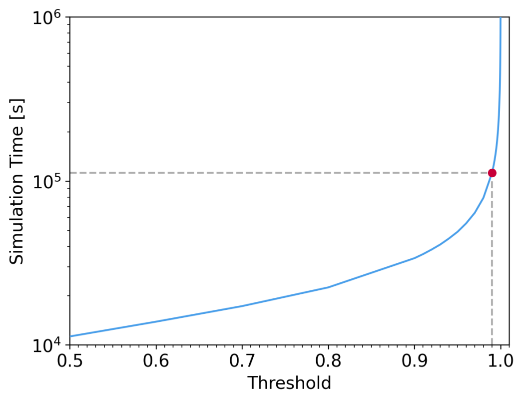

Figure C.4: Simulation time as a function of threshold for Asteroid 10603 of the fictitious population. The dotted lines and red point refer to a simulation time of $113000\,\mathrm{s}$ for a threshold of 99%.

Appendix D

Deviation from the Sphere of Influence

When analysing the results for the Probability of Detection study, we realized that for the scenario of a fixed orbit, the probability of detection was significantly underestimated. We recall such probabilities below.

$$P_{\text{det}(1)} = 7.31^{+33.74}_{-5.98} \times 10^{-5} \qquad P_{\text{det}(2)} = 5.78^{+26.30}_{-4.72} \times 10^{-5}$$

The only way these could have such an uncertainty is if the fit done to $p_{\text{det}}(m)$ was not correctly done. So, we decided to take a look at that. The found $p_{\text{det}}(m)$ curve is shown in Figure D.1.

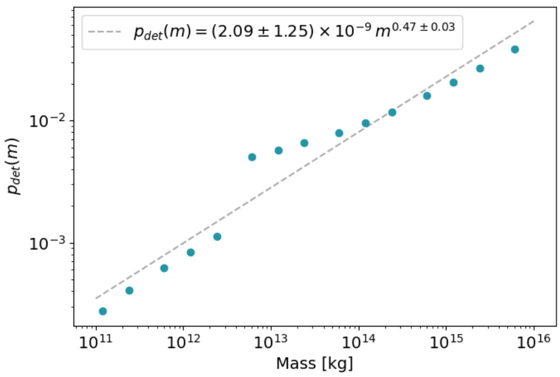

Figure D.1: Probability of detection as a function of mass for Asteroid 6135 of the fictitious population. Each point represents a value of $p_{\text{det}}(m)$ calculated for a certain mass m.

Evidently, this asteroid did not follow the expected linear trend, but rather had a jump on the probability of detection. To be able to understand where it came from, we backtracked the process and analysed the curves of δM_{NEA} and $\delta M_{\text{S/C}}$ as a function of the mass, shown in Figures D.2 and D.3. While the curve for the $\delta M_{\text{S/C}}$ seems perfectly coherent with the expected behaviour of a sphere of influence, we can see that the δM_{NEA} curve is far from it. There seems to be a jump around $m \in [2 \times 10^{12}, 5 \times 10^{12}]$ kg. Because the probability of detection is directly calculated using the δM, it inherits this behavior and thus has the jump in the same region.

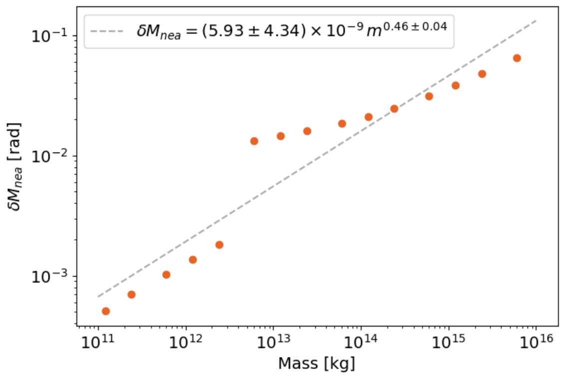

Figure D.2: δM_{NEA} as a function of mass for Asteroid 6135 of the fictitious population

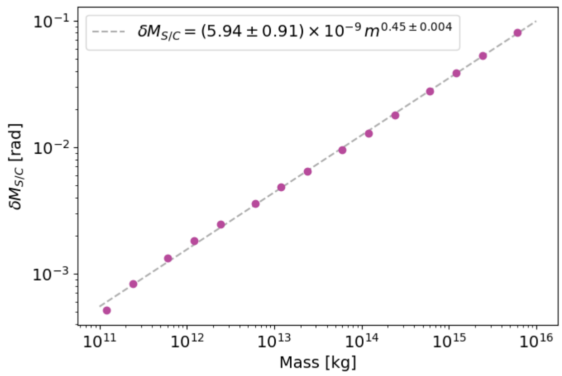

Figure D.3: $\delta M_{\text{S/C}}$ as a function of mass for Asteroid 6135 of the fictitious population

So, since the problem is for the δM_{NEA}, we examined more closely the phenomenom in the region of the jump, for $m = 2 \times 10^{12}$ kg and $m = 5 \times 10^{12}$ kg. The relative distance plot for each mass and corresponding delay allowing an SNR $= 5$, is shown in Figure D.4.

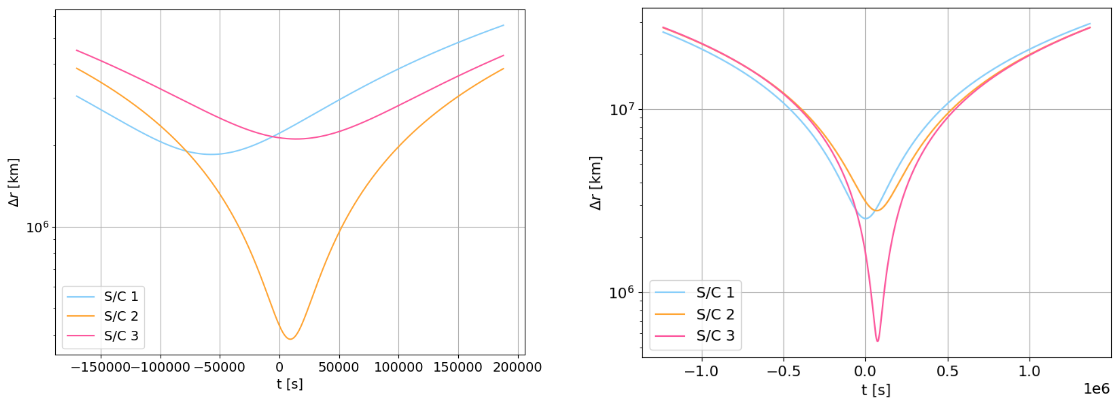

(a): $m = 2 \times 10^{12}$ kg
$\delta M_{\text{NEA}} = 0.0018$ rad

(b): $m = 5 \times 10^{12}$ kg
$\delta M_{\text{NEA}} = 0.013$ rad

Figure D.4: Magnitude of relative distance between S/C 2 and Asteroid 6135 of the fictitious population during delayed close approach for the two masses in the jump region and their respective delays.

These plot are enlightening. While the close approach was orchestrated with S/C 2 and it was still the close approach making the most contribution to the signal and SNR for $m = 2 \times 10^{12}$ kg, it was no longer true for $m = 5 \times 10^{12}$ kg. For the second case, the close approach was actually with S/C 3. This happened because, in the end, when we applied a $\delta M_{\text{NEA}} = 0.013$ rad, we got sufficiently delayed from S/C 2 that make the close approach be at a distance causing a close approach to another spacecraft. A delay of 0.013 rad can be on the order of millions of kilometers, which is precisely the inter-distance between spacecrafts. Due to the orbital geometry and the way the bodies move, this phenomenon appeared for a delay on the δM_{NEA} but it could as well have appeared on $\delta M_{\text{S/C}}$. It is just that for this asteroid, a delay in δM_{NEA} causes a motion of the asteroid in the direction of the constellation's motion. Additionally, we can see that already for $m = 2 \times 10^{12}$ kg, the distances for the close approaches with the different spacecraft are not so far apart. This means that there is also another contribution to the

SNR, multiple interactions with other spacecrafts for bigger masses. The relative distances for the three spacecraft are less than a factor 10 away from each other, which means that if we are already detectable by S/C 2 at this distance, if the mass is increases slightly, the other spacecraft will also be able to detect it and contribute to the probability of detection. This was confirmed when we analysed the relative acceleration, displayed in Figure D.5.

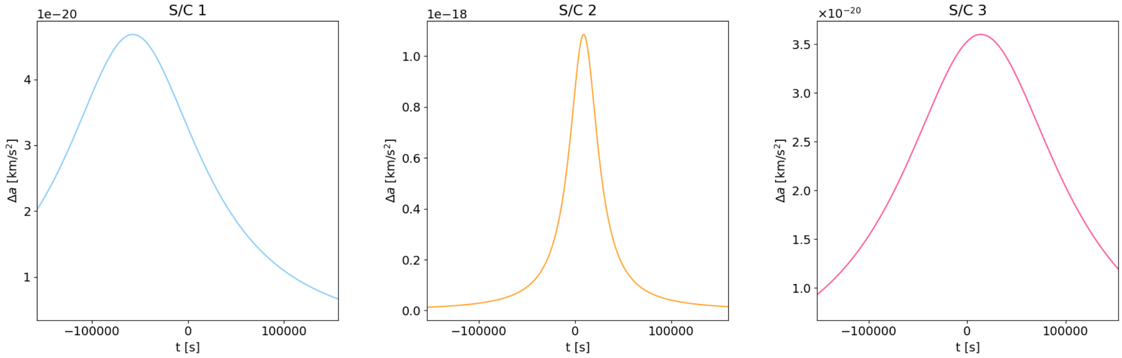

(a): $m = 2 \times 10^{12}$ kg and $\delta M_{\text{NEA}} = 0.0018$ rad

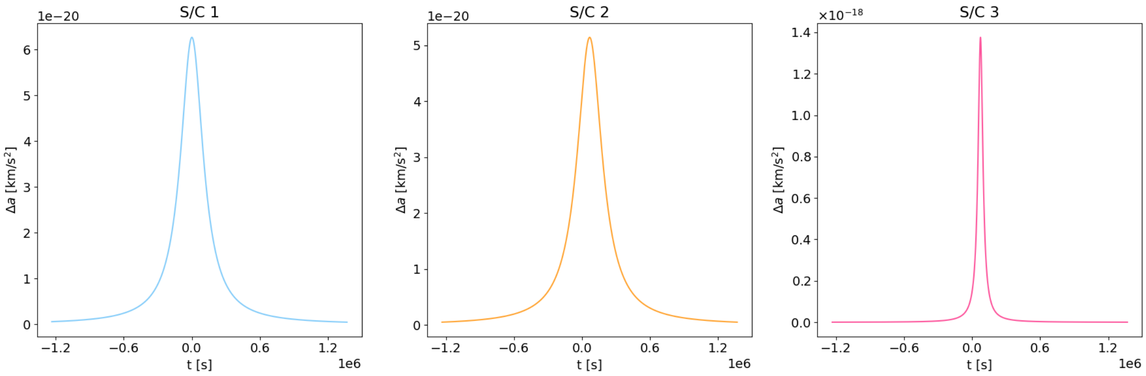

(b): $m = 5 \times 10^{12}$ kg and $\delta M_{\text{NEA}} = 0.013$ rad

Figure D.5: Magnitude of relative acceleration between S/C 2 and Asteroid 6135 of the fictitious population during delayed close approach for the two masses in the jump region and their respective delays.

If we observe these curves, we see that there is a strong close approach to S/C 2 for $m = 2 \times 10^{12}$ kg but yet there are some small close approaches to S/C 1 slightly earlier and S/C 3 slightly later in time. These accelerations are already above the expected signal for just one close approach, so they end up contributing to the SNR. The acceleration for $m = 5 \times 10^{12}$ kg shows that the strongest close approach is for S/C 3 and contributions of the other spacecraft.

We can draw a curve of SNR as a function of δM_{NEA} to understand the extent of this phenomenon for this asteroid. Such curve is displayed in Figure D.6. If the detection was linked to just one sphere of influence as we hypothesized while doing the linear fit to $p_{\text{det}}(m)$, we would expect just an exponential decay on the SNR. Nevertheless, for a sufficiently heavy asteroid and the right orbital configuration, we can see that that is no longer the case, and we have bumps arising from the interactions with the other spacecraft, more favourable at certain delays than others. In some cases, for sufficiently large masses, the bumps rise above the minimum threshold of 5 and end up contributing for the detection.

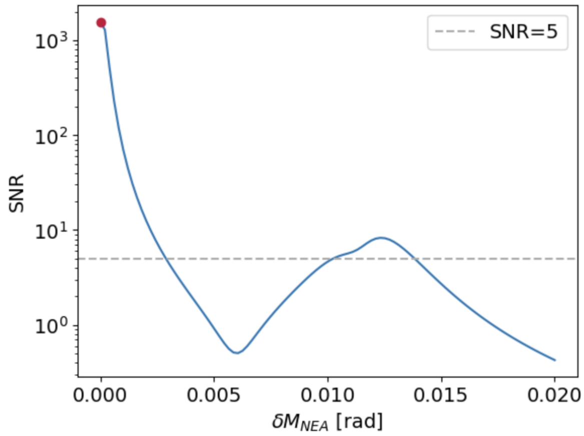

Figure D.6: SNR vs δM_{NEA} for Asteroid 6135 of the fictitious population with a mass of $m = 8 \times 10^{12}$ kg. The red dot corresponds to the MOID.

In the end, all asteroids are bound to experience from this effect. If we increase sufficiently the mass of an asteroid, it will cause the expansion of sphere of influence. But in this case, as we have more than one body, we will end up expanding three spheres which can at some point intercept the orbit and we end having multiple interactions as illustrated in Figure D.7. For some asteroids, it is a phenomenon, we will never see since it will happen for absurd masses. This is predicted by the first study (Figure 3.2). While for others such as Asteroid 6135, the orbit and close approaches are favourable in such a way that it can be seen even at reasonable masses (also visible in Figure 3.2).

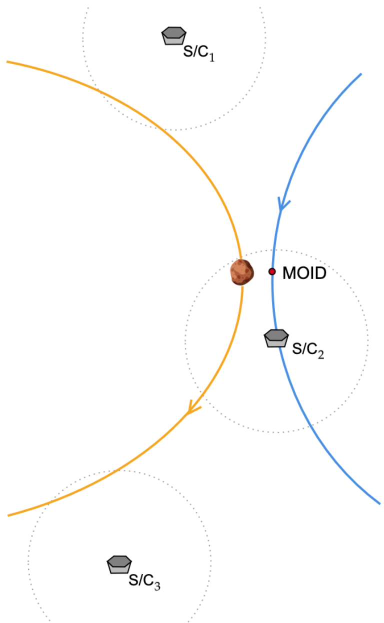

Figure D.7: Illustration of delayed close approach to S/C 2 with the spheres of influence of each S/C intercepting the orbit of the NEA. The sphere of influence for each S/C is delineated by the dotted gray line. Not to Scale.

Appendix E

Adding Fisher Matrices

Ideally, since there are three TDI channels collecting a signal in the LISA mission, it would be best to join the information contained by all of them for a better parameter resolution. To verify if this is possible, Bayes' Theorem (Equation 3.16) is used once again.

Assuming that there are two measurements that result in parameter distributions with Fisher matrices $\boldsymbol{F_1}$ and $\boldsymbol{F_2}$, it is possible to calculate the new posterior probability for the two measurements using the likelihood. We are still under the assumption that the parameters measurement probability distribution is a (multinormal) Gaussian distribution as before. That being said, we have:

$$\begin{aligned} P(\boldsymbol{\theta} \,|\, \boldsymbol{F_1},\, \boldsymbol{F_2}) &\propto e^{-\frac{1}{2}\boldsymbol{\theta}^T \boldsymbol{F_1} \boldsymbol{\theta}} \times e^{-\frac{1}{2}\boldsymbol{\theta}^T \boldsymbol{F_2} \boldsymbol{\theta}}, \\ &\propto e^{-\frac{1}{2}\boldsymbol{\theta}^T (\boldsymbol{F_1}+\boldsymbol{F_2}) \boldsymbol{\theta}}. \end{aligned} \tag{E.1}$$

Bayes' Theorem allows us to add directly the likelihoods of the two measurements. This means that adding Fisher matrices together is possible. Yet, it is not evident from Bayes' Theorem that by adding the Fisher matrices together, the uncertainty on the measurements will decrease. In other words, it is not clear that the information from the two measurements will complement each other and end up resulting in lower uncertainties or covariances.

In a standard one-dimensional case, it is trivial to show that two measurements (with associated fisher matrices F_1 and F_2 and variances σ_1 and σ_2) of the same quantity provide more information about this quantity, and make the uncertainty decrease.

$$\sigma_2^2 < \sigma_1^2 + \sigma_2^2 \;\Rightarrow\; \frac{\sigma_2^2}{\sigma_1^2+\sigma_2^2} < 1 \;\Rightarrow\; \underbrace{\frac{\sigma_1^2\sigma_2^2}{\sigma_1^2+\sigma_2^2}}_{(F_1+F_2)^{-1}} < \sigma_1^2. \tag{E.2}$$

Nevertheless, for a multidimensional case, we need to look at the error volume, quantified by the diagonal of the Covariance matrix $\boldsymbol{C} = (\boldsymbol{F_1} + \boldsymbol{F_2})^{-1}$ for both measurements, corresponding to the generalisation of the one-dimensional uncertainty. For this proof, we base ourselves in the work in [79].

Knowing that the Fisher Matrix $\boldsymbol{F_1}$ is symmetric, we can easily diagonalize it:

$$\boldsymbol{F_1^d} = \boldsymbol{R}\boldsymbol{F_1}\boldsymbol{R}^T. \tag{E.3}$$

where X is a suitable rotation matrix with the properties $\boldsymbol{R}\boldsymbol{R}^T = 1$ and $\det \boldsymbol{R} = 1$ and $\boldsymbol{F_1^d}$ is the resulting diagonal matrix.

Any diagonal matrix can be written as sum of the outer products of two vectors $\boldsymbol{v}_k$ and $\boldsymbol{v}_k^T$, consisting on the "square root" of the column vectors.

$$\boldsymbol{F_1^d} = \sum_{k=1}^{n} \boldsymbol{v}_k\, \boldsymbol{v}_k^T, \qquad \boldsymbol{v}_k = \frac{1}{\sqrt{\left\|\mathrm{col}(\boldsymbol{F_1^d},\, k)\right\|}}\,\mathrm{col}(\boldsymbol{F_1^d},\, k). \tag{E.4}$$

Defining $\boldsymbol{u}_k = \boldsymbol{R}^T\boldsymbol{v}_k$, it is possible to rewrite $\boldsymbol{F_1}$ as:

$$\boldsymbol{F_1} = \sum_{k=1}^{n} \boldsymbol{R}^T\boldsymbol{v}_k\, \boldsymbol{v}_k^T, \boldsymbol{R} = \sum_{k=1}^{n} \boldsymbol{u}_k\boldsymbol{u}_k^T. \tag{E.5}$$

Now, the Sherman–Morrison–Woodbury formula [79] can be used. It states that for a square matrix $\boldsymbol{M}$ and two vectors $\boldsymbol{b}$ and $\boldsymbol{c}$ are:

$$(\boldsymbol{M} + \boldsymbol{b}\boldsymbol{c}^T)^{-1} = \boldsymbol{M}^{-1} - \frac{\boldsymbol{M}^{-1}\boldsymbol{b}\boldsymbol{c}^T\boldsymbol{M}^{-1}}{1 + \boldsymbol{c}^T\boldsymbol{M}^{-1}\boldsymbol{b}}. \tag{E.6}$$

$\boldsymbol{M}$ and the vectors $\boldsymbol{b}$ and $\boldsymbol{c}$ can be defined using the variables in our problem:

$$\begin{aligned} \boldsymbol{M} &= \sum_{k=1}^{n-1} \boldsymbol{u}_k\boldsymbol{u}_k^T + \boldsymbol{C_2}^{-1}, \\ \boldsymbol{b} &= \boldsymbol{c} = \boldsymbol{u}_n. \end{aligned} \tag{E.7}$$

Replacing $\boldsymbol{M}$, $\boldsymbol{b}$ and $\boldsymbol{c}$ in Equation E.6, the total covariance $\boldsymbol{C}$ is:

$$\boldsymbol{C} = (\boldsymbol{M} + \boldsymbol{u}_n\boldsymbol{u}_n^T)^{-1} = \boldsymbol{M}^{-1} - \frac{\boldsymbol{M}^{-1}\boldsymbol{u}_n\boldsymbol{u}_n^T\boldsymbol{M}^{-1}}{1 + \boldsymbol{u}_n^T\boldsymbol{M}^{-1}\boldsymbol{u}_n}. \tag{E.8}$$

Now the diagonal of $\boldsymbol{C}$ corresponds to the variance of the parameters. The variance, then, corresponds to:

$$\begin{aligned} \mathrm{diag}\,\boldsymbol{C} &= \mathrm{diag}\,\boldsymbol{M}^{-1} - \frac{\mathrm{diag}\,(\boldsymbol{M}^{-1}\boldsymbol{u}_n\boldsymbol{u}_n^T\boldsymbol{M}^{-1})}{1 + \boldsymbol{u}_n^T\boldsymbol{M}^{-1}\boldsymbol{u}_n}, \\ &= \mathrm{diag}\,\boldsymbol{M}^{-1} - \frac{\mathrm{diag}\,(\boldsymbol{M}^{-1}\boldsymbol{u}_n(\boldsymbol{M}^{-1}\boldsymbol{u}_n)^T)}{1 + \boldsymbol{u}_n^T\boldsymbol{M}^{-1}\boldsymbol{u}_n}. \end{aligned} \tag{E.9}$$

As $\boldsymbol{M}$ is a symmetric definite positive matrix due to its definition, and that the denominator is larger than 1, we can conclude that:

$$\mathrm{diag}\,\boldsymbol{C} < \mathrm{diag}\,\boldsymbol{M}^{-1} = \mathrm{diag}\,\left(\left(\sum_{k=1}^{n-1} \boldsymbol{u}_k\boldsymbol{u}_k^T + \boldsymbol{C_2}^{-1}\right)^{-1}\right). \tag{E.10}$$

Iterating the previous formula for n steps, we end up with the following result:

$$\operatorname{diag} \boldsymbol{C} < \operatorname{diag} \boldsymbol{C_2}. \tag{E.11}$$

$\boldsymbol{C}$ is smaller than the covariance of the individual measurement covariance $\boldsymbol{C}_2$. If the definition of $\boldsymbol{M}$ was changed to include $\boldsymbol{C}_1$, then we would obtain the same result for the other individual measurement covariance. Therefore, this proves that the covariance decreases when we add two Fisher matrices together.

Concluding, it means that it is possible to add the Fisher matrices of the three TDI channels to obtain a better resolution on the parameters to be tested, given by the lower covariance. A final Fisher Matrix $\boldsymbol{F}$ can be computed and inverted to obtain the final Covariance Matrix $\boldsymbol{C}$ and further on, the final Correlation Matrix $\boldsymbol{X}$ for the LISA detection:

$$\begin{gathered} \boldsymbol{F} = \boldsymbol{C_A^{-1}} + \boldsymbol{C_E^{-1}} + \boldsymbol{C_T^{-1}}, \\ \boldsymbol{C} = \boldsymbol{F^{-1}}. \end{gathered} \tag{E.12}$$

Appendix F

Tables and Extra Results

F.1 LISA Constellation

F.1.1 Spacecraft Orbital Elements

The orbital elements for the three S/C of LISA used in all the simulations performed are presented in Table F.1.

	a [au]	e	i [rad]	Ω [rad]	ω [rad]	M [rad]
S/C_1	0.999006	0.004821	0.008293	0.132958	1.560585	4.661102
S/C_2	0.998994	0.004824	0.008407	2.230733	1.557594	2.566136
S/C_3	0.998991	0.004821	0.008372	4.311799	1.571140	0.471570

Table F.1: Orbital elements for LISA constellation

F.1.2 Galactic Foreground Noise

The total sensitivity curve is obtained by adding the contribution coming from the galactic foreground, S_c, described in [53]:

$$S_c(f) = Af^{-7/3}e^{-f^{\alpha}+\beta f \sin(\kappa f)}\left[1+\tanh(\gamma(f_k - f)\right]\ \mathrm{Hz}^{-1} \tag{F.1}$$

where the fit parameters in this equation can be found in Table F.2.

Time [yr]	α	β	κ	γ	f_k
0.5	0.133	243	482	917	0.00258
1	0.171	292	1020	1680	0.00215
2	0.165	299	611	1340	0.00173
4	0.138	221	521	1680	0.00113

Table F.2: Parameters of the analytic fit the galactic foreground noise, S_c according to [53]. The amplitude A has been fixed to 9×10^{-45}. The frequency, f_k, decreases with observation time and γ increases with observation time, leading to a decrease of the galactic background noise over time which makes valid our simplification. The other parameters vary as a function of time.

F.2 Observed NEA Population

F.2.1 Asteroid Taxonomy

Some of the classes of asteroid taxonomy allowing to identify an average albedo and an expected composition are shown in Table F.1.

Class	Spectrum	Albedo	Prototypes
A	Broad and deep absorption feature at 1 µm, strong red slope in the near-infrared.	$0.25^{+0.09}_{-0.07}$	(246) *Asporina*, (289) *Nenetta*, (354) *Eleonora*
B	Neutral to blue slope in the visible, blue slope in the near-infrared.	$0.06^{+0.05}_{-0.03}$	(2) *Pallas*, (531) *Zerlina*, (3200) *Phaethon*
C	Red visible slope with a possible broad feature around 1 µm and a red near-infrared slope. The spectrum might have an overall concave shape.	$0.05^{+0.02}_{-0.01}$	(1) *Ceres*, (10) *Hygiea*, (24) *Themis*
Ch	Absorption feature at 0.7 µm. The near-infrared slope is red while the overall shape might be convex.	$0.05^{+0.02}_{-0.01}$	(13) *Egeria*, (19) *Fortuna*, (41) *Daphne*
D	Featureless with steep red slope with a possible convex shape longwards of 1.5 µm.	$0.06^{+0.03}_{-0.02}$	(588) *Achilles*, (911) *Agamem.*, (1143) *Odysseus*
E	Strong red slope in the visible with a feature around 0.9 µm of varying depth and a neutral near-infrared continuation.	$0.57^{+0.15}_{-0.12}$	(64) *Angelina*, (214) *Aschera*, (434) *Hungaria*
K	Strong red slope in the visible with a broad feature around 1 µm followed by a blue to neutral near-infrared slope.	$0.13^{+0.04}_{-0.03}$	(221) *Eos*, (579) *Sidonia*, (653) *Berenike*
L	Variable appearance apart from a red visible slope. A small feature around 1 µm and a possible one at 2 µm. The near-infrared slope is blue or red.	$0.18^{+0.07}_{-0.05}$	(234) *Barbara*, (397) *Vienna*, (599) *Luisa*
M	Linear red slope with possible faint features around 0.9 µm and 1.9 µm. Might show convex shape in the near-infrared.	$0.14^{+0.05}_{-0.04}$	(16) *Psyche*, (22) *Kalliope*, (216) *Kleopatra*
O	Broad, bowl-shaped 1 µm absorption feature and a weaker feature at 2 µm.	$0.26^{+0.02}_{-0.02}$	(3628) *Boznem.*, (7472) *Kumakiri*
P	Linear red slope and generally featureless. Less red than D-types.	$0.05^{+0.02}_{-0.01}$	(65) *Cybele*, (87) *Sylvia*, (153) *Hilda*
Q	Broad absorption at 1 µm and a shallow feature at 2 µm. An overall blue slope in the near-infrared.	$0.24^{+0.12}_{-0.08}$	(1862) *Apollo*, (1864) *Daedalus*, (5143) *Heracles*
R	Strong feature at 1 µm and a feature at 2 µm. The latter feature is shallower than in V-types.	$0.30^{+0.05}_{-0.04}$	(349) *Dembow.*, (5379) *Abehiro.*, (137062) *1998 WM*
S	Moderate features around 1 µm and 2 µm and a neutral to red near-infrared slope.	$0.24^{+0.10}_{-0.07}$	(3) *Juno*, (5) *Astraea*, (14) *Irene*
V	Deep absorption features at 1 µm and 2 µm. The former is much narrower than the latter.	$0.29^{+0.11}_{-0.08}$	(4) *Vesta*, (1929) *Kollaa*, (4215) *Kamo*
Z	Extremely red slope, redder than the D-types. Featureless but may exhibit concave shape in the near-infrared.	$0.07^{+0.04}_{-0.03}$	(203) *Pompeja*, (269) *Justitia*, (908) *Buda*

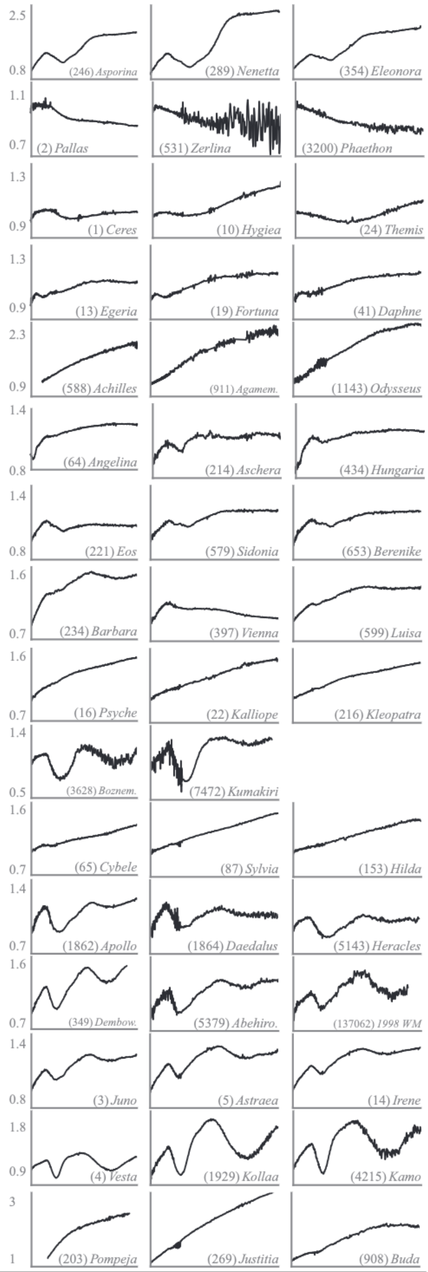

Figure F.1: Description of taxonomic classes for asteroids [43]. The spectral appearance, visual albedo mean value as well as its lower and upper standard deviation, and the spectral prototypes of the 17 classes from observations are shown in this Table. Note that this list excludes the X class. The plots of asteroid spectra on the right display the reflectance in the y-axis and the wavelenght / µm on the x-axis.

F.2.2 Orbital Elements and Physical Properties

In Table F.3, the collected orbital elements and physical properties for some of the observed NEAs using the traditional detection methods based on observations are shown.

Name	a [au]	e	i [rad]	Ω [rad]	ω [rad]	M [rad]	H	p_v	d [m]
1981 Midas	1.78	0.65	0.69	6.23	4.67	3.06	15.26	0.29	1900
2201 Oljato	2.17	0.71	0.04	1.31	1.71	4.77	15.36	0.24	2100
4179 Toutatis	2.54	0.62	0.01	2.19	4.85	5.08	15.30	0.41	2640
5693	1.27	0.59	0.09	1.69	4.52	1.14	16.87	-	1400
13651	1.34	0.31	0.30	2.04	2.34	2.36	17.85	0.51	560
16960	2.20	0.86	0.31	4.54	4.25	4.33	14.03	0.23	4100
69230 Hermes	1.65	0.62	0.11	0.59	1.62	3.26	17.62	0.27	820
85713	1.92	0.64	0.19	0.71	1.80	2.89	15.46	0.08	3484
90416	1.69	0.49	0.14	5.70	4.07	0.48	18.78	0.07	900
143649	1.09	0.19	1.08	0.02	1.83	6.28	17.37	*	*
154276	1.70	0.69	0.15	0.59	1.74	3.48	17.67	0.14	1060
162567	1.25	0.25	0.24	5.82	2.33	4.03	19.97	0.17	330
179806	1.86	0.53	0.09	5.86	2.20	2.49	20.43	*	*
221455	2.02	0.66	0.02	0.37	4.08	1.29	19.51	*	*
242643	1.83	0.87	0.15	0.68	0.85	2.76	17.38	0.092	1430
252399	0.87	0.55	0.27	1.01	2.37	0.38	19.5	0.68	260
357028	1.38	0.61	0.16	0.18	4.99	3.95	19.46	*	*
387668	1.30	0.43	0.40	6.05	4.83	4.35	20.42	*	*
415745	1.75	0.46	0.18	1.20	3.77	1.90	19.34	0.19	502
453729	1.38	0.28	0.36	1.60	3.12	4.86	18.82	*	*
509821	1.73	0.61	0.02	5.54	4.00	3.88	20.17	*	*
523820	2.24	0.60	0.96	0.30	5.57	4.34	18.26	0.02	2660
620100	1.34	0.50	0.05	1.43	1.53	3.81	21.32	*	*
2001YB5	2.34	0.86	0.10	1.89	2.01	1.03	20.65	*	*
2002NY40	2.05	0.71	0.10	2.54	4.71	2.02	19.34	0.34	280
2003UQ12	1.71	0.53	0.09	0.55	5.09	1.14	25.23	*	*
2004MC	2.43	0.59	0.04	1.59	3.56	1.04	23.35	*	*
2005YR3	0.82	0.27	0.06	1.31	3.80	0.28	23.56	*	*
2007VD12	1.15	0.36	0.40	1.09	1.59	1.17	19.88	0.39	220
2008VZ3	1.85	0.53	0.06	3.99	4.15	0.27	24.50	*	*

Table F.3: Orbital elements and physical properties of 30 asteroids. Data obtained from NEOCC database: `https://neo.ssa.esa.int/` for epoch 60400 mjd. * : data is estimated using the standard interval for the albedo $p_v = [0.05, 0.25]$ and derived using Equation 2.5. - : information is not available.

F.2.3 Uncertainties in Observed Orbital Elements

In Table F.4, the collected uncertainties for some of the observed NEAs using the traditional detection methods based on observations are shown.

Name	σ_a [au]	σ_e	σ_i [rad]	σ_Ω [rad]	σ_ω [rad]
1981 Midas	2.57×10^{-9}	2.09×10^{-8}	9.80×10^{-8}	2.80×10^{-8}	8.03×10^{-8}
2201 Oljato	8.13×10^{-9}	2.80×10^{-8}	5.44×10^{-8}	1.74×10^{-6}	1.74×10^{-6}
4179 Toutatis	4.29×10^{-10}	1.29×10^{-9}	2.83×10^{-9}	3.53×10^{-7}	3.44×10^{-7}
5693	1.70×10^{-9}	2.22×10^{-8}	3.65×10^{-8}	4.31×10^{-7}	4.23×10^{-7}
13651	7.54×10^{-10}	2.66×10^{-8}	8.03×10^{-8}	1.60×10^{-7}	2.00×10^{-7}
16960	3.89×10^{-9}	1.93×10^{-8}	4.97×10^{-8}	3.03×10^{-7}	2.86×10^{-7}
69230 Hermes	1.79×10^{-9}	1.01×10^{-8}	6.08×10^{-8}	1.48×10^{-7}	1.46×10^{-7}
85713	7.43×10^{-10}	1.92×10^{-8}	6.12×10^{-8}	1.92×10^{-7}	1.97×10^{-7}
90416	1.00×10^{-9}	1.65×10^{-8}	8.57×10^{-8}	1.90×10^{-7}	2.13×10^{-7}
143649	1.15×10^{-9}	2.72×10^{-8}	2.42×10^{-7}	3.38×10^{-8}	1.72×10^{-7}
154276	6.94×10^{-9}	1.35×10^{-8}	7.15×10^{-8}	1.83×10^{-7}	1.89×10^{-7}
162567	1.77×10^{-9}	4.39×10^{-8}	1.65×10^{-7}	2.93×10^{-7}	3.61×10^{-7}
179806	1.77×10^{-9}	4.39×10^{-8}	1.65×10^{-7}	2.93×10^{-7}	3.61×10^{-7}
221455	2.39×10^{-8}	4.49×10^{-8}	1.68×10^{-7}	3.10×10^{-7}	3.68×10^{-7}
242643	1.60×10^{-9}	1.39×10^{-8}	1.12×10^{-7}	2.11×10^{-7}	2.18×10^{-7}
252399	1.45×10^{-9}	8.55×10^{-8}	1.26×10^{-7}	2.41×10^{-7}	2.46×10^{-7}
357028	3.34×10^{-9}	7.36×10^{-8}	1.46×10^{-7}	8.81×10^{-7}	8.65×10^{-7}
387668	5.72×10^{-9}	8.45×10^{-8}	3.17×10^{-7}	1.93×10^{-7}	2.33×10^{-7}
415745	1.66×10^{-9}	3.42×10^{-8}	1.06×10^{-7}	5.73×10^{-7}	5.60×10^{-7}
453729	3.97×10^{-9}	3.34×10^{-8}	7.87×10^{-8}	1.83×10^{-7}	2.74×10^{-7}
509821	1.83×10^{-9}	4.86×10^{-8}	1.59×10^{-7}	1.00×10^{-5}	1.00×10^{-5}
523820	2.62×10^{-8}	1.28×10^{-7}	6.51×10^{-7}	1.93×10^{-7}	3.93×10^{-7}
620100	2.93×10^{-9}	2.38×10^{-8}	5.64×10^{-8}	3.17×10^{-7}	3.21×10^{-7}
2001YB5	2.53×10^{-3}	4.39×10^{-4}	1.40×10^{-4}	1.21×10^{-3}	1.27×10^{-3}
2002NY40	5.38×10^{-8}	5.19×10^{-8}	1.26×10^{-7}	7.22×10^{-8}	2.39×10^{-7}
2003UQ12	4.25×10^{-3}	1.49×10^{-3}	3.7×10^{-4}	7.90×10^{-4}	8.80×10^{-4}
2004MC	1.37×10^{-3}	1.13×10^{-3}	4.49×10^{-6}	6.00×10^{-5}	2.30×10^{-4}
2005YR3	4.00×10^{-6}	1.00×10^{-6}	1.19×10^{-6}	2.00×10^{-5}	1.00×10^{-5}
2007VD12	2.26×10^{-9}	2.08×10^{-7}	2.75×10^{-7}	5.89×10^{-8}	4.75×10^{-7}
2008VZ3	2.40×10^{-3}	6.22×10^{-4}	1.30×10^{-4}	1.34×10^{-3}	1.43×10^{-3}

Table F.4: Standard deviation for orbital elements and physical properties of 30 asteroids. Data obtained from NEOCC database: `https://neo.ssa.esa.int/` for epoch 60400 mjd.

F.2.4 Variation in SNR for different LISA Geometry

In Table F.5, the results for the first study allowing to decide if the asteroid is a good candidate for detection for some of the observed NEAs using the traditional detection methods based on observations are shown.

Name	m [kg]	MOID [au]	$\mathrm{SNR}_{\mathrm{min}}$	$\mathrm{SNR}_{\mathrm{original}}$	$\mathrm{SNR}_{\mathrm{max}}$
1981 Midas	4.53×10^{13}	3.28×10^{-3}	15.29	27.61	87.89
2201 Oljato	6.72×10^{12}	3.08×10^{-3}	2.94	3.42	14.90
4179 Toutatis	1.81×10^{14}	3.79×10^{-4}	25183.59	27746.48	63314.80
5693	4.35×10^{12}	9.00×10^{-4}	22.22	123.53	221.87
13651	2.04×10^{11}	4.00×10^{-4}	4.95	23.43	49.20
16960	1.15×10^{14}	7.22×10^{-3}	6.44	19.40	34.20
69230 Hermes	1.27×10^{12}	2.66×10^{-4}	222.76	372.07	841.95
85713	4.87×10^{13}	1.42×10^{-3}	132.64	201.68	714.94
90416	1.04×10^{12}	2.50×10^{-4}	291.47	291.48	808.40
143649	1.90×10^{12}	1.77×10^{-4}	121.39	1575.91	2533.25
154276	1.37×10^{12}	4.97×10^{-4}	48.44	99.75	234.47
162567	4.33×10^{10}	2.00×10^{-4}	6.15	28.92	41.03
179806	2.73×10^{10}	9.82×10^{-5}	56.83	84.71	116.08
221455	1.00×10^{11}	1.43×10^{-4}	113.65	179.01	249.97
242643	9.06×10^{12}	1.30×10^{-3}	27.75	127.54	173.33
252399	2.84×10^{10}	3.05×10^{-4}	1.11	9.24	13.41
357028	1.09×10^{11}	3.77×10^{-4}	6.62	22.47	39.74
387668	2.55×10^{10}	2.66×10^{-5}	746.85	794.08	846.99
415745	1.28×10^{11}	4.16×10^{-4}	12.89	17.71	39.47
453729	2.56×10^{11}	2.20×10^{-4}	49.08	95.10	232.03
509821	3.92×10^{10}	2.32×10^{-4}	12.80	28.71	39.48
523820	6.21×10^{11}	8.53×10^{-4}	5.92	17.54	31.33
620100	7.99×10^{9}	4.61×10^{-5}	63.32	70.97	111.39
2001YB5	1.86×10^{10}	1.21×10^{-5}	1338.00	1989.04	2110.60
2002NY40	2.05×10^{11}	7.69×10^{-5}	737.40	798.75	1303.45
2003UQ12	5.93×10^{7}	8.04×10^{-6}	9.94	20.77	21.39
2004MC	4.91×10^{8}	2.57×10^{-5}	22.58	39.89	40.10
2005YR3	3.03×10^{8}	5.71×10^{-6}	93.06	363.51	388.10
2007VD12	6.01×10^{10}	2.36×10^{-4}	2.87	31.14	44.50
2008VZ3	1.18×10^{8}	1.43×10^{-6}	118.05	600.75	941.92

Table F.5: Variation of SNR due to LISA geometry for 30 asteroids of the observed NEA population. Note that to calculate the mass of these asteroids, Equation 2.6 was used. Due to lack of measurements, a density of $2200\ \mathrm{kg/m^3}$ was assumed, and whenever the diameter and/or albedo was not available, Equation 2.5 and the standard albedo of $p_v = 0.14$ were used.

F.3 Fictitious NEA Population

F.3.1 Orbital Elements and Physical Properties

In Table F.6, the collected orbital elements and physical properties for some of the fictitious NEAs created with NEOPOP are shown.

Name	a [au]	e	i [rad]	Ω [rad]	ω [rad]	M [rad]	H	d [m]	m_0 [kg]	MOID [au]
1279	1.89	0.81	0.04	3.68	2.24	1.05	18.24	798.84	5.87×10^{11}	2.31×10^{-4}
1836	1.79	0.53	0.15	1.14	2.09	6.14	17.1	1350.40	2.84×10^{12}	4.61×10^{-5}
2331	1.45	0.31	0.23	0.10	3.17	0.14	17.51	1118.05	1.61×10^{12}	1.62×10^{-4}
2474	2.46	0.71	0.61	5.69	1.23	2.94	17.04	1388.23	3.08×10^{12}	4.42×10^{-4}
3112	1.94	0.50	0.19	5.73	2.73	2.19	18.84	605.98	2.56×10^{11}	1.50×10^{-4}
4368	2.26	0.62	0.23	3.24	5.46	1.08	16.4	1864.06	7.46×10^{12}	9.72×10^{-4}
4644	2.23	0.65	0.16	0.0025	4.17	5.52	19.31	488.05	1.34×10^{11}	1.22×10^{-5}
5401	3.39	0.72	0.43	3.53	5.92	1.55	18.21	809.96	6.12×10^{11}	1.79×10^{-4}
6135	1.27	0.64	0.16	4.56	2.01	1.82	17.72	1014.99	1.20×10^{12}	3.52×10^{-4}
6707	3.15	0.72	0.45	5.62	5.54	5.92	17.7	1024.38	1.24×10^{12}	1.21×10^{-4}
7151	2.40	0.83	0.14	1.51	1.20	5.39	19.61	425.07	8.85×10^{10}	3.73×10^{-5}
7578	3.60	0.74	0.56	5.95	5.76	2.80	19.16	522.95	1.65×10^{11}	1.28×10^{-4}
8117	1.32	0.41	0.65	3.26	4.51	2.64	19.75	398.53	7.29×10^{10}	5.50×10^{-4}
8775	1.57	0.49	0.03	4.84	5.25	2.56	18.41	738.69	4.64×10^{11}	1.22×10^{-5}
10198	2.64	0.66	0.07	4.67	2.49	6.09	18.88	594.92	2.43×10^{11}	1.44×10^{-4}
10603	2.45	0.73	0.21	3.11	4.98	4.23	18.26	791.52	5.71×10^{11}	7.82×10^{-4}
11545	2.64	0.84	0.72	5.39	4.45	0.60	16.26	1988.20	9.05×10^{12}	2.27×10^{-4}
11805	1.75	0.60	0.04	3.34	5.11	0.42	17.59	1077.61	1.44×10^{12}	4.79×10^{-4}
12382	2.60	0.61	0.54	0.36	0.08	5.13	17.73	1010.32	1.19×10^{12}	4.84×10^{-4}
12965	2.47	0.63	0.19	0.21	5.55	0.06	17.83	964.85	1.03×10^{12}	8.89×10^{-4}
13175	1.05	0.18	1.27	4.90	1.65	3.65	19.1	537.60	1.79×10^{11}	3.23×10^{-5}
13323	1.08	0.16	0.59	3.28	4.39	1.41	19.42	463.94	1.15×10^{11}	2.00×10^{-5}
14414	2.46	0.60	0.42	2.94	0.19	5.30	19.16	522.95	1.65×10^{11}	1.68×10^{-4}
16594	1.58	0.40	0.02	4.61	2.76	2.09	19.77	394.88	7.09×10^{10}	5.05×10^{-5}
18875	1.76	0.52	0.20	1.16	4.11	4.24	19.76	396.70	7.19×10^{10}	3.16×10^{-4}
19021	1.00	0.21	0.23	0.43	4.86	3.12	19.22	508.70	1.52×10^{11}	5.16×10^{-4}
20406	2.75	0.80	0.59	2.35	4.74	1.30	16.46	1813.26	6.87×10^{12}	9.13×10^{-4}
22349	1.24	0.65	0.41	0.12	4.24	5.68	18.85	603.20	2.53×10^{11}	2.55×10^{-4}
25414	1.08	0.57	0.33	6.23	2.04	6.26	17.32	1220.28	2.09×10^{12}	6.42×10^{-5}
25716	1.60	0.37	0.36	1.39	0.04	5.17	18.67	655.33	3.24×10^{11}	1.52×10^{-4}

Table F.6: Orbital elements and physical properties of 30 asteroids. The diameter and mass were calculated using Equations 2.5 and 2.6, respectively, with the values of $p_v = 0.14$ and $\rho = 2200\ \mathrm{kg/m^3}$. The MOID was calculated for S/C 2.

F.3.2 Probability of Detection

Synodic Period Distribution

The distribution for the synodic period of the asteroids of the fictitious population is shown in Figure F.2. The highest synodic period belongs to Asteroid 9387, being $T^x_{\text{syn}} = 3279.22$ yr, and the lowest to Asteroid 22055, being $T^y_{\text{syn}} = 0.34$ yr.

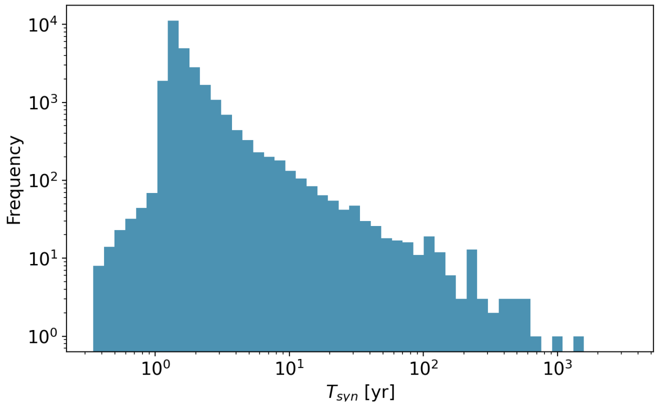

Figure F.2: Distribution of synodic periods for the fictitious population

δM Diagram and Area of Detectability

The mirroring effect of the angle δM between 0 and 2π makes that in the end there are two parallelograms for the area of detection. In theory depending on the slope, several parallelograms could happen due to mirroring effects. Nevertheless, the slope is linked to the orbital periods of the NEAs and that these vary in a way that only allow two parallelograms in the interval of $[0, 2\pi]$ rad. Figure F.3 illustrates this principle.

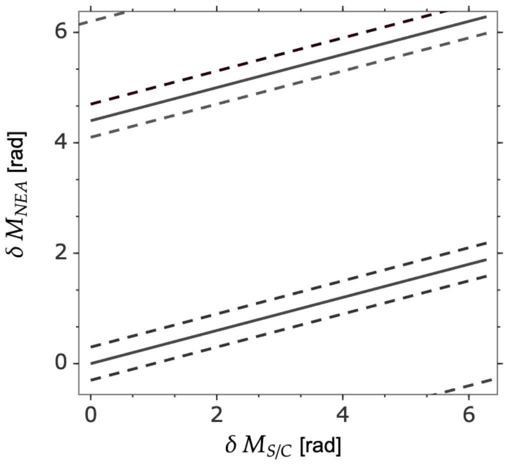

Figure F.3: Illustration of area of detectability in δM diagram. Not to scale. The bold line represents the linear relationship of Equation 3.11. The dashed lines are the limits of the detectable region, i.e the lines of SNR $= 5$.

Results

In Table F.7, the results of the probability of detection study for some asteroids of the fictitious population are shown.

			Non-Fixed Orbit		Fixed Orbit	
Name	SNR	T_{syn} [yr]	$P_{\text{det (1)}}$	$P_{\text{det (2)}}$	$P_{\text{det (1)}}$	$P_{\text{det (2)}}$
1279	492.24	1.62	$1.28^{+1.30}_{-0.65} \times 10^{-2}$	$1.03^{+1.04}_{-0.52} \times 10^{-2}$	$7.86^{+21.96}_{-5.77} \times 10^{-5}$	$6.32^{+17.41}_{-4.62} \times 10^{-5}$
1836	51520.68	1.71	$3.06^{+3.72}_{-1.67} \times 10^{-3}$	$2.47^{+2.97}_{-1.34} \times 10^{-3}$	$9.40^{+5.52}_{-3.48} \times 10^{-5}$	$7.58^{+4.42}_{-2.79} \times 10^{-5}$
2331	1836.15	2.34	$1.26^{+0.45}_{-0.33} \times 10^{-2}$	$1.06^{+0.38}_{-0.28} \times 10^{-2}$	$7.46^{+32.73}_{-6.06} \times 10^{-5}$	$5.96^{+25.75}_{-4.82} \times 10^{-5}$
2474	237.07	1.35	$1.61^{+1.63}_{-0.81} \times 10^{-3}$	$1.30^{+1.30}_{-0.65} \times 10^{-3}$	$6.99^{+145.12}_{-6.65} \times 10^{-5}$	$5.51^{+111.82}_{-5.23} \times 10^{-5}$
3112	7.85	1.59	$4.05^{+1.47}_{-1.07} \times 10^{-3}$	$3.28^{+1.18}_{-0.86} \times 10^{-3}$	$7.41^{+160.66}_{-7.06} \times 10^{-5}$	$5.76^{+122.04}_{-5.48} \times 10^{-5}$
4368	144.79	1.42	$2.67^{+2.83}_{-1.37} \times 10^{-3}$	$2.16^{+2.25}_{-1.10} \times 10^{-3}$	$3.71^{+16.79}_{-3.02} \times 10^{-5}$	$2.91^{+13.01}_{-2.37} \times 10^{-5}$
4644	28240.29	1.42	$3.44^{+1.78}_{-1.17} \times 10^{-3}$	$2.78^{+1.42}_{-0.94} \times 10^{-3}$	$7.33^{+6.16}_{-3.34} \times 10^{-5}$	$5.88^{+4.88}_{-2.66} \times 10^{-5}$
5401	751.53	1.19	$7.39^{+5.86}_{-3.26} \times 10^{-3}$	$6.00^{+4.71}_{-2.63} \times 10^{-3}$	$1.02^{+0.50}_{-0.33} \times 10^{-4}$	$8.34^{+4.02}_{-2.70} \times 10^{-5}$
6135	235.80	3.27	$1.51^{+1.13}_{-0.64} \times 10^{-3}$	$1.21^{+0.90}_{-0.52} \times 10^{-3}$	$7.31^{+33.74}_{-5.98} \times 10^{-5}$	$5.78^{+26.30}_{-4.72} \times 10^{-5}$
6707	1654.02	1.22	$5.85^{+6.30}_{-3.03} \times 10^{-3}$	$4.76^{+5.07}_{-2.45} \times 10^{-3}$	$1.32^{+6.03}_{-1.08} \times 10^{-4}$	$1.06^{+4.76}_{-0.86} \times 10^{-4}$
7151	1906.86	1.37	$4.17^{+2.02}_{-1.36} \times 10^{-3}$	$3.37^{+1.62}_{-1.09} \times 10^{-3}$	$9.75^{+2.52}_{-2.00} \times 10^{-5}$	$7.95^{+2.04}_{-1.62} \times 10^{-5}$
7578	275.42	1.17	$6.57^{+12.9}_{-4.34} \times 10^{-3}$	$5.26^{+10.2}_{-3.46} \times 10^{-3}$	$1.18^{+31.87}_{-1.13} \times 10^{-4}$	$9.14^{+242.01}_{-8.79} \times 10^{-5}$
8117	6.32	2.95	$6.78^{+185.33}_{-6.52} \times 10^{-4}$	$5.53^{+146.8}_{-5.32} \times 10^{-4}$	$3.41^{+195.86}_{-3.34} \times 10^{-5}$	$2.61^{+146.11}_{-2.56} \times 10^{-5}$
8775	62177.07	2.03	$1.27^{+0.08}_{-0.07} \times 10^{-2}$	$1.03^{+0.06}_{-0.06} \times 10^{-2}$	$1.07^{+1.00}_{-0.52} \times 10^{-4}$	$8.68^{+8.00}_{-4.15} \times 10^{-5}$
10603	20.71	1.35	$2.83^{+3.26}_{-1.51} \times 10^{-3}$	$2.27^{+2.58}_{-1.20} \times 10^{-3}$	$5.54^{+17.70}_{-4.21} \times 10^{-5}$	$4.46^{+14.04}_{-3.37} \times 10^{-5}$
11545	3470.39	1.30	$1.45^{+0.40}_{-0.32} \times 10^{-3}$	$1.18^{+0.32}_{-0.25} \times 10^{-3}$	$9.40^{+3.26}_{-2.45} \times 10^{-5}$	$7.98^{+2.62}_{-1.97} \times 10^{-5}$
11805	179.07	1.76	$1.14^{+0.18}_{-0.16} \times 10^{-2}$	$9.32^{+1.49}_{-1.29} \times 10^{-3}$	$8.15^{+7.93}_{-4.01} \times 10^{-5}$	$6.65^{+6.39}_{-3.25} \times 10^{-5}$
13323	8801.66	8.77	$5.33^{+4.35}_{-2.39} \times 10^{-4}$	$4.29^{+3.46}_{-1.91} \times 10^{-4}$	$4.18^{+3.59}_{-1.93} \times 10^{-5}$	$3.36^{+2.86}_{-1.54} \times 10^{-5}$
14414	120.68	1.35	$7.73^{+6.42}_{-3.50} \times 10^{-3}$	$6.22^{+5.11}_{-2.80} \times 10^{-3}$	$6.11^{+30.54}_{-5.07} \times 10^{-5}$	$4.81^{+23.65}_{-3.98} \times 10^{-5}$
19021	11.94	185.09	$2.34^{+1.02}_{-0.71} \times 10^{-5}$	$1.91^{+0.82}_{-0.57} \times 10^{-5}$	$6.94^{+53.75}_{-6.12} \times 10^{-7}$	$5.35^{+40.81}_{-4.71} \times 10^{-7}$

Table F.7: Probability of detection for the non-fixed and fixed orbits scenarios for 20 asteroids of the fictitious population. (1) uses an uniform distribution (Figure 3.9) for the probability density distribution of ρ and (2) uses a gamma function (Figure 3.10). The synodic periods T_{syn} were calculated with S/C 2.

F.3.3 Uncertainty in Parameters

Standard Deviations

In Table F.8, the collected uncertainties calculated through the Fisher Information method (see 3.4 Assessing the Uncertainty in Measurements) for some of the fictitious NEAs generated are shown. In Figure F.4, the respective correlation matrices are displayed.

Name	SNR	σ_a [au]	σ_e	σ_i [rad]	σ_Ω [rad]	σ_ω [rad]	σ_m^* [%]
1279	492.24	2.04×10^{-6}	1.31×10^{-6}	2.04×10^{-7}	1.17×10^{-6}	6.50×10^{-6}	3.17×10^{-4}
1836	51520.68	9.17×10^{-11}	5.26×10^{-11}	5.94×10^{-10}	1.98×10^{-10}	9.08×10^{-11}	1.31×10^{-6}
2331	1836.15	1.41×10^{-7}	6.71×10^{-8}	2.14×10^{-7}	2.79×10^{-8}	3.38×10^{-8}	2.34×10^{-4}
2474	237.07	2.05×10^{-6}	1.03×10^{-6}	4.68×10^{-6}	3.47×10^{-8}	4.34×10^{-6}	8.75×10^{-4}
3629	7.85	3.31×10^{-5}	1.03×10^{-4}	3.67×10^{-4}	2.62×10^{-6}	2.18×10^{-4}	0.11
4368	144.79	8.16×10^{-5}	2.45×10^{-5}	5.99×10^{-5}	8.54×10^{-6}	8.00×10^{-5}	0.037
4644	28240.29	2.62×10^{-13}	1.17×10^{-13}	1.29×10^{-12}	3.42×10^{-13}	7.00×10^{-14}	1.09×10^{-7}
5401	751.53	1.23×10^{-7}	1.15×10^{-8}	3.29×10^{-7}	1.50×10^{-8}	2.12×10^{-8}	2.07×10^{-4}
6135	235.80	6.84×10^{-7}	1.07×10^{-6}	1.02×10^{-5}	2.25×10^{-6}	2.59×10^{-6}	1.91×10^{-3}
6707	1654.02	1.40×10^{-9}	1.89×10^{-10}	2.28×10^{-8}	2.66×10^{-10}	6.50×10^{-10}	3.84×10^{-5}
7151	1906.86	5.36×10^{-11}	2.82×10^{-11}	1.51×10^{-9}	4.61×10^{-10}	5.36×10^{-10}	6.57×10^{-6}
7578	275.42	2.30×10^{-8}	2.00×10^{-9}	7.90×10^{-7}	1.27×10^{-8}	6.51×10^{-9}	6.28×10^{-5}
8117	6.32	7.12×10^{-5}	1.93×10^{-4}	4.80×10^{-4}	9.45×10^{-6}	4.68×10^{-4}	0.16
8775	62177.07	1.60×10^{-14}	1.90×10^{-14}	3.78×10^{-14}	2.58×10^{-13}	2.27×10^{-13}	1.40×10^{-7}
10198	251.50	2.99×10^{-7}	5.72×10^{-8}	7.41×10^{-8}	7.45×10^{-8}	2.33×10^{-7}	1.42×10^{-4}
10603	20.71	1.93×10^{-4}	1.39×10^{-4}	4.01×10^{-4}	7.29×10^{-5}	5.48×10^{-4}	0.10
11545	3470.39	5.30×10^{-9}	2.93×10^{-9}	1.33×10^{-7}	1.46×10^{-11}	1.70×10^{-8}	1.14×10^{-5}
11805	179.07	1.28×10^{-5}	1.97×10^{-5}	1.40×10^{-5}	6.55×10^{-5}	1.19×10^{-4}	0.019
12382	123.88	5.26×10^{-5}	7.87×10^{-6}	3.98×10^{-5}	1.22×10^{-6}	4.22×10^{-6}	0.019
12965	23.74	2.77×10^{-4}	5.99×10^{-5}	5.78×10^{-5}	1.19×10^{-5}	1.54×10^{-4}	0.096
13175	4507.01	5.12×10^{-13}	5.89×10^{-12}	2.25×10^{-10}	9.77×10^{-13}	1.20×10^{-11}	3.89×10^{-7}
13323	8801.66	1.18×10^{-12}	3.18×10^{-12}	2.87×10^{-10}	6.96×10^{-12}	7.55×10^{-13}	4.18×10^{-7}
14414	120.68	1.22×10^{-6}	2.03×10^{-7}	2.65×10^{-6}	8.70×10^{-8}	1.25×10^{-7}	1.44×10^{-3}
16594	727.91	3.74×10^{-9}	1.82×10^{-9}	1.11×10^{-10}	1.61×10^{-9}	4.47×10^{-9}	2.18×10^{-5}
18875	21.99	9.14×10^{-5}	5.49×10^{-5}	4.07×10^{-5}	8.41×10^{-6}	1.48×10^{-4}	0.031
19021	11.94	1.39×10^{-5}	7.81×10^{-5}	2.79×10^{-4}	4.28×10^{-5}	1.85×10^{-4}	0.17
20406	90.67	5.70×10^{-7}	2.33×10^{-6}	3.10×10^{-5}	1.84×10^{-7}	1.31×10^{-5}	3.20×10^{-3}
22349	149.50	1.05×10^{-6}	1.55×10^{-6}	3.36×10^{-6}	1.49×10^{-7}	4.00×10^{-6}	4.36×10^{-4}
25414	19208.36	2.18×10^{-10}	3.98×10^{-10}	2.70×10^{-10}	1.70×10^{-11}	8.88×10^{-10}	3.07×10^{-7}
25716	438.90	2.18×10^{-7}	8.56×10^{-8}	2.90×10^{-6}	1.51×10^{-7}	1.43×10^{-7}	1.67×10^{-3}

Table F.8: Uncertainties in orbital elements for 30 asteroids of the fictitious population. The close approaches were calculated between the asteroids and S/C 2. These standards of deviation were calculated using $\boldsymbol{\Delta\theta} = \begin{bmatrix}10^{-6}\,a & 10^{-6}\,e & 10^{-4}\,i & 10^{-6}\,\Omega & 10^{-6}\,\omega & 10^{-2}\,m\end{bmatrix}$.

Correlation Matrices

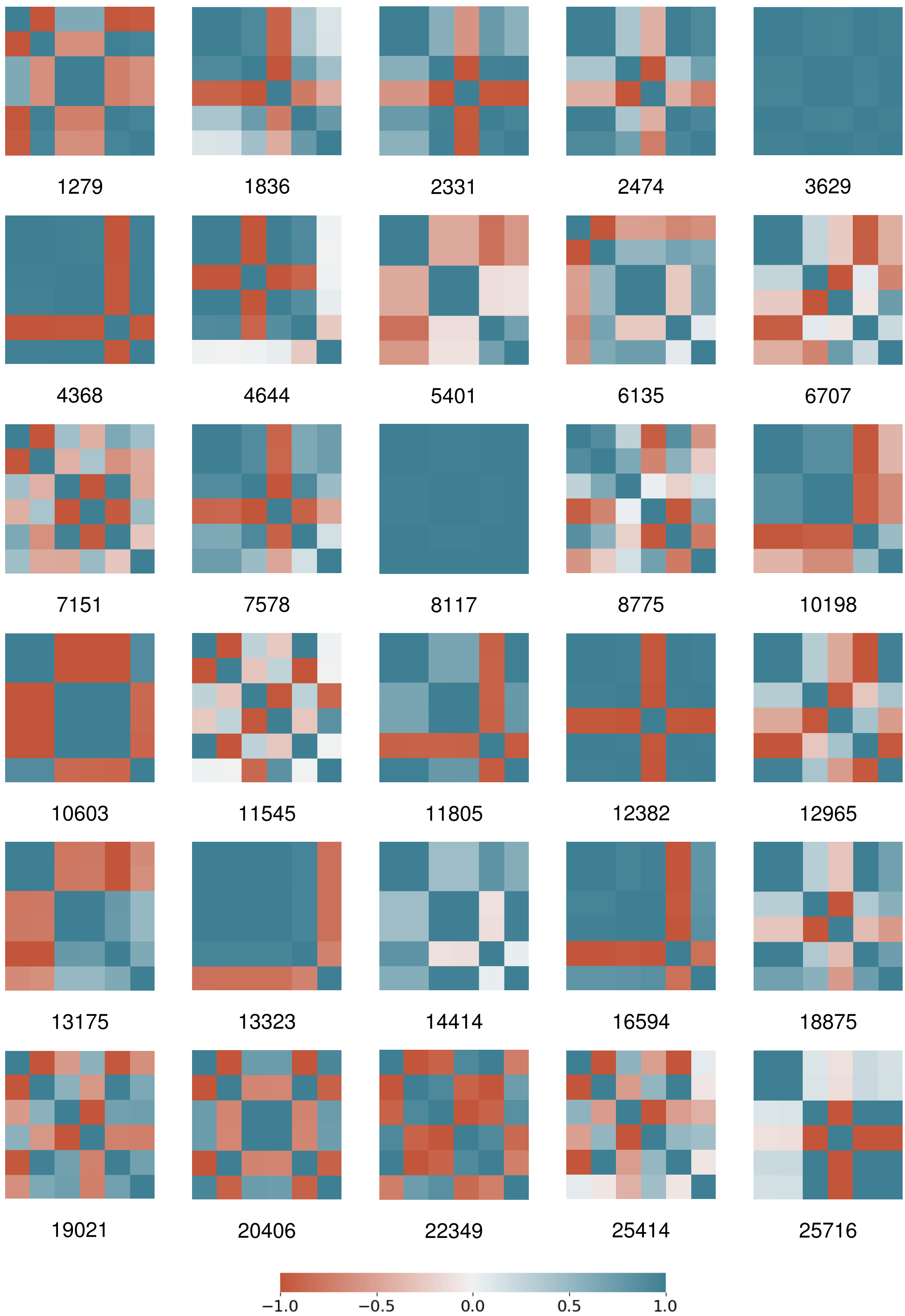

Figure F.4: Correlation matrices from Fisher information study for 30 asteroids of the fictitious population. These correlation matrices were calculated using $\boldsymbol{\Delta\theta} = [10^{-6}\,a \quad 10^{-6}\,e \quad 10^{-4}\,i \quad 10^{-6}\,\Omega \quad 10^{-6}\,\omega \quad 10^{-2}\,m]$.